

DESIGN, SYNTHESIS, AND IMPEDANCE SPECTROSCOPY  
OF TRIPLE IONIC-ELECTRONIC CONDUCTING  
THIN FILM ELECTRODES

by

Meagan Christine Papac

© Copyright by Meagan Christine Papac, 2021

All Rights Reserved

A thesis submitted to the Faculty and the Board of Trustees of the Colorado School of Mines in partial fulfillment of the requirements for the degree of Doctor of Philosophy (Materials Science).

Golden, Colorado

Date \_\_\_\_\_

Signed: \_\_\_\_\_

Meagan Christine Papac

Signed: \_\_\_\_\_

Dr. Ryan O'Hayre  
Thesis Advisor

Signed: \_\_\_\_\_

Dr. Andriy Zakutayev  
Thesis Advisor

Golden, Colorado

Date \_\_\_\_\_

Signed: \_\_\_\_\_

Dr. Angus Rockett  
Professor and Department Head  
Department of Metallurgical and Materials Engineering

## ABSTRACT

Triple ionic-electronic conducting oxides (TIECs) conduct electrons alongside at least two ionic species and are of interest for use in intermediate temperature (300°C–600°C) electrochemical devices. Transport properties of these materials are dependent on defect concentrations, which can be moderated by cation substitution and by operating conditions. Thus, effective improvement and development of these materials for targeted device applications necessitates comprehensive understanding of how these variables affect materials properties. In pursuit of this understanding, new tools were developed and applied to a promising TIEC material system.

To begin, a review of TIEC materials is presented to summarize current understanding of defect formation and conduction mechanisms in single-phase TIECs. To build on this understanding, combinatorial materials synthesis and characterization methods were utilized and advanced. An instrument was developed for spatially resolved measurements of thin-film impedance at temperatures up to 300°C under dry or humidified gas (air or nitrogen). The probe arm was uniquely designed to direct localized gas flow toward the sample point being measured, enabling benchtop operation and allowing time-dependent measurement of impedance as the sample equilibrates to the gas flow. The stage and probe assembly were also employed for collection of current-voltage curves to determine DC conductivity. Custom data processing procedures, including loading and visualization routines, were developed within a combinatorial data analysis software package. Lastly, the instrument was applied to a study of electronic properties of combinatorial thin film libraries of  $\text{Ba}(\text{Co,Fe,Zr,Y})\text{O}_3$  (BCFZY), a materials system that is being explored for electrocatalytic applications in ceramic fuel cells and electrolyzers. The libraries were deposited by pulsed laser deposition. Device performance, as represented by polarization resistance of half fuel cells comprising BCFZY thin films atop an electrolyte layer, was evaluated as a function of temperature and gas atmosphere. The dependence of polarization resistance on chemical composition, temperature, and hydration is reported.

## TABLE OF CONTENTS

ABSTRACT . . . . .	iii
LIST OF FIGURES . . . . .	viii
LIST OF TABLES . . . . .	x
LIST OF SYMBOLS . . . . .	xi
LIST OF ABBREVIATIONS . . . . .	xi
ACKNOWLEDGMENTS . . . . .	xii
DEDICATION . . . . .	xiii
CHAPTER 1 INTRODUCTION . . . . .	1
CHAPTER 2 TRIPLE IONIC-ELECTRONIC CONDUCTING OXIDES FOR NEXT-GENERATION ELECTROCHEMICAL DEVICES . . . . .	3
2.1 Abstract . . . . .	3
2.2 Introduction . . . . .	3
2.3 TIEC applications . . . . .	5
2.4 Electronic properties of TIECs . . . . .	9
2.4.1 Charge generation and transport . . . . .	9
2.4.2 Surface reactions . . . . .	11
2.5 TIEC discovery . . . . .	12
2.5.1 Crystal structure . . . . .	12
2.5.2 Ion electronegativity . . . . .	13
2.5.3 Other considerations . . . . .	14
2.6 Chemical design of TIECs . . . . .	14
2.6.1 B-site substitution . . . . .	15
2.6.2 A-site substitution . . . . .	15
2.6.3 Anion substitution . . . . .	16
2.7 Research directions . . . . .	17

2.7.1	Deconvolute charge-carrier contributions . . . . .	18
2.7.2	Improve chemical stability . . . . .	22
2.7.3	Enable ORR/OER below 400°C . . . . .	22
2.7.4	Discover and design n-Type TIECs . . . . .	22
2.8	Summary and outlook . . . . .	24
CHAPTER 3 INSTRUMENT FOR SPATIALLY RESOLVED, TEMPERATURE-DEPENDENT ELECTROCHEMICAL IMPEDANCE SPECTROSCOPY OF THIN FILMS UNDER LOCALLY CONTROLLED ATMOSPHERE . . . . .		
3.1	Abstract . . . . .	25
3.2	Introduction . . . . .	25
3.3	Design of the instrument . . . . .	27
3.3.1	Design overview . . . . .	27
3.3.2	Electrical probing of the sample . . . . .	29
3.3.3	Temperature and gas flow control . . . . .	30
3.3.4	Data collection . . . . .	31
3.3.5	Data analysis . . . . .	32
3.4	Experimental methods . . . . .	33
3.4.1	Preparation of thin-film sample libraries . . . . .	33
3.4.2	Characterization of thin-film structure and composition . . . . .	34
3.4.3	Electrical measurements and equivalent circuit model fitting . . . . .	35
3.5	Demonstrating instrument capability . . . . .	36
3.5.1	Measurement repeatability and accuracy . . . . .	36
3.5.2	Gas-dependent results . . . . .	39
3.5.3	Mapping property variation on a compositionally graded library . . . . .	40
3.5.4	Experimental throughput . . . . .	40
3.6	Summary . . . . .	41
CHAPTER 4 COMBINATORIAL SCREENING OF TRIPLE IONIC-ELECTRONIC CONDUCTING, TRANSITION-METAL SUBSTITUTED BARIUM ZIRCONATE ELECTRODES . . . . .		
		43

4.1	Abstract . . . . .	43
4.2	Introduction . . . . .	43
4.3	Methods . . . . .	45
4.4	Thin film synthesis . . . . .	45
4.5	Thin film characterization . . . . .	47
4.5.1	Structure and composition . . . . .	47
4.6	Electrical characterization . . . . .	47
4.7	Results and discussion . . . . .	48
4.7.1	PLD deposition parameters . . . . .	48
4.7.2	Structure and composition . . . . .	49
4.7.3	DC results . . . . .	49
4.7.4	Polarization resistance . . . . .	50
4.8	Conclusions . . . . .	51
	CHAPTER 5 EPILOGUE . . . . .	52
5.1	Summary . . . . .	52
5.2	Conclusions . . . . .	52
5.3	Future research directions . . . . .	53
5.4	Additional research contributions . . . . .	53
	REFERENCES . . . . .	54
	APPENDIX A SUPPLEMENTAL INFORMATION FOR INSTRUMENT FOR SPATIALLY RESOLVED, TEMPERATURE-DEPENDENT ELECTROCHEMICAL IMPEDANCE SPECTROSCOPY OF THIN FILMS UNDER LOCALLY CONTROLLED ATMOSPHERE . . . . .	70
A.1	Synthesis by pulsed laser deposition . . . . .	70
A.2	Statistical analysis . . . . .	70
A.3	Temperature calibration . . . . .	72
A.4	Humidity calibration . . . . .	72
A.5	Alignment effects . . . . .	73
A.6	ITO resistance . . . . .	73

APPENDIX B SUPPLEMENTAL INFORMATION FOR COMBINATORIAL SCREENING OF TRIPLE IONIC-ELECTRONIC CONDUCTING, TRANSITION-METAL SUBSTITUTED BARIUM ZIRCONATE ELECTRODES . . . . .	75
B.1 Target synthesis . . . . .	75
B.2 X-ray diffraction spectra of thin films . . . . .	75
B.3 Substrate comparison . . . . .	75
B.4 Equivalent circuit model results . . . . .	76
B.5 Electrolyte impedance . . . . .	76
B.6 Validity of polarization resistance fit method . . . . .	76
APPENDIX C COPYRIGHT PERMISSIONS . . . . .	79

## LIST OF FIGURES

Figure 2.1	Typical structure of TIEC materials. . . . .	4
Figure 2.2	TIECs as protonic ceramic fuel cell positrodes. . . . .	6
Figure 2.3	Effect of $p_{O_2}$ on charge carrier concentration. . . . .	8
Figure 2.4	Transport in TIECs. . . . .	10
Figure 2.5	Factors that influence TIEC performance. . . . .	19
Figure 2.6	Composition effects on electronic conductivity, oxygen non-stoichiometry, and proton uptake. . . . .	20
Figure 2.7	Conceptual band diagram of an n-type TIEC. . . . .	23
Figure 3.1	Instrument and sample layout. . . . .	28
Figure 3.2	Calibration curves for temperature and humidity. . . . .	30
Figure 3.3	Work flow for the user and for the LabVIEW-controlled, automated process. . . . .	32
Figure 3.4	Representative composition and structure data. . . . .	34
Figure 3.5	Impedance spectra and equivalent circuit model. . . . .	36
Figure 3.6	Spatial maps of $R_{\text{elyte}}$ among various sets of measurements of the BZY20 thin film. . . . .	37
Figure 3.7	Conductivity comparison between the BZY20 film measured in this study to materials with similar chemical compositions from the literature. . . . .	38
Figure 3.8	Resistance of BZY20 samples measured under dry and humid gases. . . . .	39
Figure 3.9	Temperature-dependent polarization resistance ( $R_p$ ) results from a compositionally graded BCFZY thin film. . . . .	40
Figure 3.10	Polarization resistance across the compositional spread of a $\text{Ba}(\text{Zr},\text{Y},\text{Co},\text{Fe})\text{O}_3$ thin film. . . . .	41
Figure 4.1	Pulsed laser deposition for synthesis of combinatorial libraries. . . . .	45
Figure 4.2	Effect of deposition variables on thin film XRD patterns . . . . .	48
Figure 4.3	Results of structural and microstructural analysis. . . . .	49
Figure 4.4	Results of DC and AC electronic measurements under dry and humid conditions. . . . .	50
Figure A.1	Schematic of the interior of the combinatorial pulsed deposition chamber . . . . .	70
Figure A.2	KS test results. . . . .	71

Figure A.3	Surface temperature over time at heater setpoints between 100°C and 500°C. . . . .	72
Figure A.4	Difference over time between the measured temperature at the sample surface and the mean measured temperature. . . . .	73
Figure A.5	Relative humidity over time for three different flow rates of humidified N <sub>2</sub> . . . . .	73
Figure A.6	Nyquist plot from a single contact measured with variation in x and z coordinates. . . . .	74
Figure A.7	DC resistance of ITO compared to resistances of samples measured by impedance spectroscopy. . . . .	74
Figure B.1	XRD patterns of all libraries presented in this study. . . . .	75
Figure B.2	Diffraction patterns of BCFZY films on SiO <sub>2</sub> and on ITO compared to the diffraction pattern of an ITO substrate. . . . .	76
Figure B.3	Equivalent circuit model fits of impedance spectra. . . . .	77
Figure B.4	Electrolyte resistance, as determined by the equivalent circuit model fit. . . . .	78
Figure B.5	Comparison of polarization resistance values obtained through different methods. . . . .	78

## LIST OF TABLES

Table 2.1	Common characterization techniques for mixed-conducting oxides . . . . .	21
Table 4.1	Unique sample types for each characterization method. . . . .	46
Table A.1	KS test results from samples in different orientations and under different environmental conditions. . . . .	71

## LIST OF SYMBOLS

Diffraction angle . . . . .	$2\theta$
Frequency . . . . .	$\omega$
Polarization resistance . . . . .	$R_p$

## LIST OF ABBREVIATIONS

Constant phase element . . . . .	CPE
Distribution of relaxation times . . . . .	DRT
Equivalent circuit model . . . . .	ECM
Full width at half maximum . . . . .	FWHM
Mixed ionic-electronic conducting oxide . . . . .	MIEC
Oxygen evolution reaction . . . . .	OER
Oxygen reduction reaction . . . . .	ORR
Protonic ceramic fuel cell . . . . .	PCFC
Scanning electron microscopy . . . . .	SEM
Solid oxide fuel cell . . . . .	SOFC
Triple ionic-electronic conducting oxide . . . . .	TIEC
Triple phase boundary . . . . .	TPB
X-ray diffraction . . . . .	XRD
X-ray fluorescence . . . . .	XRF

## ACKNOWLEDGMENTS

Large tasks are never accomplished alone and my mentors, colleagues, friends, and family have made an overwhelming number of both large and small contributions that have carried me through my graduate school experience. I would like to thank my advisor, Dr. Ryan O'Hayre, for bringing me on to this project and keeping an eye out for opportunities for me. I would like to thank my co-advisor, Dr. Andriy Zakutayev, for entertaining my curiosity and for providing encouragement when I needed it most.

Special thanks to Dr. Kevin Talley for his flexible assistance with many odds and ends, to Jake Huang for copious conversations about impedance spectroscopy, and to my many other colleagues at NREL and Mines who have provided inspiration and assistance over the last several years. Many thanks to my friends and family for their support and encouragement. And to my heavy bag...thank you for being so solid and for not breaking my knuckles. Last, but not least, I want to express my appreciation to my daughter, Kelbri. Her enthusiasm, understanding, and cheerleading are unmatched, and I cannot imagine how I would have accomplished this without her.

For Kelbri Kohl

## CHAPTER 1

### INTRODUCTION

Materials research is making use of increasingly complex materials in order to meet the stringent demands of modern technological advancements. Materials that possess a perovskite, or  $ABO_3$ , structure are of particular interest due to flexibility in A-site, B-site, and even anion substitution. These materials can display complex behavior that is moderated by their chemical composition. Perovskite-structured materials have been studied for a variety of applications, from dielectrics to superconductors, including piezoelectrics, magnets, and catalysts. In particular, their ionic and electronic transport properties are well suited to application as electrolytes and electrodes in solid oxide fuel cells (SOFCs).

An effort to reduce operating temperature of SOFCs has led to the development of protonic ceramic fuel cells (PCFCs), a sub-category of SOFCs that utilizes proton-conducting electrolytes, rather than more traditional oxygen-conducting electrolytes. Operating temperature can be reduced because of lower migration energy for protons compared to oxide ions. Not only do these electrolytes facilitate lower operating temperatures, but they eliminate dilution of the fuel stream by waste, since water is produced on the air electrode side, rather than on the fuel electrode side.

In PCFCs, several reaction and transport steps occur at the cathode (air electrode), including reduction of gaseous oxygen at the surface, transport of protons from the electrolyte, and formation of water (a reaction involving protons, oxygen, and electrons).[1] Consequently, the cathode must possess diverse transport and catalytic properties, including high proton conductivity, high surface exchange for the oxygen reduction reaction, and considerable electronic conduction. Traditional cathodes for solid oxide fuel cells are mixed oxide ion and electronic conductors. With the transition to proton-conducting electrolytes, proton conduction in the cathode is also desirable. In this case, oxide ion transport is less critical, but high oxygen reduction reaction activity is required. These two properties are typically governed by the same materials characteristics.

Several previous approaches to PCFC cathode design have improved performance by infiltrating oxides with catalysts or carefully architecting composite structures by combining proton conductors and mixed ionic and electronic conductors.[2–5] While these approaches have achieved some success, they limit the location of the cathode reaction to the triple phase boundary (the point or interface at which the three reaction species can come together) limiting power density. Another approach that has achieved very high performance in PCFCs involves single phase, triple ionic-electronic conducting oxides (TIECs), which transport all three species simultaneously, eliminating reliance on triple phase boundaries.[6–8]

$\text{BaZr}_{0.1}\text{Y}_{0.1}\text{Co}_{0.4}\text{Fe}_{0.4}\text{O}_{3-\delta}$  (BCFZY1144) is one perovskite that has demonstrated triple conduction. Consequently, the BCFZY materials system was chosen here for a detailed study of transport properties as determined by B-site substitution. While transport in this and other complex oxides has been investigated, conclusions from a particular study are typically isolated to a very limited compositional space. As the number of species included in these materials increases, the number of possible combinations greatly increases as well. Thus, to keep up with the breadth of possible elemental combinations, scientists are developing sophisticated tools for rapidly screening compositions utilizing high-throughput experimental methods. High-throughput synthesis typically employs combinatorial physical vapor deposition, which produces thin films with spatially varying chemical composition. High-throughput characterization methods allow rapid screening of structure and properties. In this way, large composition spreads can be synthesized and characterized in a matter of weeks or months, significantly reducing the time scale of materials exploration compared to serial methods. Additionally, machine learning techniques can be applied to both computational and experimental data to process very large data sets, analyze relevant variables, and predict properties of compositions that have not yet been investigated.

In an effort to advance the development of TIEC materials, the work presented here pursues the following goals:

1. Aggregate and consolidate current understanding of mixed conduction in oxides to form a complete picture of current understanding of these materials, especially as applied to TIECs.
2. Develop a combinatorial approach to cathode characterization to expedite the route to materials optimization.
3. Explore the BCFZY materials family to test these methods and identify promising compositions for high PCFC cathode performance.

The following chapters describe the progress made toward each of these goals. Chapter 2 is a review on the current body of research on transport in mixed conducting oxides. Chapter 3 describes development of a spatially resolved method for characterizing performance of combinatorial thin film electrodes. Chapter 4 details the results of this characterization on BCFZY thin films. Chapter 5 summarizes the work.

CHAPTER 2  
TRIPLE IONIC-ELECTRONIC CONDUCTING OXIDES FOR NEXT-GENERATION  
ELECTROCHEMICAL DEVICES

Reprinted with permission from Nature Materials.<sup>1</sup>

Meagan Papac,<sup>2,3</sup> Vladan Stevanović,<sup>7,8</sup> Andriy Zakutayev,<sup>7,8</sup> and Ryan O’Hayre<sup>7</sup>.

## 2.1 Abstract

Triple ionic-electronic conductors (TIECs) are materials that can simultaneously transport electronic species alongside two ionic species. The recent emergence of TIECs provides intriguing opportunities to maximize performance in a variety of electrochemical devices, including fuel cells, membrane reactors, and electrolysis cells. However, the potential application of these nascent materials is limited by lack of fundamental knowledge of their transport properties and electrocatalytic activity. The goal of this review is to summarize and analyze the current understanding of TIEC transport and electrochemistry in single-phase materials, including defect formation and conduction mechanisms. We particularly focus on the discovery criteria (e.g., crystal structure and ion electronegativity), design principles (e.g., cation and anion substitution chemistry), and operating conditions (e.g., atmosphere) of materials that enable deliberate tuning of the conductivity of each charge carrier. Lastly, we identify important areas for further advances, including higher chemical stability, lower operating temperatures, and discovery of n-type TIEC materials.

## 2.2 Introduction

Mixed ionic-electronic conductors (MIECs) simultaneously accommodate both ionic and electronic conduction and are used in a variety of applications, including fuel cells, electrolyzers, and electrochemical membrane reactors.[9–11] Most MIECs are perovskite (or perovskite-like) materials based on the  $ABO_3$  formula unit (Figure 2.1), with Ba, La, Sr, or Gd on the A-site and one or more transition metals on the B-site. Although MIECs of other structures have been investigated, the facile rotation of corner-sharing oxygen octahedra exhibited by the perovskite structure enables superior ionic transport.[11]

This review discusses the science and potential applications of triple ionic-electronic conductors (TIECs), an emerging class of materials that are related to MIECs, but can simultaneously transport more than one ionic species. Note that we specifically focus on this phenomenon in single-phase materials, while

---

<sup>1</sup>Reprinted from Nat. Mat., 20(3), 301-313.

<sup>2</sup>Department of Metallurgical and Materials Engineering, Colorado School of Mines

<sup>3</sup>Materials, Chemical, and Computational Science directorate, National Renewable Energy Laboratory

other strategies to achieve multi-species conduction may employ multi-phase materials or composites.[12] This unique feature can dramatically increase performance and diversify functionality of electrochemical energy conversion and gas separation devices and precludes reliance on triple phase boundaries, which are required for operation of these devices if they comprise single-carrier conductors.[6, 13, 14] These applications require that TIECs sustain sufficient electronic conductivity as electrodes or electrocatalysts under high current while enabling significant electrochemical functionality by multi-species ionic conduction. Ionic conductivity typically includes only protons ( $H^+$ ) and oxygen ions ( $O^{2-}$ ).[15, 16] We point out, however, that the development of TIECs that transport alternative or additional ionic species, such as  $Li^+$ ,  $Na^+$ , or  $OH^-$ , is a tantalizing prospect for future research.

Due to the typically higher mobility of electrons versus ions, TIECs are dominantly electronic conductors and can be classified as either n-type or p-type, depending on whether the majority carriers are electrons or holes. Although we use semiconductor nomenclature in this review for simplicity (i.e., n-type/p-type, electrons/holes), it is important to note that most TIECs are based on transition-metal-substituted wide-bandgap oxides; electronic conduction generally occurs via a small-polaron hopping mechanism and shows temperature-activated behavior. Furthermore, all TIECs encountered in the current literature are p-type, acceptor-doped oxides. In n-type conductors, oxygen vacancies are filled at the expense of electronic charge carriers. Thus, the development of an n-type TIEC that could operate under oxidizing conditions would represent a significant scientific breakthrough. Strategies for accomplishing this will be discussed later in this review.

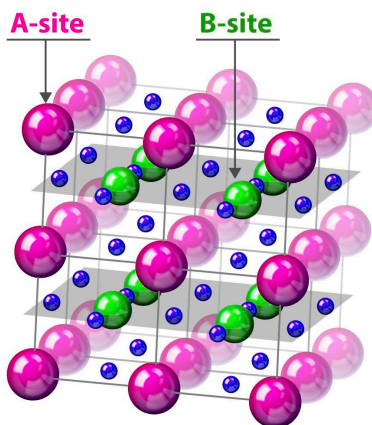


Figure 2.1 Typical structure of TIEC materials. Idealized perovskite structure, demonstrating the A-site (pink) and the B-site (green), which is surrounded by an oxygen (blue) octahedron. The 200, or B-O, planes are indicated in grey. The relevance of these planes to charge transport is further illustrated in Figure 2.4

### 2.3 TIEC applications

TIECs may be applied to any device in which multi-species conduction is beneficial. However, they have primarily been developed as air electrodes for electrochemical cells (Figure 2.2a) and designed to operate in oxidizing conditions. Under fuel cell operation, the TIEC catalyzes the oxygen reduction reaction (ORR) and serves as the cathode. Under electrolysis operation, the same electrode catalyzes the oxygen evolution reaction (OER) and serves as the anode. To avoid confusion, we refer to this electrode as a 'positrode' because it is the positive electrode in both device modes.[17] Similarly, 'negatrode' describes the negative electrode.

Three primary categories of solid oxide electrochemical cells are defined by the ionic species transported through the electrolyte. The electrolyte may be primarily an oxygen-ion conductor (such as in a solid oxide fuel cell (SOFC)), a proton conductor (such as in a protonic ceramic fuel cell (PCFC)), or a mixed oxygen-ion and proton conductor. The electrode materials must facilitate required reactions and transport. For example, holes, protons, and oxygen must be brought together for the electrochemical reaction at a PCFC positrode, making a TIEC positrode a logical choice.[18] This reaction does not directly necessitate oxygen-ion transport, but it does require high ORR activity, which often accompanies oxygen-ion transport.[19] Furthermore, the additional bulk and surface transport pathways enabled by oxygen-ion conduction may increase the positrode reaction rate. Experiments have shown that when applied as PCFC positrodes, TIECs enable high performance and operation at temperatures as low as 350°C, which is unprecedented for ceramic fuel cells.[6, 13, 16] The advantage of the transport pathways provided by an  $H^+/O^{2-}/h^+$  TIEC is illustrated in Figure 2.2b.

TIECs may also benefit the performance of other types of solid oxide electrochemical cells. For example, triple-conducting  $BaCo_{0.4}Fe_{0.4}Zr_{0.1}Y_{0.1}O_{3-\delta}$  (BCFZY10) increased the intermediate-temperature performance of an SOFC compared to  $Ba_{0.5}Sr_{0.5}Co_{0.8}Fe_{0.2}O_{3-\delta}$ , one of the highest-performing mixed-conducting SOFC positrodes.[20] Although the proton conductivity offered by a TIEC may be extraneous in this application, it nevertheless yields high performance through mobile oxygen-vacancy defects and high ORR activity. Additionally, the potential application of BCFZY10 as a mixed-ion-conducting electrolyte was demonstrated by creating a p-n junction with ZnO, which suppressed the electronic conductivity and enhanced proton and oxygen-vacancy transport.[21] The oxygen reduction and hydrogen oxidation reaction activities in the resulting cell were also enhanced by this approach.

TIECs have also demonstrated high catalytic activity and stability for the OER compared to state-of-the-art catalysts in electrolyzers[14, 22] and reversible fuel cell/electrolyzer devices.[23] The OER and ORR may include proton-coupled processes that benefit from high proton uptake in a TIEC

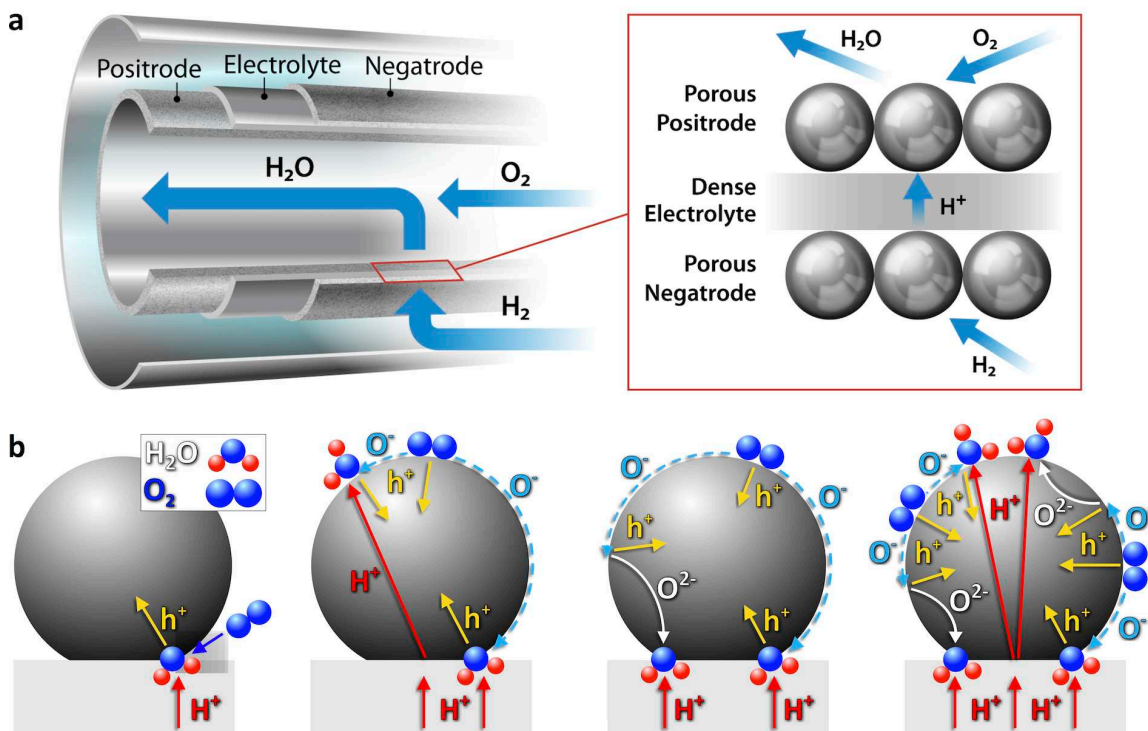


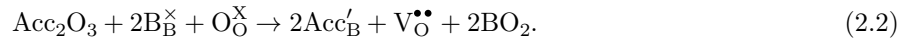
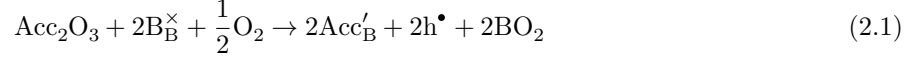
Figure 2.2 TIECs as protonic ceramic fuel cell positrodes. a) Schematic of a protonic ceramic fuel cell. Inset: Reactants and products on each side of the 3-layer device. Hydrogen is oxidized at the negatrode, and the resultant protons are conducted through the electrolyte to the positrode, where they react with oxygen (which has been reduced by the positrode) to form water. By running this process in reverse, such a device may also function as an electrolysis cell. b) Bulk and surface transport pathways and PCFC positrode reaction sites in a single particle of (from left to right) a pure electronic conductor, an  $\text{H}^+/\text{h}^+$  MIEC, an  $\text{O}^{2-}/\text{h}^+$  MIEC, and an  $\text{H}^+/\text{O}^{2-}/\text{h}^+$  TIEC. Reaction sites are represented by the presence of  $\text{H}_2\text{O}$ . Electronic conductivity is shown as p-type, although n-type may be possible.

positrode.[24, 25] Additionally, the mixed B-site occupancy in these materials enables efficient charge transfer and  $\text{O}_2$  desorption.

Perhaps most intriguingly, the coupled transport of protons, oxygen ions, and holes in TIEC materials offers opportunities to direct the electrochemical extraction or insertion of active chemical species within a membrane reactor.[26] For example, TIECs could be applied in this way to aid the formation of ethylene from methane, conversion of natural gas to syngas, or electrochemical reforming of syngas to hydrogen.[27, 28] Depending on the gas-phase partial pressures across a TIEC membrane, coupling among the three mobile defects enables the separation of oxygen, hydrogen, or steam, and it can enable unusual phenomena such as uphill diffusion.[29] Uphill diffusion forces any one of these species to be transported against its concentration gradient, which is a feature that could be useful for certain gas-separation or sensor applications.[30] The simultaneous conduction of two ionic species, in addition to electrons or holes, is key to the potential use of TIECs in these innovative applications.

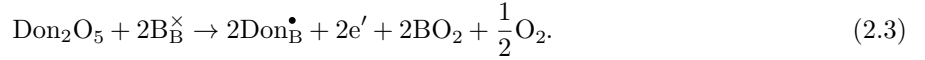
### Box 1 — Defect formation

The ideal perovskite (or perovskite-like) structure comprises cations and anions that are charge-balanced at full site occupancy. However, like many electrochemically active oxides, TIEC materials are doped with aliovalent or multi-valent cations on the A- or B-sites, which induces the formation of additional defects for charge balance. Acceptor dopants on the B-site, for example, can be charge-balanced by p-type electronic defects ( $h^\bullet$ , Equation 2.1) or oxygen vacancies ( $V_O^{\bullet\bullet}$ , Equation 2.2) as follows, in Kröger-Vink notation:[31]



Here, Acc represents the acceptor dopant and B represents the host B-site species. Similar equations can be applied to acceptor doping on the A-site.

Alternatively, n-type electronic defects ( $e'$ ) can be generated in response to donor (Don) doping (Equation 2.3):



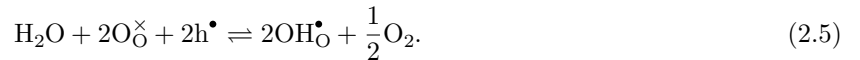
However, to our knowledge, n-type behavior in an MIEC under oxidizing conditions has only been reported once.[32] Therefore, only p-type electronic defects will be further considered in this section.

In addition to doping, the operating environment experienced by the oxide can significantly affect the defect concentrations (Figure 2.3) and the resultant transport properties. When an oxygen-deficient material is operated in a dry, oxidizing environment, the oxygen vacancies can be filled by atmospheric oxygen, according to the following reaction:



Thus, for p-type MIECs operated in this environment, the electronic defect concentration will increase with  $p_{\text{O}_2}$  and the oxygen-vacancy concentration will simultaneously decrease.

In humid gas environments, the mechanism of proton uptake is also influenced by the  $p_{\text{O}_2}$ . In humid, oxidizing environments, a material may take on protons ( $\text{OH}_O^\bullet$ ) by a redox reaction, termed hydrogenation (Equation 2.5), which is independent of oxygen vacancies:[34]



In this case, the proton carrier concentration increases with  $p_{\text{H}_2\text{O}}$ , enhancing proton conductivity, whereas electronic charge carrier concentration decreases.

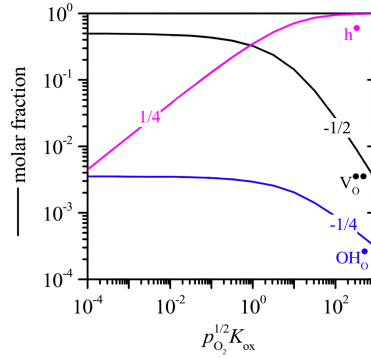


Figure 2.3 Effect of  $p_{o_2}$  on charge carrier concentration. Calculated concentrations of each charge carrier across a range of  $p_{o_2}$  for a general mixed conductor using an ideal dilute model and constant  $p_{H_2O}$ . With increasing  $p_{o_2}$ , the proton concentration decreases alongside a decrease in oxygen-vacancy concentration, while the hole concentration increases in accordance with Equation 2.4. Adapted from ref. [33]

If, instead, the material is operated in humid, reducing conditions, then proton uptake occurs by an acid-base reaction, known as hydration (Equation 2.6):[34]



In this regime, the proton concentration again increases with  $p_{H_2O}$ , whereas the oxygen-vacancy concentration decreases. Equations 2.4-2.6 are not independent because any two of them can be combined to recover the third.

The boundary between the oxidizing and reducing regimes occurs under conditions at which the defect concentrations are balanced according to  $2[O^{\bullet\bullet}] = [h^{\bullet}]$ . [34] Thus, we can see that the balance of all defects in acceptor-doped TIECs is moderated by both  $p_{H_2O}$  and  $p_{o_2}$  and is governed by the following defect equilibrium:

$$[Acc'_B] = [h^{\bullet}] + 2[V_O^{\bullet\bullet}] + [OH_O^{\bullet}] \quad (2.7)$$

The equilibrium constant (determined by standard enthalpy and entropy changes) for a given oxygen partial pressure at known oxygen-vacancy concentration can be used to determine the equilibrium hole concentration as follows:

$$K_{ox} = \frac{[O_O^{\times}][h^{\bullet}]^2}{p_{O_2}^{1/2}[V_O^{\bullet\bullet}]} \quad (2.8)$$

In the hydration regime, the equilibrium constant and oxygen-vacancy concentration may be used to determine the equilibrium proton concentration at a given water partial pressure (Equation 2.9). In the hydrogenation regime, the proton concentration at given partial pressures of water and oxygen can be

determined when the hole concentration is known (Equation 2.10).

$$K_W = \frac{[\text{OH}_\text{O}^\bullet]^2}{p_{\text{H}_2\text{O}}[\text{O}_\text{O}^\times][\text{V}_\text{O}^{\bullet\bullet}]} \quad (2.9)$$

$$K_{W/ox} = \frac{p_{\text{O}_2}^{1/2}[\text{OH}_\text{O}^\bullet]^2}{p_{\text{H}_2\text{O}}[\text{O}_\text{O}^\times]^2[\text{h}^\bullet]^2} = \frac{K_W}{K_{ox}} \quad (2.10)$$

Note that anion dopants (Ani) also affect defect concentrations. Anion dopants are typically positively charged compared to oxygen and are compensated by annihilation of oxygen-vacancy defects (Equation 2.11), creation of cation vacancies (Equation 2.12), or a combination of both.[35]



This compensation decreases the number of sites available for oxygen transport or hydration. The effects of these dopants on materials properties are further discussed in the section below on anion substitution.

## 2.4 Electronic properties of TIECs

To discover and design new TIECs, we must first understand the principles that govern charge generation and transport as well as surface reactions. These processes can be affected by chemistry, structure, and operating conditions, as detailed below.

### 2.4.1 Charge generation and transport

Broadly, ionic conduction is enabled by basic, acceptor-doped oxides with high symmetry and large free volume.[36] Proton conduction requires oxide chemistries that thermodynamically favor proton uptake. Protons locate near oxygen sites and are transferred through vibrational and rotational motion via a Grotthuss-type mechanism (Figure 2.4a).[36] Mobile oxygen ions are transferred through vacancy diffusion.[37, 38] Oxygen transport is governed by bulk diffusion, surface exchange, and grain-boundary transport, with bulk diffusion and surface exchange dominating in perovskite structures.[39]

Electronic charge carriers are transferred through the B-site to oxygen-site (B-O) bond network between aliovalent transition-metal sites and oxygen ligands.[40–42] Although there are exceptions (predominantly in materials containing a high concentration of Co or operated at high temperatures),[43, 44] a small-polaron hopping mechanism is generally accepted.[45–47] For hopping to result in conduction, the concentration of multi-valent transition metals (TMs) must be above the bond percolation threshold; this is calculated to lie between 15% and 29%, [48] a range supported by experiment.[49] Below the percolation threshold, electronic conductivity decreases sharply and the scattered TM sites become low-energy traps.[46] However, above the percolation threshold, these TM

dopants provide a low-energy conduction pathway.[45] Consequently, the percolation threshold is observed as a sharp increase in conductivity across a composition range known as the critical region (Figure 2.4b). The composition at which the critical region occurs may be decreased by ordering, clustering, preferential site occupation, or increasing temperature.[49, 50]

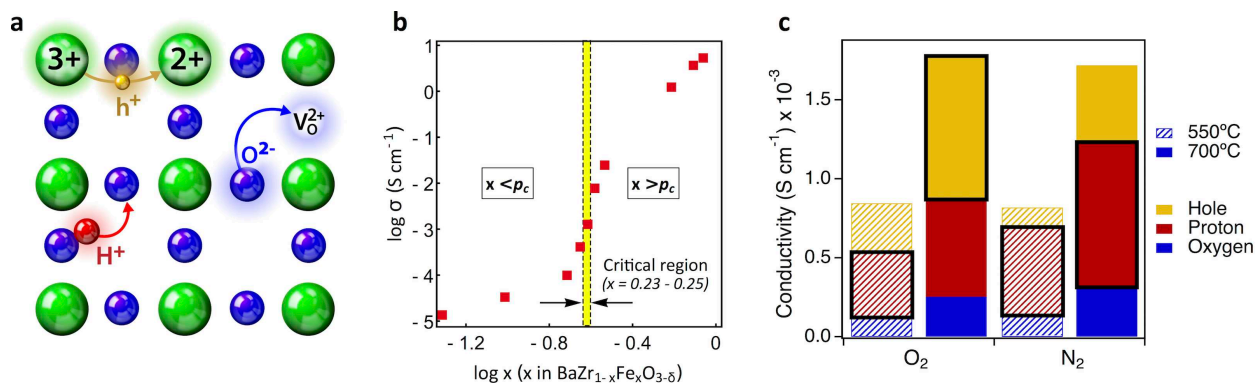


Figure 2.4 Transport in TIECs. a) Transport pathways in the B-O plane for protons ( $H^+$ ), electron holes ( $h^+$ ), and oxygen ions ( $O^{2-}$ ). B-site transition metals are represented by the large, green spheres and oxygen is represented by the small, blue spheres. b) Electronic conductivity in  $BaZr_{1-x}Fe_xO_{3-\delta}$  as a function of acceptor doping concentration on the B-site, showing a sharp increase through the critical region around the percolation threshold. Reproduced from ref. 33 with permission from Elsevier. c) Conductivity of holes, protons, and oxygen vacancies in  $Ba_{0.85}K_{0.15}ZrO_{3-\delta}$  at 550°C (striped) and 700°C (solid) under  $O_2$  and  $N_2$  atmospheres. The conductivity of the dominant carrier is emphasized by a black frame. Data from ref. [51]

While carrier concentrations are affected by composition, they also depend on temperature and atmosphere. At high temperature, the lattice dehydrates, the proton concentration decreases, and conductivity may be dominated by hole or oxygen-ion conductivity.[52] Under oxidizing conditions, oxygen fills the vacancies, which reduces oxygen transport and proton uptake and increases hole concentration. At low temperatures, the total conductivity may be significantly lower under oxidizing conditions than under reducing conditions if it is dominated by p-type small polarons, which have low mobility at low temperature. Additional information on the interplay among these defects and external parameters can be found in Box 1.

The effects of such relationships are readily observable in materials subjected to various conditions. For example, protons are the dominant carrier in  $Ba_{0.85}K_{0.15}ZrO_{3-\delta}$  in a pure oxygen atmosphere at temperatures up to 600°C, whereas holes become dominant at higher temperatures (Figure 2.4c). In a nitrogen atmosphere, protons are the dominant carrier at all temperatures, due to the much higher concentration of protons over p-type electronic charge carriers under these conditions.[51] In  $BaCe_{0.9-x}Zr_xY_{0.1}O_{3-\delta}$ , pure proton conduction is observed in a hydrogen atmosphere, whereas under oxidizing environments, electronic charge carriers are produced and the material demonstrates (p-type)

triple conduction.[53] Thus, to effectively control materials properties, one must consider chemistry and structure as well as external parameters, such as temperature and gas atmosphere.

### 2.4.2 Surface reactions

Low ORR activity has been identified as the limiting variable in electrochemical cell performance, especially at low temperatures, which makes the development of materials with considerable low-temperature ORR activity the primary research objective in this field.[20, 54, 55] Although noble metal catalysts are often used to enhance surface ORR activity, catalytically active mixed-conducting oxides have the advantage of lower cost, and they can offer high activity for both the ORR and OER, which makes them desirable electrodes for reversible electrochemical devices.[56] These surface reactions can be affected by oxygen-vacancy concentration, surface chemistry, and the gas environment. The oxygen surface-exchange reaction occurs in several steps, including adsorption of oxygen onto the surface, charge transfer, oxygen dissociation, and transfer of the surface oxygen into a vacant site in the bulk.[33] Of these, the last step is the only one that requires an oxygen vacancy.[57] Water formation and dissociation reactions that take place at the positive electrode can also occur independently of oxygen vacancies.[33] However, it is generally understood that oxygen vacancies benefit these surface reactions, although the role of these defects has not been clearly identified. It has been proposed that either the oxygen vacancies serve as surface reaction sites[15, 58, 59] or that the increase in the Fermi level associated with vacancy formation increases the rate of the charge-transfer step.[39]

Surface structure also affects ORR activity: some lattice planes have higher activity than others.[56] Therefore, surface activity (for both ORR and OER) can benefit from maximizing specific surface area of the most active surfaces by nanostructuring.[56]

For many electrochemical applications, it is essential to consider the effects of water on the surface reactions. The presence of water may enable high ORR activity, as demonstrated in some electrolyte materials.[60, 61] Upon introduction of water, the surface reaction rate rapidly increases. However, it then gradually decreases, which is likely because adsorbed water molecules inhibit further oxygen adsorption.[60] The proton conduction provided by a TIEC could address this problem by transporting protons away from the adsorption site, promoting the desorption of water back into the gas phase and leaving the surface open for additional oxygen adsorption.

Despite the potential benefits of water on surface activity, high water partial pressure can lead to rapid material degradation, prompting morphology changes, including changes in surface chemistry. For example, water may catalyze the decomposition of complex oxides to base oxides.[62] Material degradation in humid environments is both more intense and faster as temperature is lowered from 1000°C to 700°C,

indicating that it may be a particular problem for protonic ceramic electrochemical cells, which are designed to operate in an intermediate temperature range.[62, 63]

## 2.5 TIEC discovery

The basic principles required to achieve high electronic conductivity accompanied by both proton and oxygen-ion conduction are relatively straightforward, yet there have been few disclosures of triple-conducting materials until very recently. One reason for this discrepancy is that when the electronic conductivity carries 99% or more of the total current, it is difficult to identify ionic conduction using traditional electrical characterization techniques, such as electrochemical impedance spectroscopy, conductivity relaxation, or electromotive force measurements. For this reason, it is likely that there are many excellent TIEC materials hiding in plain sight because their dominating electronic conductivity obscures their ionic conduction. Thus, to discover new TIECs, an understanding is required of the chemical and structural features that enable triple conduction. From the extensive research available on proton-conducting materials and MIECs, we can establish provisional guiding principles for TIEC discovery.

The main variables that control conductivity can be related to crystal structure (including ordering in the cation or anion sublattices), ion electronegativity, and other considerations (such as electronic structure and microstructure), as detailed below. Many of these factors have contradictory effects on electronic conductivity and ionic conductivity (Figure 2.5a), making TIEC discovery an intriguing and complex challenge.

### 2.5.1 Crystal structure

For a single perovskite, high symmetry (i.e., cubic) is generally beneficial to the mobility of all three charge carriers. Highly symmetric structures exhibit isotropic transport and can also display a propensity toward greater atomic orbital overlap, which increases the extent of the electronic states in the solid and the dispersion of the electronic bands. Together, these features decrease small-polaron localization and binding energy.[47] Near-cubic symmetry and large free volume increase oxygen mobility by increasing the critical radius, thereby decreasing the degree of lattice distortion required for vacancy diffusion.[47, 64, 65] The A- and B-sites are commonly occupied by more than one cation, necessitating slight deviation from cubic symmetry to avoid local lattice strain.[64] However, as a structure deviates further from cubic symmetry, the O-O bond distances may increase, inhibiting proton mobility by increasing the hop distance. Additionally, this distortion creates a number of inequivalent oxygen sites with different enthalpies of hydration due to varying bond distances and local environments, which decreases both the proton saturation limit and mobility. Variation between adjacent oxygen sites results in isolated low-energy sites,

which may become proton and/or oxygen-vacancy traps, inhibiting the mobility of these ions.[66–68] Thus, for pure mobility considerations, a highly symmetric lattice is preferred.

A-site ordering in perovskites that contain more than one A-site species has a beneficial effect on oxygen transport and hydration, as demonstrated by  $\text{GdBaMn}_2\text{O}_{6-\delta}$ . [77] Ordered  $\text{LaBaCo}_2\text{O}_{6-\delta}$  also has a higher oxygen-vacancy concentration than the corresponding disordered phase, leading to similar or better performance than state-of-the-art PCFC positrodes.[78] This result is confirmed by molecular dynamics simulations of  $\text{GdBaCo}_2\text{O}_{6-\delta}$ , which show that, although diffusion in the ordered structure is highly anisotropic, the diffusivity is much higher than in the disordered structure (Figure 2.5b).[69]

In contrast to beneficial A-site ordering, B-site ordering reduces symmetry and proton conductivity.[67] Additionally, oxygen-vacancy ordering is detrimental for hydration of perovskites and reduces ionic conductivity.[79–81] Therefore, to maximize conductivity of each type, a material should ideally have ordered A-site occupancy with disorder on the B-site and anion sublattices.

### 2.5.2 Ion electronegativity

Electronegativity of both the cations and anions influences metal-oxygen (M-O) bond energy and oxygen-site basicity, which can significantly affect charge transport. Increased cation electronegativity and introduction of a second, more electronegative anion (such as fluorine), lower the M-O bond energy.[82, 83] Decreasing M-O bond energy can enhance oxygen-ion transport and ORR activity by decreasing the intrinsic vacancy-defect formation energy and enhancing oxygen-ion mobility and may even improve surface-exchange kinetics:[83, 84] if the bond energy is too low, then  $\text{O}_2$  adsorption is limited, whereas if it is too high, then the surface M-O bond is too stable and inhibits further catalysis.[85] Charge delocalization from vacant oxygen sites, facilitated by strong hybridization between the O 2p and metal 3d states, increases with increasing cation electronegativity and also promotes both oxygen-vacancy formation and electronic conductivity.[86] Lastly, activation energies of both proton and oxygen-ion migration decrease with decreasing M-O bond energy.[87, 88] Thus, lowering M-O bond energy by increasing average cation or anion electronegativity may enhance transport of all three carriers.

Conversely, low cation electronegativity facilitates proton uptake by increasing the oxygen-site basicity. As ionic character of the M-O bond increases, the electron density at the oxygen site increases, leading to higher basicity and increased proton uptake.[34] Low average electronegativity of A- and B-site cations results in a large negative enthalpy of hydration (Figure 2.5c), while charge delocalization, enabled by higher average cation electronegativity, may result in detrimental proton-hole interactions and lower overall proton conductivity.[79] Thus, cation electronegativity in a TIEC can simultaneously enhance and deter different aspects of the overall conductivity through opposing effects on the mobility and concentration of

each charge carrier.

### 2.5.3 Other considerations

Other factors that affect TIEC performance include electronic structure, microstructure, and gas environment. Electronic structure has been proposed as a defining factor for catalytic activity for the ORR and OER. Considerations include the energy of the O p-band center and  $e_g$  orbital occupancy of surface transition metals (Figure 2.5d).[24] Although suggested provisional principles correlate electronic structure to properties, the studies are predominantly computational. More investigation is required, including further experimental studies to corroborate results.

Microstructure is influential on TIEC performance because of the effects of surface-area-to-volume ratio on macroscopic electrochemical performance. For example, the rate-limiting steps in PCFC positrodes are typically dissociative adsorption of oxygen, bulk proton diffusion, and surface oxygen-ion diffusion.[1, 89] All of these can be promoted by maximizing surface area, which maximizes catalytically active area (for the ORR/OER) and minimizes the bulk ionic diffusion distance.

Oxygen partial pressure determines the proton-uptake mechanism, which can be either hydration or hydrogenation (Eqs. (3)-(4)). For example, proton conduction in  $\text{Ba}_{0.85}\text{K}_{0.15}\text{ZrO}_{3-\delta}$  dominates in a pure-oxygen atmosphere below 600°C, at which temperature conduction becomes dominated by holes. In a nitrogen atmosphere, proton conduction dominates at all temperatures.[51] Simultaneously increasing water pressure and decreasing oxygen pressure also causes a shift from hole-dominated to proton-dominated conductivity. Alternatively, the dominant charge carrier can be controlled by temperature. As temperature increases, oxygen-ion conductivity can overtake proton conductivity as the material dehydrates and the thermal energy becomes sufficient to activate oxygen migration.

## 2.6 Chemical design of TIECs

From a materials design perspective, the perovskite or perovskite-like structures of most TIEC materials afford great flexibility for both A- and B-site substitution, as well as anion substitution. The substituted elements can enhance phase stability,[90, 91] conductivity,[92, 93] or proton uptake.[79, 90] They can also alter the coefficient of thermal expansion[94, 95] and introduce oxygen vacancies or electronic defects into the lattice.[90, 92] Below, we discuss substitution at each site in more detail. We use the words ‘substitution’ and ‘doping’ interchangeably, which is customary in the field of TIECs. However, we note that the word ‘doping’ has a narrower meaning in the context of semiconductors, referring only to small concentrations of conductivity-promoting substitutions.[96]

### 2.6.1 B-site substitution

The B-site is commonly substituted with acceptor dopants, which may increase proton uptake by increasing oxygen-site basicity (i.e., electron density) due to lower dopant electronegativity relative to the B-site host. If the dopants are multi-valent transition metals, mobile electronic defects may be introduced; the concentration of dopant cations in the higher oxidation state is the primary contributor to the electronic defect concentration.[97] The effects of B-site doping are illustrated in two select examples below.

The  $\text{SrFe}_{1.5-x}\text{Co}_x\text{O}_{3-\delta}$  materials system demonstrates the effect of B-site TM concentrations on electronic conductivity. Although both B-site species are multi-valent TMs, electronic conductivity increases with the Co:Fe ratio (Figure 2.6a).[98] This is a result of stronger metal 3d and O 2p hybridization in Co-O versus Fe-O bonds, which is accompanied by increased charge delocalization and mobility.

Recent studies have shown that Zn, which had been previously investigated mainly as a sintering aid,[52] increases proton uptake when included as a B-site dopant in several TIEC materials systems, such as  $(\text{Ba,Sr,L a})\text{FeO}_{3-\delta}$ . [79] This increase is due to the increased oxygen-vacancy concentration that charge balances the Zn substitution for higher-valence cations, as well as the lower electronegativity of Zn compared to the B-site host. The local lattice distortion in response to Zn doping may also increase oxygen-site basicity. Of the materials analyzed,  $\text{Ba}_{0.95}\text{La}_{0.05}\text{Fe}_{0.8}\text{Zn}_{0.2}\text{O}_{2.4}$  achieved the highest proton concentration: 10% (as determined by thermogravimetric analysis at 250°C on a sample quenched from 700°C in  $p_{\text{O}_2} \leq 100$  ppm before exposure to humidified nitrogen). This concentration is greater than the proton concentration expected from the increase in charge-balancing oxygen defects, indicating additional contributions from one or more of the other above-mentioned factors. Notably, the Ba-rich compositions all exhibited higher proton concentrations than those with mixed Ba and Sr occupancy on the A-site, which can be attributed to the comparatively lower electronegativity of Ba and the corresponding increase of oxygen-site basicity, as discussed further below.

### 2.6.2 A-site substitution

The main role of the A-site in perovskite TIECs is to maintain a large unit-cell volume and inhibit structural distortion, particularly during proton transfer. For example, doping with large, acceptor cations on the A-site has been shown computationally to benefit ionic conduction in  $\text{Sr}_2\text{Fe}_{1.5}\text{Mo}_{0.5}\text{O}_{3-\delta}$  (SFMO).[99] Substituting a small amount of Ba onto the Sr site lowered the migration energy barrier. This was attributed to the increased lattice constant. Doping with the same concentration of K, which is an even larger ion, had an even greater benefit: oxygen octahedral rotation is not necessary for proton transfer in the K-doped material, whereas it is required for the undoped and Ba-doped materials. Additionally, the K-doped SFMO had significantly lower oxygen-vacancy formation energies than the other variants due to

favorable charge compensation between the holes formed upon  $K^+$  substitution for  $Sr^{2+}$  and the electrons associated with oxygen-vacancy formation.

Doping with K also significantly benefited calculated hydration energy in  $Ba_{0.5-x}K_xSr_{0.5}Co_{0.8}Fe_{0.2}O_{3-\delta}$ . The superior performance of the K-doped material was confirmed experimentally in a protonic ceramic fuel cell, in which the K-doped positrode increased the peak power density by more than 50% when operated under similar conditions at 600°C.[100] These results indicate that appropriate A-site doping can increase hydration, proton mobility, and oxygen-vacancy concentration, resulting in enhanced device performance

A study of four different  $Ba(Gd,La,Pr)(Co,Fe)_2O_{6-\delta}$  double perovskites demonstrated the effects of A-site substitution on oxygen non-stoichiometry and site basicity (Figure 2.6b). The oxygen concentrations of the Pr-containing compositions were closest to stoichiometric. To fully charge-balance the oxygen site, a portion of the cation sites must take a 4+ valence. Of the A-site species studied, this is possible only for Pr. Thus, the Pr-containing composition had the lowest concentration of oxygen vacancies. The two compositions with A-site Gd had similar oxygen non-stoichiometry regardless of the presence of La; however, the La-containing compound showed considerable proton uptake, whereas the proton uptake of the La-free compound was negligible (Figure 2.6c). Substitution of La ( $\chi = 1.1$ ) on the Gd ( $\chi = 1.2$ ) site decreases A-site electronegativity, which increases oxygen-site basicity and proton uptake.[67, 70] Although the electronegativity of Pr ( $\chi = 1.13$ ) is similar to that of La, the low oxygen vacancy concentration of the Pr-containing compositions inhibits hydration, according to equation (6). The larger radius of La compared to both Gd and Pr may further enhance the oxygen-site basicity by decreasing local lattice distortion.[79] These results demonstrate the crucial roles of both oxygen-site basicity and oxygen non-stoichiometry in facilitating proton uptake

Deficiency on the A-site can introduce oxygen vacancies, increasing both proton uptake and oxygen-ion conductivity,[101] and can increase stability against carbonate formation in Ba-based perovskites.[102] However, this deficiency also reduces electronic charge carrier concentration.[102] Additionally, if the A-site deficiency is compensated by the B-site species, both the oxygen-vacancy concentration and the degree of hydration will decrease.[103]

### 2.6.3 Anion substitution

Substitution on the anion site has recently gained interest as an alternative doping strategy to the more common cation doping. Anion dopants are also mobile in perovskites, thus broadening the scope of TIECs. However, the high mobility of certain anionic dopants may make them difficult to retain at high temperatures.[93] Partial substitution of oxygen with anions of lower valence and higher electronegativity (such as F or Cl) benefits both oxygen-ion and proton mobility by decreasing the oxygen-site electron

density. This decreases the bond energy between oxygen and the adjacent cations and increases oxygen exchange kinetics and mobility.[83] In response, O-H bond distance increases, decreasing the proton hop distance and easing proton transfer.[104] Ionic mobility is further increased by repulsion between the different species on the anion sublattice.[81, 105] Finally, when the anion defect is charge compensated by both oxygen and A-site vacancies, the oxygen mobility is greater than when the defect is compensated by oxygen vacancies alone.[93]

In contrast, anionic dopants can decrease electronic conductivity and all charge-carrier concentrations. As concentration of the lower valence anion increases, oxygen conductivity initially increases, as a result of increased mobility, then decreases as the effect of the decreased vacancy concentration takes over (equation (11)).[88] A similar dependence is observed for ORR catalytic activity.[83] In materials that require a change in oxygen coordination to facilitate ionic conduction, doping with fluorine decreases proton concentration. For example, the InO<sub>4</sub> tetrahedra of the brownmillerite structure of BaInO<sub>5- $\delta$</sub>  transform to octahedra as oxygen vacancies are filled during hydration. These transformations facilitate nearly complete hydration.[106] Doping with fluorine decreases the degree of hydration by inhibiting the change in coordination.[81, 105] However, if the symmetry of a material is not affected by hydration, then a doped sample can achieve the same degree of hydration as an undoped sample.[105]

In most materials studied so far, anion doping either increases the symmetry of the structure or has no measurable effect.[83, 88, 91] However, of particular interest are the effects of fluorine on symmetry in BaInO<sub>5-x</sub>F<sub>x</sub> (an MIEC with perovskite structure) and La<sub>2</sub>Mo<sub>2</sub>O<sub>9-0.5x</sub>F<sub>x</sub> (an oxygen conductor with non-perovskite structure).[80, 81] At high temperature, each of these materials transitions to a cubic phase, which is accompanied by an increase in conductivity. In both cases, doping with fluorine decreases the transition temperature, which increases total conductivity at lower temperatures in the doped material, compared to the undoped oxide. Thus, anion doping can have positive effects on ionic mobility and symmetry, but can negatively affect charge carrier concentrations.

## 2.7 Research directions

The discussion above highlights the complex effects of various chemical factors on TIEC design. Many studies of TIEC materials have focused on understanding the properties of a particular composition or on property variation within a composition range, but the fundamental science of underlying composition-performance relationships is not yet fully understood.[89] Recently, a number of computational studies have sought to establish these fundamental principles;[86, 99, 107, 108] however, additional experimentation is needed to complement these theoretical findings. To reliably explain trends, such experimental studies must be highly systematic to ensure that property variation among samples is

determined solely by compositional variation and is not due to uncontrolled factors such as synthesis method, microstructural variation, or differences in instrumentation or technique.

Broad compositional investigations are enormous tasks if approached with serial synthesis and characterization methods. Additionally, synthesis and characterization of large compositional spaces present significant challenges for data analysis. One solution currently being pursued by the authors applies combinatorial experimentation in conjunction with machine learning. We have synthesized and characterized more than one thousand unique, potential TIEC compositions by combinatorial pulsed laser deposition of thin films and combinatorial characterization methods. The data will be fed into a machine learning model to promote understanding of the chemical characteristics that determine transport properties. Additional research areas that will facilitate rapid development and application of these materials include developing characterization methods to effectively deconvolute contributions of individual charge carriers to conductivity, improving chemical stability of TIEC-based positrodes, and extending the relevant temperature for ORR/OER below 400°C.

### **2.7.1 Deconvolute charge-carrier contributions**

One major challenge to the fundamental understanding of TIECs — and, therefore, to new TIEC material development — is the lack of efficient characterization techniques that effectively separate charge carriers. Several methods have been applied to MIEC membranes.[109] Some methods isolate one carrier, whereas others can separate two; however, the addition of a third carrier further complicates disentanglement. In Table 2.1, we discuss the benefits and challenges of characterization methods commonly used for mixed conductors.

Currently, the most common approaches either combine various characterization methods or use a single method under a variety of limiting conditions that enable one carrier to dominate conduction. By comparing the resultant data, the carriers are separated analytically. For example, impedance spectroscopy is employed to measure the total conductivity of the isolated material, and electronic conductivity is determined by a direct-current measurement (when electronic conduction dominates transport); the results are then compared to the impedance of a device with a TIEC membrane layer and blocking electrodes on either side. A similar approach can be taken using the electromotive force method.[110] Such approaches require multiple steps and may still be unable to isolate proton conductivity. Alternatively, detailed chemical thermodynamic transport models that include all three charge carriers can be constructed and used to fit published conductivity data;[111] however, even these models generally cannot produce a unique solution for the individual transport of each of the three carriers. Consequently, new approaches are required.

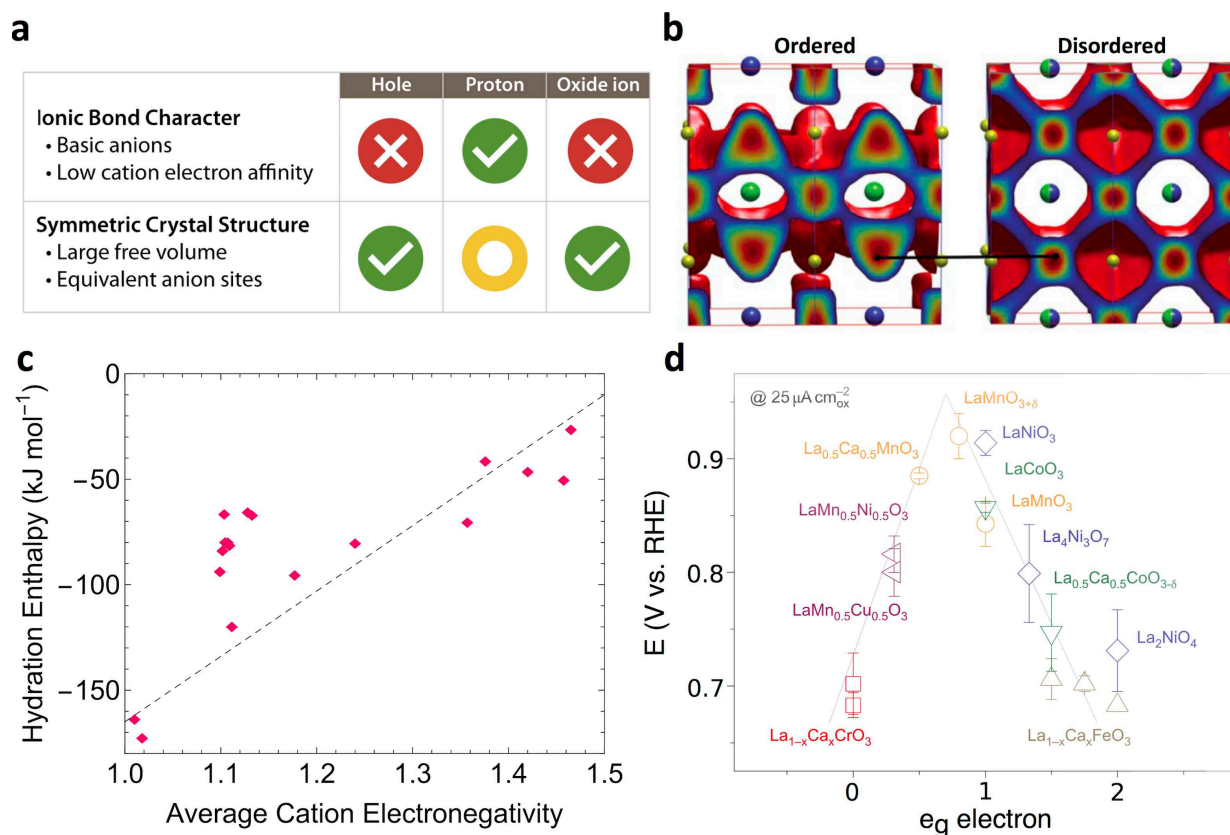


Figure 2.5 Factors that influence TIEC performance. a) Variables that have either positive (✓), negative (✗), or mixed (○) effects on the transport of each of the three charge carriers. The underlying details are discussed in the text. b) Oxygen density profiles from molecular dynamics simulations, suggesting a highly anisotropic profile in ordered  $\text{GdBaCo}_2\text{O}_{5.5}$ . Oxygen migration in the ordered case is confined to oxygen sites in the planes between Gd (green) and Co (yellow), whereas the oxygen near Ba (blue) does not contribute to conduction. In the disordered case, the density profiles (and resultant migration pathways) are isotropic. Republished with permission of the Royal Society of Chemistry, from ref. [69]; permission conveyed through Copyright Clearance Center, Inc. c) Hydration enthalpy increases with an increasing average of A- and B-site Rochow-Allred cation electronegativities, as shown here for various perovskites. The most favorable (large, negative) enthalpy corresponds to the lowest average electronegativity. Dashed line serves only as a guide for the eye. Data from ref. [67] and refs. [8, 70–75]. d) Dependence of ORR catalytic activity (defined by the overpotential compared to a reference hydrogen electrode (RHE)) on average  $e_g$  orbital occupancy of the B-site transition metal, indicating an ideal occupancy close to 1. Republished with permission of Royal Society of Chemistry from ref. [76]; permission conveyed through Copyright Clearance Center, Inc.

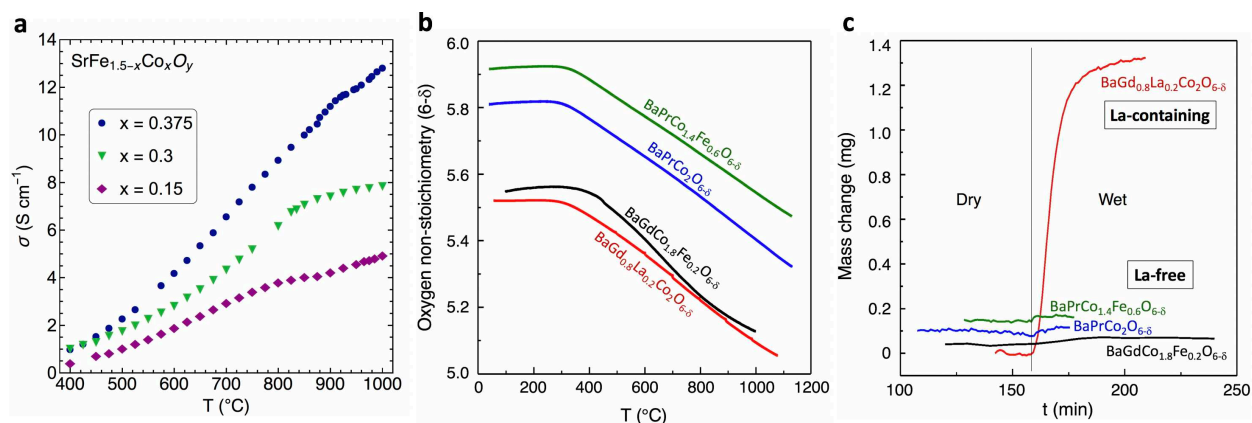


Figure 2.6 Composition effects on electronic conductivity, oxygen non-stoichiometry, and proton uptake. a) Conductivity increases with Co:Fe ratio due to increasing metal 3d and O 2p hybridization in SrFe<sub>1.5-x</sub>Co<sub>x</sub>O<sub>y</sub>. Adapted from ref. [98] with permission from Elsevier. b) Temperature-dependent oxygen non-stoichiometry for various Ba(Gd,La,Pr)(Co,Fe)<sub>2</sub>O<sub>6- $\delta$</sub>  compounds. Adapted from ref. [70] with permission from Elsevier. c) Mass change in 2.5-g powder samples of compositions from part (b) across a transition from dry to humid atmosphere over time. The La-containing composition shows observable mass increase upon exposure to humid atmosphere, indicating greater proton uptake than in the La-free compositions, which show negligible mass gain. Adapted from ref. [70] with permission from Elsevier.

Table 2.1 Common characterization techniques for mixed-conducting oxides

Technique	Extracted Variables	Challenges	Solutions
Electrochemical impedance spectroscopy[112, 113]	Ionic and electronic conductivities; bulk and surface resistances; chemical diffusion coefficients; electronic charge-carrier concentration; mobility and activation energies for electron and ion migration; reduction entropy and enthalpy[19, 112]	Time constants of physically distinct processes may be too similar to reliably separate using equivalent circuit models, which are not unique solutions[114] Individual carrier resistances can only be extracted if both single-carrier and mixed-conducting regimes are accessible[112]	Higher-resolution analysis by distribution of relaxation times distinguishes between processes with similar time constants without pre-existing models[114, 115]
Conductivity relaxation by four-point probe[116–118]	Chemical diffusion coefficient; surface exchange coefficients[116, 119]	Accurate results depend on nearly instantaneous reactor flush[120] Requires dense samples to minimize microstructural effects on results[121] May not distinguish between reaction steps or between charge carriers[122] Thermodynamic factor is required to calculate oxygen diffusion coefficient from chemical diffusion coefficient[123–125]	Sufficient gas flow rate avoids changes in oxygen activity due to uptake and release of oxygen from sample[126] Flush time correction[120]
Mass relaxation by thermogravimetric analysis[16, 124]	Mass-action constants; hydration enthalpy and entropy; defect concentrations; chemical diffusion coefficients; thermodynamic factor[8, 125, 127, 128]	Yields only changes in (rather than absolute values of) oxygen non-stoichiometry[109, 129] May be time consuming, depending on required range of measurement temperatures and gas atmospheres and on length of equilibration time[130] Requires dense samples[8]	A chemical method, such as X-ray photoelectron spectroscopy or titration, can establish initial oxygen non-stoichiometry[109]
Electromotive force[131]	Transport number for each charge carrier[131]	Multinary compounds with more than one mobile species show path- and time-dependence of open-circuit voltage[132]	Careful control of gas partial pressures on each side of the material [110, 133, 134]
Tracer exchange and depth profiling with secondary-ion mass spectrometry[58, 123, 135–137]	Tracer diffusion coefficient; activation energy of diffusion; surface exchange coefficient[138]	Costly and time consuming[119, 139] Requires very dense samples[138, 139] Cannot distinguish between surface reaction steps[140]	Steady-state isotope-exchange method deconvolutes reaction steps[140]

### 2.7.2 Improve chemical stability

Although compounds containing Ba or Sr on the A-site typically exhibit the highest conductivity, their stability is often compromised by undesirable reactions between the A-site cation and process gases, inhibiting long-term performance.[58, 141] Stability can be improved by doping, but further development is needed to ensure reliability. In addition, materials doped with B-site cobalt consistently demonstrate high electronic conductivity and ORR activity,[15] but exhibit notoriously low chemical stability and detrimentally high thermal expansion. Alternative multi-valent TMs that enable equivalent or superior performance must be identified.

Chemical stability can also be enhanced by optimizing the tolerance factor. Perovskite stability is generally considered to be tied to the tolerance factor ( $t$ ), which may range as low as 0.85 and as high as 1.04 for the perovskite structure, with the cubic case defined as  $t = 1.30$ . [37, 87] Calculated formation energies confirm that the perovskite structure becomes more favorable with increasing  $t$  up to 1. [142] A tolerance factor in this range does not ensure stability,[143] but doping with combinations of cations that bring the tolerance factor closer to 1 can improve chemical stability.[144]

### 2.7.3 Enable ORR/OER below 400°C

Operation of a TIEC has been demonstrated at temperatures as low as 350°C, but most materials studied so far have inadequate catalytic activity and conductivity for practical application at such temperatures.[6] Reducing electrochemical device operating temperatures will reduce cost, increase market viability, and make portable and transport applications possible.[15] The limiting factor during low-temperature operation is typically oxygen catalysis. Consequently, this goal may be achieved by incorporating results from recent advances in low-temperature oxide ORR/OER catalysis for alkaline fuel cells and electrolyzers. Such studies have broadly focused on eliminating or significantly reducing precious-metal usage by creating intricate, stable structures that maximize surface area or specific catalytic activity and by inhibiting coarsening to maintain high surface area.[145] Additionally, these studies have found that catalytic activity may be anisotropic and can, therefore, be maximized by orienting materials such that surfaces comprise lattice planes with the highest catalytic activity.[56]

### 2.7.4 Discover and design n-Type TIECs

Another important future challenge for designing TIEC materials is the development of an n-type TIEC. Extrinsic donors may generate n-type carriers in either pure electronic conductors or  $O^{2-}/h^+$  MIECs.[32, 42, 146] However, even donor doping does not ensure n-type electronic conductivity because donor dopants can instead be compensated by cation vacancies.[147] Consequently, a more fundamental

approach is required.

In solids, the charge state of a hydrogen interstitial depends on the Fermi energy of the host material.[148] Hydrogen interstitials can act as bare protons ( $H^+$ ) if there are empty states available at or above the Fermi energy and if the energy of these states is lower than the s-atomic orbital of the hydrogen atom. If, on the other hand, there are filled electronic states at higher energy than the hydrogen atomic orbitals, then charge will transfer from the host material to the hydrogen interstitial, effectively making it an  $H^-$  ion. This behavior of hydrogen interstitials — acting as  $H^+$  or as  $H^-$  ions, depending on the Fermi energy of the host — is known as ‘amphoteric doping’ and has been thoroughly investigated because of its technological importance in the semiconductor industry.[149]

The  $H^+/H^-$  hydrogen transition level has been shown to lie about 4.4 eV below vacuum across many classes of materials.[148] Thus, an n-type proton-conducting materials system would require a conduction band more than 4.4 eV below vacuum so that interstitial hydrogen behaves as a bare proton and the material’s Fermi energy can be raised (by appropriate doping) close to the conduction band, rendering the material n-type (Figure 2.7). Intrinsic energy-band alignment of various functional oxides has been investigated experimentally[141] and computationally,[150] and it can be used for n-type TIEC material selection.

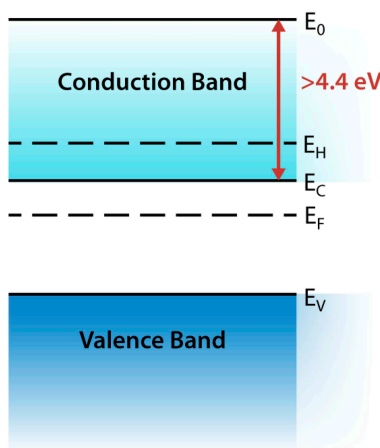


Figure 2.7 Conceptual band diagram of an n-type TIEC. The material should have an electron affinity greater than 4.4 eV so that the  $H^+/H^-$  transition level lies within the conduction band.

Although there are no rigorous physical restrictions on where the conduction and valence bands of materials lie, the p-type electronic conductivity of presently known TIECs indicates that their valence-band maxima lie less than 4.4 eV below vacuum. As a result, the bare protons coexist with electron holes, and the conductivity is usually accomplished through hole (rather than electron) doping.

However, in principle, triple conduction can be realized with electrons as the primary carriers if the design principle is fulfilled of having the conduction-band minimum lower than 4.4 eV relative to vacuum. Such behavior may be challenging to achieve, particularly among traditional perovskite-derived oxides.

Combining a first-principles approach[151] with the recently successful automation of defect and doping calculations[152] could assist in the search for such materials systems across large chemical spaces and, more broadly, in the rational design of interstitial defect behavior.[153]

## 2.8 Summary and outlook

Most known TIEC materials are mixed proton, oxygen-ion, and hole conductors that have been developed primarily as fuel cell positrodes. To date, the highest performance for this application has been observed for Ba-based materials with high multi-valent transition-metal doping and inclusion of Zn. However, many other applications can be envisioned for these versatile materials, including reversible devices, p-n heterojunctions, and membrane reactors.

Due to their predominantly perovskite-like structures, TIECs readily accommodate both cation and anion substitution. The defect concentrations and resultant properties of these materials are determined by occupancy ratios and by the atmosphere to which they are exposed. Defect mobility can be influenced by both composition and structural features, such as symmetry and cation ordering. Thus, the overall conductivity of each carrier type can be manipulated by a combination of composition, structure, and operating conditions. Additionally, appropriate manipulation of the conduction-band energy minimum may open new opportunities for designing n-type, rather than p-type, TIECs.

As this review illustrates, TIEC materials offer the prospect for both improved performance in existing devices and development of novel devices — but there are still challenges to overcome. First, development of more efficient and direct characterization methods for studying these materials will improve our fundamental understanding of their transport behavior, allowing deliberate manipulation of properties to suit targeted applications. Next, extending the operable temperature range will further broaden TIEC applications. Finally, improving chemical stability of these complex materials, which often operate in harsh conditions, is a prerequisite to broad industrial acceptance.

CHAPTER 3  
INSTRUMENT FOR SPATIALLY RESOLVED, TEMPERATURE-DEPENDENT  
ELECTROCHEMICAL IMPEDANCE SPECTROSCOPY OF THIN FILMS UNDER LOCALLY  
CONTROLLED ATMOSPHERE

Meagan C. Papac,<sup>4,5</sup> Kevin R. Talley,<sup>7</sup> Ryan O’Hayre,<sup>8</sup> and Andriy Zakutayev<sup>7,8,6</sup>

### 3.1 Abstract

We demonstrate an instrument for spatially resolved measurements (mapping) of electrochemical impedance under various temperatures and gas environments. Automated measurements are controlled by a custom LabVIEW program, which manages probe motion, sample motion, temperature ramps, and potentiostat functions. Sample and probe positioning are provided by stepper motors. Dry or hydrated atmospheres (air or nitrogen) are available. The configurable heater reaches temperatures up to 500°C although temperature at the sample surface is moderated by gas flow rate. The local gas environment is controlled by directing flow toward the sample via a glass enclosure that surrounds the gold wire probe. Software and hardware selection and design are discussed. Reproducibility and accuracy are quantified on a Ba(Zr,Y)O<sub>3-δ</sub> proton-conducting electrolyte thin film synthesized by pulsed laser deposition. The mapping feature of the instrument is demonstrated on a compositionally graded array of electrocatalytically active Ba(Co,Fe,Zr,Y)O<sub>3-δ</sub> thin film microelectrodes. The resulting data indicate that this method proficiently maps property trends in these materials, thus demonstrating the reliability and usefulness of this method for investigating electrochemically active thin films.

### 3.2 Introduction

Electrochemical impedance spectroscopy is a common tool for measuring frequency-dependent electronic responses in materials. It has been applied to various classes of materials, including mixed ionic-electronic conductors,[112] superconductors,[154] dielectrics,[155] ferroelectrics,[156] and solar cells.[157] Impedance is measured either in potentiostatic mode, in which an alternating voltage is applied and the resulting current is measured, or galvanostatic mode, in which an alternating current is induced and the required potential is measured. Such measurements yield the amplitude and phase offset between the signal and the response. Different reaction or diffusion processes typically have different time constants, which are observed as separable features in plots of frequency-dependent impedance. Consequently, the technique can be used to

---

<sup>4</sup>Materials, Chemical, and Computational Science directorate, National Renewable Energy Laboratory

<sup>5</sup>Department of Metallurgical and Materials Engineering, Colorado School of Mines

<sup>6</sup>Author for correspondence

distinguish between various processes related to surfaces, interfaces, and the bulk based on variation in their time constants.[158] By measuring under various temperatures or gas environments, additional information can be obtained. Temperature-dependent results allow the calculation of activation energies. Measurements under various gas atmospheres provide insight into properties such as ionic conductivity or catalytic activity and assist in identifying the dominant electronic carrier (electrons or holes), as these variables are all affected by defect concentrations in the material and, thus, by gas partial pressures.[159]

A growing interest in high-throughput experimentation has created demand for spatially resolved, automated characterization tools.[160–162] Combinatorial samples (known as ‘libraries’) are typically thin films deposited by physical vapor deposition methods, such as sputtering or pulsed laser deposition (PLD). By these methods, many unique material specimens can be deposited as a single library in a short period of time. Gradients in chemical composition or in synthesis conditions generate gradients in sample properties. One major goal of high-throughput experimentation is to quickly screen a library to identify trends in these properties and locate compositional or experimental parameter spaces that warrant more thorough investigation. Ideal characterization tools must be spatially resolved and automated, with minimal input from the user. Such experimental methods inform and expedite the materials discovery process.

Automated impedance spectroscopy has been used to measure fuel-cell electrode materials in the form of thin films that have been fashioned into microelectrodes.[163–168] Beneath the electrode film is an electrolyte layer to form a half fuel cell. An anode or cathode layer is sometimes added on the opposite side of the electrolyte to make a full or symmetric fuel cell, respectively. The bottommost layer of the stack is an electronically conducting counter electrode. Microelectrodes are synthesized in a multi-step process, including thin film deposition followed by photolithography and ion-beam etching.[163–168] The microelectrodes are typically 20 to 500  $\mu\text{m}$  in diameter, although those 100  $\mu\text{m}$  and larger are most consistently measurable, due to the uncertainty in alignment of the probe with smaller microelectrodes in existing measurement instruments.[165] Due to the small diameters of both the electrodes and the probe tip, a microscope is required to align the probe with the sample. Additionally, for instruments that have environmental gas control, the sample and probe must be completely enclosed within a vacuum chamber.

Here, we describe an approach to spatially resolved electrochemical impedance measurements, or impedance mapping, that combines features of previous approaches, including spatial resolution, automation, and temperature control, in a modular design that can be reconfigured to suit researchers’ needs. Notably, local control of the gas environment is achieved via an encased probe design. The instrument is demonstrated on a family of materials of interest for protonic ceramic fuel cells,  $\text{Ba}(\text{Co,Fe,Zr,Y})\text{O}_3$  (BCFZY), which includes a widely studied proton conductor,  $\text{BaZr}_{0.8}\text{Y}_{0.2}\text{O}_3$  (BZY20), and a known triple ionic-electronic conductor,  $\text{Ba}(\text{Co}_{0.4}\text{Fe}_{0.4}\text{Zr}_{0.1}\text{Y}_{0.1})\text{O}_3$  (BCFZY4411). The high, stable

proton conductivity of BZY20 makes it a good candidate for proving accuracy and repeatability of measurement and analysis methods. Triple-conducting BCFZY4411 facilitates mixed transport of electrons, protons, and oxygen ions and has high activity for the oxygen reduction reaction.[6] These transport properties are moderated by composition, temperature, and gas environment. Thus, a compositionally graded BCFZY thin film was selected to demonstrate the instrument’s mapping capability. Temperature-dependent ionic conductivity values for BZY20 extracted by this instrument are consistent with those obtained from previous studies of this proton conductor. Impedance measurements of compositionally graded BCFZY thin films demonstrate the instrument’s ability to map a range in electrochemical properties at different temperatures and gas environments. The instrument presented here provides facile screening of ionic conductivity and electrocatalytic activity as a function of spatially graded variables alongside measurement temperature and gas environment, thereby demonstrating the utility of this measurement method for combinatorial experimentation.

### **3.3 Design of the instrument**

#### **3.3.1 Design overview**

The primary requirements for the instrument are that 1) it must reliably and steadily heat the sample, 2) it must provide an equilibrated gas environment under which to measure the sample, and 3) it must enable electrical contact with the sample. The three primary components for controlling temperature, establishing gas flow, and electrically probing the samples are shown in Figure 3.1.

Sample temperature is controlled by a heated stage, which consists of two heater cartridges embedded in a stainless-steel block (Figure 3.1a). A thermocouple positioned directly between the two heater cartridges provides feedback to the temperature controller. A block of thermal insulation works in conjunction with an underlying water-cooled stage to minimize heat loss and avoid thermal damage to any mechanical parts. A stainless-steel clamp holds the sample in place and provides electrical contact with the outer edge of the conductive substrate. It is electrically isolated from the base plate of the hot stage by alumina standoffs. Electrical contact with the sample is provided by a gold wire probe tip. A glass tube surrounds the probe tip and directs gas toward the sample during measurement. Additional details of electrical and gas components of the instrument are discussed in Section 3.3.2 and Section 3.3.3 and illustrated in Figure 3.1b and Figure 3.1c, respectively.

One advantage of this instrument, over others with a similar purpose, is its simple and configurable design. This design allows the user to easily change the probe tip, the gas flow area, or the sample dimensions by replacing or modifying any of the custom-built parts. A second advantage is local gas control, which can improve reliability of benchtop measurements (Appendix A, Figure A.2) and facilitate

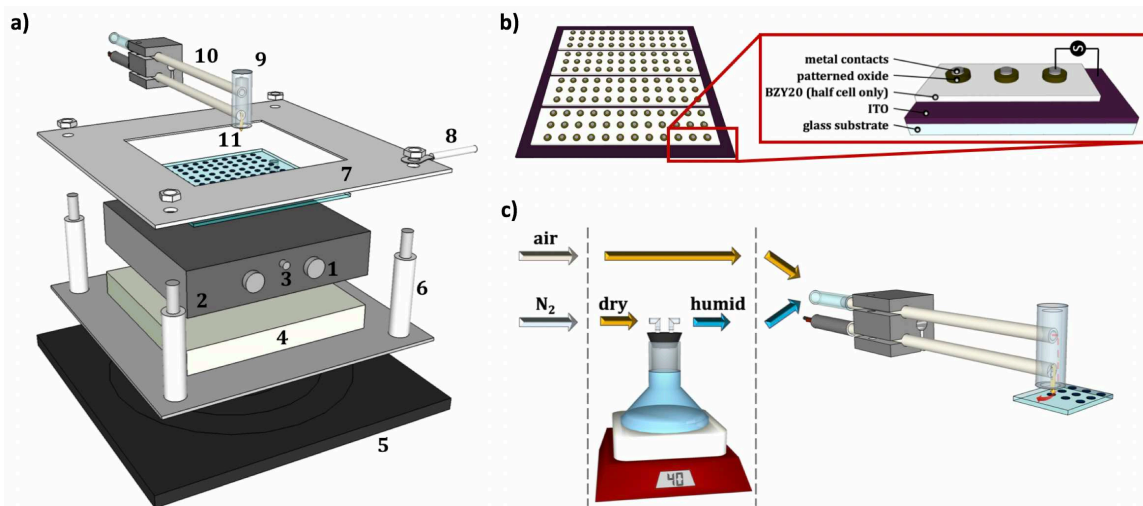


Figure 3.1 Instrument and sample layout. a) Design of the hot stage featuring 1) heater cartridges in 2) a stainless steel heater block, 3) a thermocouple to monitor temperature, 4) insulation to minimize heat loss, 5) a cooled x-y stage, and 6) alumina standoffs isolating 7) the top clamp, which makes electrical contact to the counter electrode. Current is carried from the top clamp by 8) an eye connector in electrical contact with the corner of the clamp. Gas flows into 9) a glass cylinder through 10) an alumina tube. A second alumina tube carries the 11) gold probe wire into the cylinder. b) Illustration of a thin film sample stack, showing the metal contacts deposited on patterned electrodes atop the BZY20 electrolyte layer with ITO exposed around the perimeter for electrical contact with the top clamp. For the electrolyte samples, the cathode layer is omitted. A glass substrate supports the device. c) Flow of either air or  $N_2$  passes through the probe tip, which moves in the z-direction. The gas may be humidified prior to flowing through the probe.

screening of materials kinetics. In this design, only the portion of the sample that is immediately under the probe is directly subjected to the gas environment at any given time. Thus, a microelectrode could, for example, be measured under dry gas and then repeatedly under humid gas as a function of time to observe how quickly, and at which frequencies, the impedance changes upon exposure to the humid environment. Localized gas flow immediately changes the gas environment for the contact being measured and ensures that this could be repeated for contacts across the library because they are not all simultaneously equilibrating to the change. Conversely, localized gas flow could be seen as a disadvantage because a dwell is required at each sample point for gas equilibration. This increases the measurement time for each point at a set gas environment compared to an enclosed measurement instrument. Additionally, the maximum achievable relative humidity of the gas environment in the current design is limited, since the gas lines and probe operate close to room temperature. As the relative humidity approaches 100%, water droplets may form along the gas line and drip onto the sample. A hydrophobic gas line is used to discourage droplet formation.

### 3.3.2 Electrical probing of the sample

Here, we use an out-of-plane measurement configuration (Figure 3.1b) to demonstrate functionality of this instrument. This configuration enables a two-electrode measurement because the large area of the counter electrode results in negligible impedance compared to that of the sample electrodes.[163, 169] For a two-electrode measurement, the working and working sense leads are combined as the working electrode. The counter and reference leads are combined as the counter electrode. An out-of-plane configuration may be preferred for measuring thin films deposited by PLD, which typically produces films with vertically aligned columnar grains.[170] When a film is very thin ( $<100$  nm), pinholes in the film may lead to short circuiting between the probe and counter electrode. However, when pinholes are avoided, measurement down the length of the columnar grains yields an impedance response that is more similar to the bulk than the response measured in a cross-grain configuration.[171]

Gold wire (0.455 mm diameter, Surepure Chemetals, USA) is chosen to electrically probe the sample because of its ability to avoid oxidation under a wide range of gas environments and because it is not catalytically active.[172] The gold electrical probe tip is surrounded by a custom glass cylinder (Precision Glass Blowing, USA) that has an open bottom for gas egress (Figure 3.1c) and a closed top to direct gas flow toward the sample. The glass cylinder has two vertically aligned holes in the side, each fitted with an alumina tube. Gas flow is directed through the upper tube, while the lower tube carries the gold wire. A u-bend in the end of the gold wire acts as the electrical probe tip. An earlier design employed the blunt-cut end of a wire as the probe tip; however, it was difficult to execute repeatable contact between the probe and the sample with this design. Additionally, the edges of the tip scratched the samples and compromised the films during measurement. The u-bend tip addresses these issues and has been successfully employed in other contact-sensitive measurement applications.[173] The opposite end of the gold wire is connected to a coaxial cable that connects it to both the working and working sense electrode leads. A stainless-steel clamp contacts the perimeter of the continuous counter electrode layer and holds the sample in place. The lead from the sample counter electrode is connected to both the counter and reference electrode leads from the potentiostat. Impedance is measured by an Interface 1000 potentiostat (Gamry, USA) that is run in potentiostatic mode. This instrument has  $\pm 1$   $\mu\text{V}$  applied voltage accuracy, 12.5  $\mu\text{V}$  resolution, and  $\pm 5$  pA measured current accuracy.

In addition to the out-of-plane measurement geometry described here, where voltage is applied perpendicular to the sample surface, the voltage can, in principle, be applied parallel to the sample surface resulting in an in-plane measurement geometry. For in-plane measurements, the voltage is applied across the width of the grains, measuring a series of bulk and grain boundary impedances. The typically high

impedance of grain boundaries results in higher measured impedance in this configuration.[171] Additionally, high interfacial conduction at the film-substrate interface can provide a parallel conduction pathway, complicating results. However, since the in-plane configuration measures across grain boundaries, it can be useful for studying both bulk and grain boundary contributions to the impedance, provided the stray capacitance is managed by minimizing the distance between electrodes.[174] To enable such in-plane measurement in the future, the instrument presented here can be modified by inserting a second gold wire through a second, electrically isolated hole in the alumina tube.

### 3.3.3 Temperature and gas flow control

Sample temperature is moderated by two 120-Watt cartridge heaters (MISUMI, USA) embedded in a stainless-steel block (Figure 3.1a). The heaters are controlled by a temperature controller (Cole-Parmer, USA), which receives feedback from a K-type thermocouple installed between the two cartridge heaters. The heater block sits atop heat insulating plates (MISUMI, USA) to minimize heat loss through the bottom of the block and to prevent the cooled x-y stage from overheating. The insulating layer is 10 mm thick with thermal conductance equal to  $1.1 \times 10^{-4} \frac{W}{K}$ . Temperature calibration experiments indicated that the sample surface is cooler than the heater setpoint due to heat dissipation by the glass substrate (Figure 3.2a) and that the surface temperature stabilizes after a few minutes (Appendix A, Figure A.3). Consequently, the sample is equilibrated for 4 minutes after each temperature ramp to ensure constant sample temperature before electrical measurements begin.

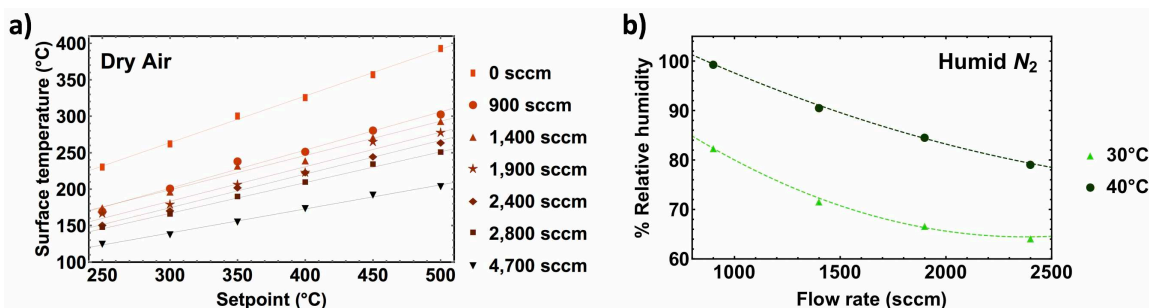


Figure 3.2 Calibration curves for temperature and humidity showing a) the difference between setpoint temperature and surface temperature at various gas flow rates. The difference increases with increasing gas flow rate and deviates from the setpoint under all flow rates. b) Relative humidity increases with increasing temperature and with decreasing flow rate.

Gas flows down an alumina tube and through the glass cylinder that surrounds the probe tip, directing the gas flow toward the sample (Figure 3.1c). The inner diameter of the cylinder is 4 mm and its lower edge rests 1mm above the sample when the probe tip is in contact with the sample. This enables consistent gas flow without inhibiting user visibility during alignment. Gas flow decreases the surface temperature

(Figure 3.2a). Thus, an additional dwell at each contact is implemented for measurements taken under gas flow in order to equilibrate both the surface temperature and the gas atmosphere. The instrument has access to both air and  $N_2$  and they can be supplied dry or humidified. During a dry measurement, gas flows directly down the gas line, through the probe, and over the sample. For measurements under humidified atmosphere, the dry gas upstream of the sample is directed through an Erlenmeyer flask that contains deionized water and rests on a hot plate. Humidity can be moderated by varying the hot plate setpoint and the gas flow rate (Figure 3.2b). The effects of these two variables on the relative humidity of the gas leaving the probe have been calibrated so that the relative humidity of the measurement environment is known. A sudden change in either of these variables causes a gradual change in relative humidity of the gas in the line (Appendix A, Figure A.5). Consequently, the humidified gas is allowed to flow for 30 minutes before measurement under newly adjusted settings in order to stabilize humidity.

### 3.3.4 Data collection

Aside from gas flow, which is adjusted manually by the user, all critical functions of this instrument are controlled by a custom LabVIEW program that interfaces with the temperature controller, the x-y stage, the z-axis probe actuator, and the potentiostat to coordinate measurement of each sample point at all temperatures (Figure 3.3). During setup, the user selects a configuration file containing x,y coordinates for each measurement position and then defines three reference coordinates on the sample. The three-dimensional, relative coordinates of all sample points are calculated by combining the coordinates in the file with the plane defined by the reference coordinates. The sequence of setup and measurement steps is outlined in Figure 3.3. The user procedure for mapping a library includes 1) loading the sample and securing the sample clamp, ensuring that the clamp is in contact with the counter electrode; 2) defining measurement coordinates, a data export path, a list of measurement temperatures, dwell times, and a frequency range; and 3) aligning the sample positions with the probe so that the software can define the complete coordinate grid.

The procedure followed by the software includes 1) ramping to a setpoint and dwelling at that temperature for a user-defined period of time; 2) moving the x-y stage and z-axis probe actuator to the appropriate coordinates and establishing contact between the sample and the probe; 3) dwelling in this position for a user-defined period of time to equilibrate the gas environment; and 4) applying potential and measuring current response across a range of frequencies to acquire a complete impedance spectrum at that point. Once a spectrum has been collected, the data is exported to the user-defined file path. When data collection is complete, the heater is cooled to room temperature.

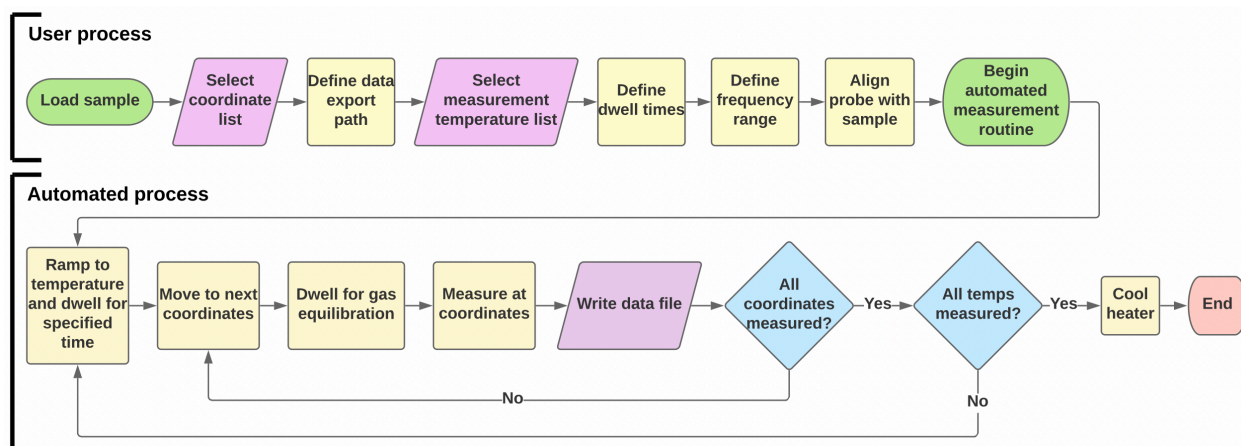


Figure 3.3 Work flow for the user and for the LabVIEW-controlled, automated process.

### 3.3.5 Data analysis

The raw impedance data is output from LabVIEW in a format that can be fit with equivalent circuit models (ECM) in EChem Analyst (Gamry, USA). This commercially available software can fit a batch of hundreds of spectra automatically. The user selects the spectra and the ECM to be used and can set minimum and maximum values for each equivalent circuit element. The software uses the indicated ECM and the boundaries to fit each spectrum sequentially, generating a comprehensive table of fit parameters for all spectra. This table can be copied and exported for further data analysis and plotting.

Data management procedures specific to impedance data variables and file formats were developed for data processing within the framework of COMBIgor (available for download from [www.combigor.com](http://www.combigor.com)).<sup>[175]</sup> These procedures include loading and sorting of raw data and ECM fit data, calibrating measured temperature data, and calculating fit data from fit parameters for the purpose of plotting raw and fit data simultaneously. Nyquist or Bode plots can be generated for all contacts in a library at all measurement temperatures, either with or without the ECM fits, and saved in a location selected by the user. COMBIgor functions can also be used to directly compare and plot impedance data against other variables, such as those related to structure or composition.

Additional developments could enhance fit quality and automation capability by supplementing or replacing ECM fitting with a method that utilizes the distribution of relaxation times (DRT).<sup>[176]</sup> The DRT could be analyzed to determine the number and type of circuit elements with which to fit the spectrum and would replace the current approach that applies a single, user-selected model to all points. This enhancement would be especially useful if the number of observed processes changes across a compositional range or with temperature.

## 3.4 Experimental methods

### 3.4.1 Preparation of thin-film sample libraries

The instrument was tested on one- and two-layer thin-film libraries. The first layer is a nominally 2  $\mu\text{m}$  thick film of proton-conducting  $\text{BaZr}_{0.8}\text{Y}_{0.2}\text{O}_3$  (BZY20). A single-layer BZY20 film was chosen for demonstrating repeatability and accuracy of the tool because the properties of this film are expected to exhibit minimal spatial variation. For the two-layer samples, the BZY20 layer is topped with a compositionally graded layer of  $\text{Ba}(\text{Co}_{1-x-y-z}\text{Fe}_x\text{Zr}_y\text{Y}_z)\text{O}_3$  (BCFZY), which is a known triple ionic-electronic conducting cathode material for proton-conducting fuel cells.[20] Data from the two-layer BZY20/BCFZY stack demonstrates the automated spatial mapping features of the instrument. Combined, these two layers were tested as a half fuel cell, in which the comparatively low electronic conductivity of the BZY20 layer ensures that the various reaction and diffusion processes taking place in the BCFZY cathode layer are not masked by a DC electronic short.

As shown in Figure 3.1b these one-layer and two-layer stacks are deposited on commercially available, ITO-coated glass substrates (150 to 200 nm ITO thickness, Delta Technologies, USA), which act as the counter electrodes. The BZY20 electrolyte was blanket-coated on ITO. For half-cell samples, the BCFZY cathode film was deposited through a shadow mask, creating a patterned array of circular electrodes with 1.75 mm diameter. Shadow masking is a viable method here because the entire area of this TIEC material is electrochemically active and, thus, a perfectly well-defined electrode edge is not critical. Finally, circular metal contacts of 1 mm diameter were applied to the thin-film samples to reduce interfacial impedance between the sample and the probe tip, leaving the outer edge ( $1.62 \times 10^{-2} \text{ cm}^2$ ) of the BCFZY film exposed to the gas atmosphere. A 10 nm Ti adhesion layer followed by 50 nm of Au were deposited through a shadow mask by electron-beam metallization (FC-2000, Temescal, USA). Before measurement, the samples were annealed in air for 4 hours at 500°C to equilibrate the oxygen stoichiometry. This approach to materials synthesis and electrode formation supersedes additional patterning and etching steps that are often reported in literature for similar measurements.[163–168]

The BZY20 and BCFZY films were deposited in a combinatorial PLD chamber. This technique uses a 248 nm KrF laser to ablate ceramic targets, creating a plume of the target composition that deposits onto the substrate. The laser energy was set to 300 mJ with a pulse rate of 20 Hz. The base pressure was below  $0.001 \times 10^{-3}$  Torr and total deposition pressures were moderated by continuous oxygen flow.

For the BZY20 sample, the substrate was continuously rotated during deposition to achieve nominally uniform composition and thickness. The substrate heater was set to 800°C and the total pressure was  $50 \times 10^{-3}$  Torr. As many as six targets can be loaded onto a rotating carousel (Appendix A, Figure A.1)

that brings the targets into the path of the laser. Rotation of the substrate to different angles during ablation of different targets achieves x-y composition gradients across the surface of the substrate. This technique was employed for the BCFZY cathode film so that each circular electrode has a unique composition (Figure 3.4a). For this sample, the heater was set to 700°C and the total pressure was  $1 \times 10^{-3}$  Torr.

### 3.4.2 Characterization of thin-film structure and composition

Composition, thickness and structure were characterized by x-ray fluorescence (XRF) and x-ray diffraction (XRD). The number of layers in the film stacks described above, combined with the similarity in composition between the electrolyte and electrode layers and overlapping diffraction peaks observed among all layers make composition and structural mapping of the electrode films by each method quite difficult. To address this challenge, reference samples for structural and chemical characterization of these films were deposited on fused quartz (GM Quartz, USA) using identical synthesis parameters.

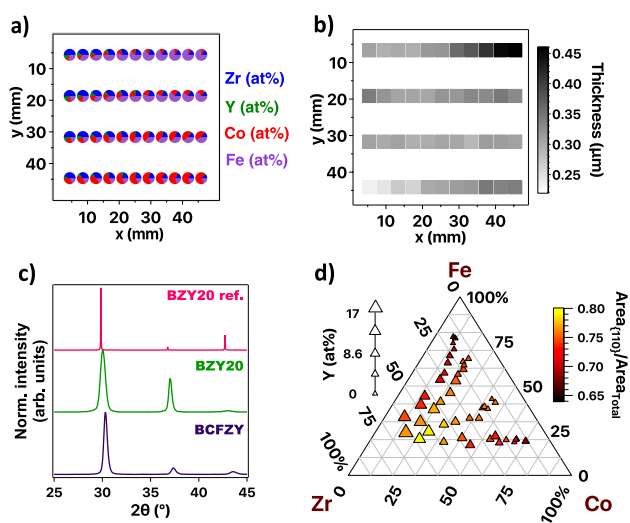


Figure 3.4 Representative composition and structure data. a) Percent occupation of each B-site species shown for 44 points on the combinatorial thin film library. Each pie chart represents the distribution of B-site species at that location. b) Thickness map of the BCFZY film. c) XRD patterns from a BZY20 reference (ICSD no. 187802) compared to representative BZY20 and BCFZY samples from this study. d) Fractional area of 110 peak compared to total area of all peaks in the measured angular range ( $19^\circ \leq 2\theta \leq 52^\circ$ ) across the composition space of the BCFZY library. Fractional area is highest for compositions with high concentrations of the larger ions (Zr and Y) and lowest for compositions with high concentrations of a single, smaller transition metal (Fe or Co).

Composition and thickness were measured by XRF (XDV-SDD, Fischer Technology Inc., USA). XRF composition data for the BCFZY film is shown in Figure 3.4a. The thickness of this film ranged between

235-494 nm (Figure 3.4b).

Materials structure was examined by XRD (D8 Discover, Bruker). All sample points measured on each library showed a single-phase perovskite structure within the resolution of the laboratory XRD (Figure 3.4c). The fractional intensity of the highest intensity diffraction peak (the 110 peak) for all points of the BCFZY film is shown in Figure 3.4d. In each of these instruments, a grid of 44 distinct points was measured, rather than the higher resolution 144-point grid that is mapped on the impedance instrument. The 44-point data was interpolated using a second-degree, two-dimensional polynomial plane fit to provide unique composition data for each of the 144 electrodes on the thin-film library.

### 3.4.3 Electrical measurements and equivalent circuit model fitting

As mentioned above, the BCFZY electrode films under study demonstrate p-type electronic conduction alongside proton and oxygen ion conduction and have high catalytic activity for the oxygen reduction reaction[6] Equivalent circuit models for such triple-conducting cathode materials typically include a series circuit consisting of a resistor and either two or more parallel-connected sets of a resistor (R) and a constant phase element (CPE).[16, 177–181] The equivalent circuit model used here is shown in Figure 3.5a. The parallel R and CPE at high frequency represent the BZY20 bulk. Thus, the ionic resistance ( $R_{\text{ion}}$ ) is represented by  $R_1$  (Figure 3.5b). The lower frequency elements represent the electrode reactions, including oxygen reduction, ion incorporation, and transport within the bulk of each layer and at the interfaces between them.[54, 182] The low frequency impedance of the BZY20 sample (Figure 3.5d) is dominated by the BZY20 surface and the metal-oxide interface, rather than by the BZY20-ITO interface. This is confirmed by the decreased low-frequency impedance in the half-cell samples (Figure 3.5e-g) compared to the BZY20 samples, since both of these contain similar BZY20-ITO interfaces. The Ti is a blocking electrode to the high proton conduction of the BZY20, while the addition of the BCFZY layer provides reversible proton transfer at the BZY/BCFZY interface, reversible electronic conductivity at the interface with the metal contact, and higher ORR activity at the film surface, decreasing the impedance of each of these processes.

In the BZY20 samples, the lowest frequency feature of the spectrum has a very large impedance, due to the blocking nature of the metal electrodes, and only a portion of this feature was captured by the measured frequency range. Consequently, the resistance variable calculated for purposes of reliability studies ( $R_{\text{elyte}}$ ) is the sum of  $R_2$  and  $R_3$ , which includes the semicircle represented in Figure 3.5c, while the low frequency, high impedance tail (Figure 3.5d) was excluded.

For the half-cell library, the polarization resistance ( $R_p$ ) is the primary variable of interest because it provides a measure of electrocatalytic activity: a lower  $R_p$  value corresponds to higher activity.  $R_p$  is

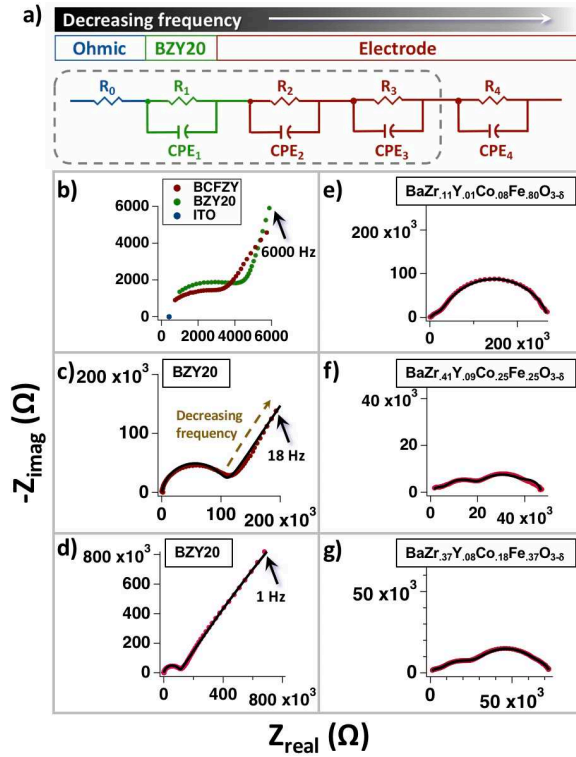


Figure 3.5 Impedance spectra fit by a) an equivalent circuit model that includes parallel combinations of resistors and constant phase elements connected in series. The elements in the dashed rectangle comprise the model for the BZY20 film. b) The high-frequency portion of the Nyquist plots from an ITO substrate, the BZY20 film, and the half-cell stack (BCFZY) show that the BZY20 contribution is visible in the half cell and that ITO is responsible for the ohmic offset ( $R_0$ ). c) The fit of the mid-range frequency semicircle was included in the determination of repeatability, but d) the low frequency feature was excluded because it is not fully captured within the measured frequency range. e-g) Spectra from the compositionally graded libraries were fit using additional circuit elements ( $R_4$  and  $CPE_4$ ), to account for impedance contributions related to the addition of the BCFZY layer.

calculated as the sum of all resistances except for the ohmic resistance,  $R_0$ .

### 3.5 Demonstrating instrument capability

#### 3.5.1 Measurement repeatability and accuracy

In order to ensure that data collected by this instrument is reliable, we established that the data is reproducible and that it can be reasonably compared to data from the literature. For these experiments, the BZY20 thin film sample was used.

First, the effects of probe alignment were investigated. It was determined that slight variation in x- or y- coordinates or in z-height has a negligible effect on the results for contacts of this size (Appendix A, Figure A.6). Other factors that may affect measurement repeatability at a particular contact include measurement order, heater block temperature uniformity, thermal contact between sample and heater

block, location of contact with respect to the counter electrode lead, and electrical contact between the sample and the clamp and probe. These were investigated by comparing initial spectra to data collected 1) after a complete measurement cycle and 2) after rotating and reloading the sample.

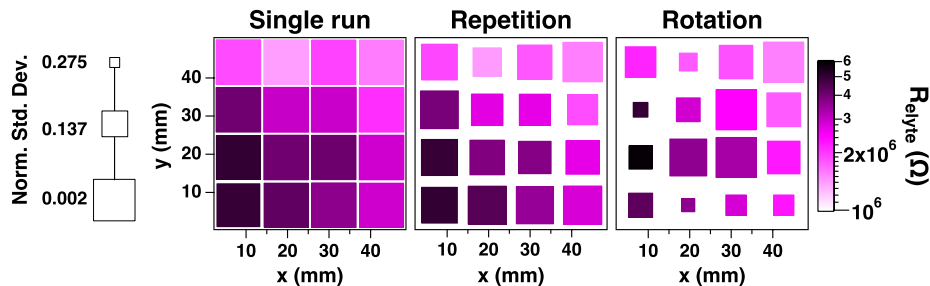


Figure 3.6 Spatial maps of  $R_{\text{elyte}}$  among various sets of measurements of the BZY20 thin film. The sets correspond to data collected (from left to right) within a single run, upon immediate repetition, and upon  $180^\circ$  rotation. Color is determined by average resistance. Marker size is inversely related to standard deviation divided by the resistance value. Higher standard deviation is represented by a smaller marker size, with the value ranging from 0.02% (largest marker) to 27.5% (smallest marker) of the resistance value.

The BZY20 library was measured under 1,400 sccm dry air across a frequency range from 1 MHz to 0.1 Hz. A grid of 16 contacts was probed; each contact was measured five times in immediate succession at heater setpoints of  $400^\circ\text{C}$ ,  $450^\circ\text{C}$ , and  $500^\circ\text{C}$ . After cooling to room temperature, the measurement was repeated again at  $500^\circ\text{C}$ . The library was then rotated  $180^\circ$  and mapped once more to investigate effects of the spatial location of a contact with respect to the heater block and distance from the back-contact lead. Comparison of  $R_{\text{elyte}}$  results for each contact among these rounds of measurements comparing factors of immediate repetition and  $180^\circ$  rotation are shown in Figure 3.6. Average resistance values ranged between  $1.4 \times 10^6$  to  $5.8 \times 10^6$  Ohms. The repeated measurements were in reasonable agreement with each other. Mean standard deviations for a single run, immediate repetition, and  $180^\circ$  rotation were  $8.74 \times 10^5$ ,  $2.63 \times 10^5$ , and  $4.78 \times 10^5$  Ohms, respectively, corresponding to  $\pm 0.69$ , 9.01, and 14.8% of the average resistance for each data set.

The calculated values of  $R_{\text{elyte}}$  are dependent not only on variation in raw spectra, but also on the goodness of fit of the equivalent circuit model and excludes a portion of the impedance spectrum. Consequently, statistical analysis was also performed on pairs of raw spectra taken from the same BZY20 point at the same temperature using a Kolmogorov-Smirnov (KS) two-sample test. This is a non-parametric test that determines the probability (p) that two distributions are from the same population. Results indicated that the differences between the spectra were not statistically significant. Results of this test are consistent with the error analysis of the fitted  $R_{\text{elyte}}$  data. Agreement among spectra from repeated measurements on the library without removal from the instrument is quite high

(average  $p = 0.86$ ), while agreement is lower upon  $180^\circ$  sample rotation (average  $p = 0.54$ ). However, in all cases, spectra from the same contact at different locations on the stage are more consistent than spectra taken from different contacts on the same physical location on the stage. Thus, the results of both the  $R_{\text{elyte}}$  comparison and the KS analysis verify the repeatable nature of these measurements and suggest that the variation in measured impedance is dominated by variations in the material and not by the measurement instrument. This instills confidence in observed trends among contacts measured on a single library and from different libraries.

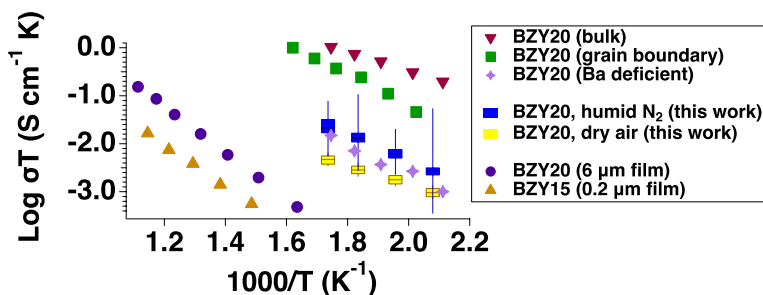


Figure 3.7 Conductivity comparison between the BZY20 film measured in this study to materials with similar chemical compositions from the literature. Conductivity from the present work is higher than other thin films, likely due to use of the through-plane measurement configuration. Film conductivity is lower than values from bulk samples, except for values from Ba-deficient materials, which demonstrated lower conductivity than stoichiometric compositions.

Not only is data from the instrument repeatable, but the extracted ionic conductivity is also consistent with literature values[67, 172, 183] for materials of similar composition. Figure 3.7 shows data from the present work compared to data from thin films of BZY20 and BZY15 measured in-plane under humidified nitrogen ( $p_{\text{H}_2\text{O}}=0.03$  atm) and humidified argon (100%RH at  $25^\circ\text{C}$ ,  $p_{\text{H}_2\text{O}}\approx 0.03$  atm), respectively. The considerably thicker BZY20 film ( $6\ \mu\text{m}$ ) displays higher conductivity than the thinner BZY15 film. This effect is likely attributable to differences in microstructure and in grain boundary density since grain boundary conductivity is lower than that of the grain interior.[67, 172] The conductivity of each of the thin films is lower than the highest values reported for bulk materials.[172] However, the conductivity of our films is quite similar to that of Ba-deficient bulk material. Thus, the lower conductivity of our films compared to the highest performing bulk materials may be due to a combination of barium deficiency and microstructural differences, while the through-film measurement configuration utilized by our instrument results in higher measured conductivity compared to thin films from the literature that were measured using an in-plane configuration. Overall, data from the present work falls reasonably within the range defined by previously reported data.

### 3.5.2 Gas-dependent results

Measurements of the BZY20 samples under lab ambient and under flowing gas showed that controlling the gas atmosphere during measurement improves repeatability. Measurements under dry air flow achieved much more consistent results than those without gas flow (Appendix A, Figure A.2). Since more than 24 hours passed between repeated measurements, changes in the ambient environment could have led to changes in the local gas atmosphere over time, while continuous gas flow ensures a consistent and stable local gas environment across all measurements.

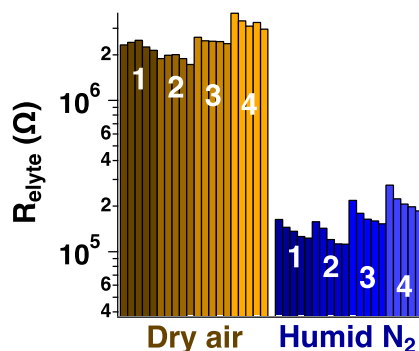


Figure 3.8 Resistance of BZY20 samples measured under dry and humid gases. Each set of same-color bars represents repeated measurements on an individual contact (labeled 1-4), ordered chronologically from left to right. The sample was subjected to a 20-second dwell under dry air or a 100-second dwell under humidified nitrogen before each measurement.

These results show that directing gas flow toward the BZY20 sample in the immediate location of the probe enables gas-dependent property investigations. This is confirmed by a large change in  $R_{\text{elyte}}$  observed under humidified nitrogen compared to dry air. However, the 20-second dwell time used for measurements under dry air proved insufficient for local equilibration under humidified nitrogen. In fact, the impedance of the BZY20 sample did not reach equilibrium under humidified nitrogen even after five measurements taken with 100s dwells in between (Figure 3.8);  $R_{\text{elyte}}$  decreased with each repeated measurement on the same contact. While this is an important result for the study of this material, equilibration time will vary based on the kinetics of the thin film material and must be established for each individual case. In the future, the LabVIEW program and the probe could be upgraded to monitor either the relative humidity or the impedance as a function of time, and to initiate the automated measurement when the chosen variable has stabilized within a given tolerance.

### 3.5.3 Mapping property variation on a compositionally graded library

To map property variation on the two-layer BZY20/BCFZY library, a grid of 144 contacts was measured at heater setpoints between 400°C and 500°C (corresponding to sample surface temperatures ranging from 238–303°C) under 1,400 sccm dry air across a frequency range from 1 MHz to 0.1 Hz. As discussed previously, the  $R_p$  for the half cell samples is calculated as the sum of all non-ohmic resistances from the equivalent circuit model for each point on the sample library.  $R_p$  ranges across more than an order of magnitude as a function of composition and varies by more than two orders of magnitude as a function of both composition and temperature (Figure 3.9). The observed temperature-activated decrease in  $R_p$  is expected since both ionic conductivity and electrocatalytic activity increase with temperature. These results demonstrate that electronic properties can be successfully mapped across graded samples.

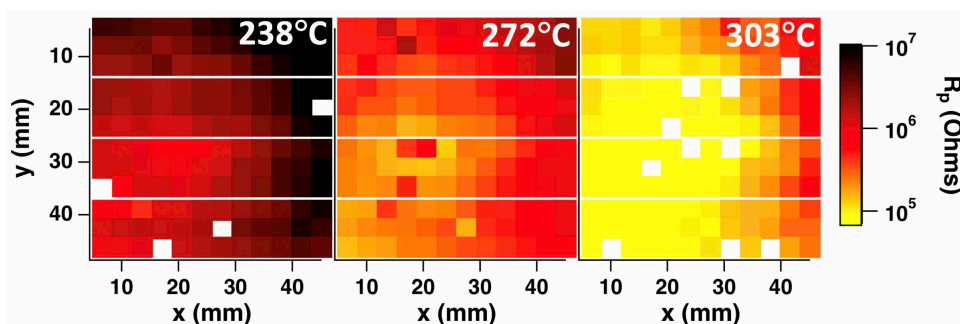


Figure 3.9 Temperature-dependent polarization resistance ( $R_p$ ) results from a compositionally graded BCFZY thin film measured under dry air showing decreasing  $R_p$  with increasing temperature. Outliers, shown in white and defined by deviation in  $R_p$  of more than an order of magnitude from an immediately adjacent contact, have been removed for clarity.

### 3.5.4 Experimental throughput

The BCFZY sample represented in Figure 3.10 (including both the electrolyte and patterned cathode layers) was synthesized in a single day, with another half day required for metallization and annealing. Electrical mapping of this 144-point library takes 10 to 20 hours at each temperature. This time frame can be extended or reduced depending on the number of contacts measured, the frequency range selected, and the equilibration times used. The single thin-film library represented in Figure 3.10 captured B-site cation compositional variations ranging between 8–74 at% Co, 16–81 at% Fe, 12–57 at% Zr, and 0–17 at% Y. The trend in materials properties with composition is consistent with the understanding from the literature.[184] However, a full analysis of composition-property relationships would require additional characterization of the materials and interfaces. Such effects will be addressed in a future publication.

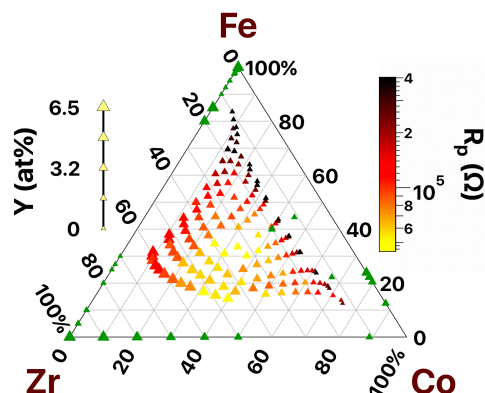


Figure 3.10 Polarization resistance measured at 303°C under 1,400 sccm dry air across the compositional spread of a  $\text{Ba}(\text{Zr},\text{Y},\text{Co},\text{Fe})\text{O}_3$  thin film. Position on the ternary is determined by percent occupancy of the majority B-site cations. Marker size represents yttrium concentration. Green markers represent bulk compositions from the ten studies found in literature.

In contrast, the time to synthesize a single bulk electrode composition by the sol-gel method (a common synthesis method) and to fabricate a half cell takes approximately 5 days. Device characterization can be completed in 0.5 to 1 day. Thus, synthesizing and testing 144 compositions in bulk would take nearly 2 years, while this single library of 144 unique compositions can be synthesized and measured within a few days.

The rapid pace of synthesis and characterization available by combinatorial methods also facilitates investigation at much higher compositional resolution compared to data obtained by serial experimental methods. The difference is obvious in Figure 3.10, where the green markers compare the low coverage of this compositional space in the literature from ten different studies[25, 47, 49, 84, 185–190] to the density of data points collected in the present study. Oftentimes, one composition is found to have preferred properties and much effort is put into optimizing that composition by, for example, microstructural engineering, at the expense of further compositional optimization. Combinatorial characterization tools, such as the present example, both enable compositional optimization in a reasonable time frame and provide a route to collecting a complete data set that can inform a fundamental understanding of composition-property relationships, thereby enabling informed materials discovery avenues.

### 3.6 Summary

An instrument for spatially resolved measurements of temperature-dependent electrochemical impedance under locally controlled gas environments was developed and used to characterize both uniform BZY20 and compositionally graded BCFZY thin film libraries. Ionic conductivity measured on the BZY20 proton conductor is consistent with experimental results from similar thin films in the literature, verifying

the accuracy of this method. The spatially resolved character of the instrument is demonstrated by mapping the temperature-dependent impedance of a compositionally graded BCFZY thin film. In this instrument, the heater can reach a setpoint of 500°C with the demonstrated sample surface temperature reaching 375°C with no gas flow and 300°C under a 1,400 sccm dry air flow. The gas flow is directed locally to each sample point during measurement and, as a result, long dwell times may be required for the sample to reach equilibrium with the gas environment. However, this automated method still provides data in a significantly shorter time frame than traditional, serial experimental methods. In addition, this instrument is readily configurable and employs a simpler design than other state-of-the art measurement instruments with similar capabilities.

CHAPTER 4  
COMBINATORIAL SCREENING OF TRIPLE IONIC-ELECTRONIC CONDUCTING,  
TRANSITION-METAL SUBSTITUTED BARIUM ZIRCONATE ELECTRODES

Meagan C. Papac,<sup>7,8</sup> Andriy Zakutayev,<sup>7,8</sup> and Ryan O’Hayre,<sup>8,9</sup>

#### 4.1 Abstract

Transport properties of triple ionic-electronic conducting oxides (TIECs) depend on chemical composition as well as environmental conditions, such as temperature and gas environment. A family of TIEC perovskites,  $\text{Ba}(\text{Zr}, \text{Y}, \text{Co}, \text{Fe})\text{O}_{3-\delta}$ , was studied by combinatorial methods to observe changes in electronic properties at elevated temperatures in both humidified  $\text{N}_2$  and dry air. Appropriate deposition parameters are established for synthesizing thin film samples by pulsed laser deposition across a wide range in chemical composition. The electrochemical performance of these thin films is evaluated by polarization resistance as determined by electrochemical impedance spectroscopy. We demonstrate that the lowest polarization resistance under dry conditions is achieved in Co-rich compositions. Under humid conditions, low polarization resistance is achieved both in compositions with less than 25% B-site occupancy by Fe and in Y-rich compositions in which the B-site occupancy by multi-valent transition metals is near 40%. These conclusions provide an empirical map of oxygen electrode performance in this family of materials.

#### 4.2 Introduction

Triple ionic-electronic conducting oxides (TIECs) have recently gained interest for their unique ability to simultaneously transport electrons and two ionic species. Within this class of materials,  $\text{Ba}(\text{Co}_{0.4}\text{Fe}_{0.4}\text{Zr}_{0.1}\text{Y}_{0.1})\text{O}_{3-\delta}$  (BCFZY4411) stands out for demonstrating high catalytic activity for the oxygen reduction reaction (ORR), for achieving high performance when employed as a cathode in protonic ceramic fuel cells (PCFCs),<sup>[6]</sup> and for its ability to perform as an anode when a PCFC is operated in reverse as an electrolysis cell.<sup>[23]</sup> Although the properties and performance of BCFZY4411 have been the subject of several studies,<sup>[10, 20, 116, 191, 192]</sup> understanding the properties of similar materials across a broad range in chemical composition will enable tuning and optimization of transport properties in similar materials by altering the cation composition.

Prior studies of two-species mixed ionic-electronic conductors (MIECs) provide a baseline understanding of conduction mechanisms in these triple-conducting materials.<sup>[184]</sup> For example, in

---

<sup>7</sup>Materials, Chemical, and Computational Science directorate, National Renewable Energy Laboratory

<sup>8</sup>Department of Metallurgical and Materials Engineering, Colorado School of Mines

<sup>9</sup>Author for correspondence

materials that contain a sufficient concentration of multi-valent transition metals (TMs), electronic conduction is achieved through a small-polaron hopping mechanism and charge is transferred through the TM-O-TM bond network.[40–42] Protons are transferred among oxygen sites by a Grotthuss-type mechanism,[36] while oxygen ions are transported by a vacancy-diffusion mechanism.[37, 38] Each of these mechanisms can be enhanced or inhibited by manipulating the cation composition.

Most known MIECs are perovskite ( $ABO_3$ ) or perovskite-like structures that readily accommodate A- and/or B-site cation substitution. Substituting a cation to enhance transport of one carrier may inhibit transport of another carrier. For example, substitution with Co can benefit both electronic conductivity and oxygen vacancy formation.[98, 193] Cobalt has a low binding energy with O and can, consequently, facilitate oxygen vacancy formation and diffusion and enhance surface exchange kinetics of oxygen. However, cobalt may inhibit proton uptake due to the higher covalency of Co-O (versus Fe-O) bonds, which decreases the oxygen site basicity.[185] Conversely, Fe substitution on the B-site of  $BaZrO_3$  decreases proton migration energy, enhancing proton transport.[25] In Ba-based oxides with Co or Fe on the B-site, Y stabilizes the cubic structure in concentrations as small as 8 at% B-site occupancy and increases the unit cell volume. Both of these structural factors can increase the electronic and ionic mobility.[47, 84] However, the high binding energy of Y-O, while structurally stabilizing, can reduce oxygen ion mobility. The presence of Y can also lower the oxidation state of Fe, which decreases the electron-hole concentration.[47] Lastly, since electronic conductivity in transition-metal doped oxides occurs via small polaron hopping, B-site yttrium disturbs the path of electron holes, which follow the B-O-B pathway.[45, 46] Due to these various, and often conflicting, effects of each element on transport, a comprehensive studies with high compositional resolution are required to better understand how changes in cation concentrations affect transport properties in the  $Ba(Co,Fe,Zr,Y)O_{3-\delta}$  (BCFZY) materials system. Unfortunately, conducting such studies via serial methods would be prohibitively time consuming. We, instead, apply combinatorial methods to screen this composition space.

Combinatorial methods have previously been applied to measurement of thin-film electrode and electrolyte materials.[163–167] Patterned microelectrodes are synthesized atop an electrolyte layer that has been deposited on a conductive counter electrode.[163] We use a similar configuration here. We perform a study of electronic properties as a function of B-site cation concentrations in these complex oxides. We show that substituting Co on the B-site enhances necessary reactions and transport while significant substitution with Fe has little benefit and can even be detrimental to the performance of these materials. In dry conditions, Co reduces polarization resistance due to charge transfer. In humid conditions, Co reduces polarization resistance by promoting oxygen vacancy formation. In the presence of a significant Co concentration, substitution with Y also decreases polarization resistance. This effect is attributed to the

larger unit cell, more symmetric structure, and higher oxygen site basicity enabled by this cation.

### 4.3 Methods

For this study, we employ combinatorial experimental methods to examine a broad compositional range. First, we establish parameters for synthesizing BCFZY thin films across the required range. Next, we explore the electronic properties of the BCFZY materials system to uncover composition-property relationships.

### 4.4 Thin film synthesis

We synthesized thin films ranging in thickness from 450 to 600 nm by combinatorial pulsed laser deposition (combi-PLD). Substrates are pre-heated in the vacuum chamber for 30 minutes by a radiative heater. The combi-PLD system has a rotational carousel on which as many as six targets can be loaded simultaneously. These targets are sequentially brought into the path of a 248-nm KrF excimer laser (Figure 4.1(a)) and are ablated at a distance of 7.5 cm from the substrate. The system is equipped with a rotational substrate holder that centers specific locations of the substrate over the targets during ablation. By depositing different target compositions at different substrate locations, compositional gradients spanning a range of 6 to 60 at% B-site occupation for any single element are achieved across a 2" × 2" substrate Figure 4.1(b). These compositionally graded samples are known as libraries. The entire BCFZY composition range examined in this study is represented in Figure 4.1(c). Further information regarding target synthesis can be found in Appendix B, Section B.1.

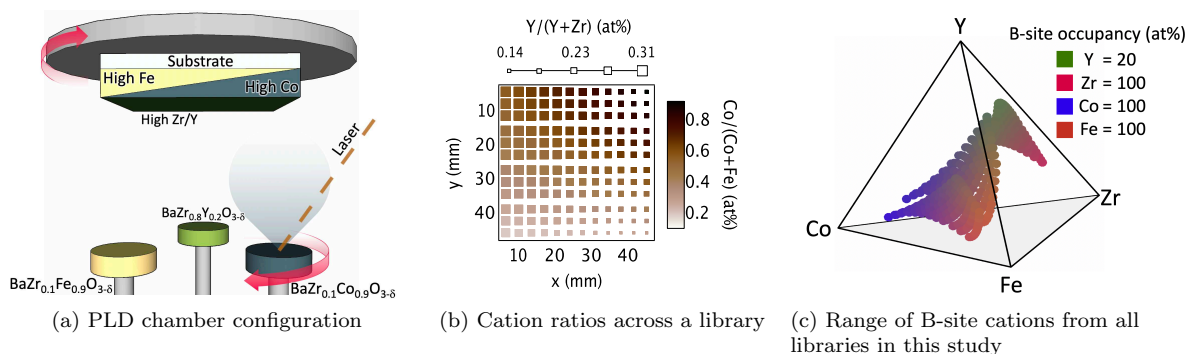


Figure 4.1 Pulsed laser deposition for synthesis of combinatorial libraries. a) The laser ablates a target, creating a plume that is deposited on the inverted substrate. Rotation of the target carousel and of the substrate throughout a deposition results in composition gradients in the film. b) Cation ratios can be spatially mapped across a library. Ratios are extrapolated from 44-point XRF maps to all 144 points characterized by DC and AC electrical measurements. c) 3D representation of entire composition space covered in this study. The basal plane cation apexes represent full occupation of the B-site by that species. The yttrium axis has been elongated for clarity such that the apex represents 20% B-site occupancy.

Pulsed laser deposition gives access to a wide range in synthesis parameters such as substrate temperature, gas partial pressure, laser energy, and laser pulse frequency. These parameters were explored in order to establish which combination most consistently produced crystalline films across a broad compositional range. To determine the effects of substrate temperature, the substrate was loaded onto a purpose-built substrate holder that applied a temperature gradient across the substrate during deposition. Pressure effects were investigated by depositing films at 1, 5, 10, 50, and 100 mT. Laser pulse frequencies between 5 and 40 Hz were tested as well as 200 mJ and 300mJ laser energies. The results of these experiments are discussed in Section 4.7.1.

Compositionally graded BCFZY thin films were deposited as part of three distinct film stacks, each for a different method of characterization Table 4.1. Sample type 1 comprises continuous film libraries deposited directly on bare, fused silica substrates ( $\text{SiO}_2$ ). These libraries served as reference samples for structure and chemical composition measurements and avoided the elemental and diffraction peak overlap that arises with additional layers. Sample type 2 comprises continuous film libraries deposited on ITO-coated glass substrates (ITO, Delta Technologies, USA). Current-voltage curves were collected from these libraries. Sample type 3 comprised two PLD-deposited layers atop an ITO-coated glass substrate, to form a library of electrochemical half cells. A compositionally uniform, continuous  $\text{BaZr}_{0.8}\text{Y}_{0.2}\text{O}_{3-\delta}$  (BZY20) layer serves as the electrolyte and is topped with a compositionally graded BCFZY electrode library. In these samples, the BCFZY layer was deposited through a shadow mask to produce a 12x12 point array of spatially separated and compositionally unique 1.75 mm diameter microelectrodes. These samples were characterized by electrochemical impedance spectroscopy. The proton-conducting and electron-blocking BZY20 layer was included to ensure that the ionic conductivity of the BCFZY layer was not obscured by the electronic conductivity, which may be much greater than the ionic conductivity. To improve electrical contact between the sample and the probe during electrical measurements, sample types 2 and 3 were topped with 12x12 point arrays of metal contacts. These 1 mm diameter circular contacts employed a 50 nm adhesion layer of Ti topped with a 100 nm layer of Au and were deposited through a shadow mask in a Temescal FC-2000 Electron Beam Evaporation System.

Table 4.1 Unique sample types for each characterization method.

Type	Substrate	Electrolyte	Cathode	Electrical contacts	Characterization method/s
1	$\text{SiO}_2$	None	BCFZY	None	XRD, XRF
2	ITO	None	BCFZY	50 nm Ti +100 nm Au	DC conductivity
3	ITO	BZY	BCFZY	50 nm Ti +100 nm Au	Impedance spectroscopy

## 4.5 Thin film characterization

### 4.5.1 Structure and composition

Thin film structure and composition were analyzed on a 4x11 point grid via x-ray diffraction (XRD) and x-ray fluorescence (XRF), respectively. X-ray diffraction patterns were collected by a 2D detector in a Bragg-Brentano configuration in a Bruker D8 Discover diffractometer with Cu K $\alpha$  radiation. The diffraction angle ranged from 19° to 52° with a step size of 0.05°. Peaks were indexed according to cubic barium zirconate. Cubic lattice constants were calculated by the position of the most intense diffraction peak, the (110) peak. Energy dispersive x-ray fluorescence was measured by a Fischerscope<sup>®</sup> X-Ray XDV<sup>®</sup>-SDD to determine film thickness and composition. A spectrum collected from a blank, fused quartz substrate provided a base spectrum for this analysis. Data from XRD, XRF, and other characterization methods were processed by custom routines within the COMBIgor software package.[175]

### 4.6 Electrical characterization

Electrical characterization was performed by a lab-built instrument that is described in detail elsewhere.[194] Measurements were taken at elevated temperatures by placing the sample on a hot stage and employing automated data collection routines to measure the libraries in a through-film configuration. A custom-built probe directed localized gas flow toward the sample during measurement. After each temperature ramp, the sample was equilibrated for 4 mins to achieve a consistent surface temperature. An additional dwell was employed after the probe moved to each contact in order to equilibrate the local gas environment. The samples were measured under dry air, after a 20-second dwell per contact, and under humidified N<sub>2</sub> ( $p_{H_2O} = 0.028$  atm), after a 100-second dwell per contact.

Direct-current (DC) current-voltage curves were collected from the type 2 sample libraries by a Keithley DC voltmeter for voltages between -1 and 1 V in increments of 0.01 V. Resistance was calculated from linear fits of these curves between 0 and 0.5 V. Conductivity was calculated by combining these resistances with the film thicknesses from each point, as determined by XRF, and the assumption that all metal contacts have equal, negligible resistance. A full voltage sweep was recorded at hot-stage set points ranging from 200°C to 500°C in increments of 100°C under both dry air and humidified N<sub>2</sub>.

Electrochemical impedance was measured on the half-cell samples (sample type 3) by an Interface 1000 potentiostat (Gamry, USA) that was run in potentiostatic mode. Impedance spectra were collected at hot-stage set points from 350°C to 500°C in 50°C intervals under both dry air and humidified N<sub>2</sub>. For screening purposes, polarization resistance was approximated as the low-frequency intercept of the modulus of the impedance as determined by a linear fit of five data points at the low-frequency end of the spectrum.

## 4.7 Results and discussion

### 4.7.1 PLD deposition parameters

Deposition parameters were evaluated by the crystallinity of the resulting films and by the time required to produce films of the desired thickness. A film with the smallest FWHM of the most intense diffraction peak, the (110) peak, was considered to be the most crystalline. First, films of various compositions were synthesized at 50 mT at various substrate temperatures. It was found that film crystallinity decreased at lower temperatures (Figure 4.2(a)). Thus, 700°C was chosen as the heater setpoint temperature for the BCFZY films. In these films, samples with highest Fe concentrations consistently demonstrated the lowest crystallinity. Consequently, films deposited from a single  $\text{BaZr}_{0.1}\text{Fe}_{0.9}\text{O}_{3-\delta}$  target were chosen to analyze the effects of deposition pressures between 1 and 100 mT. Of the pressures studied, 1 mT produced the most crystalline films (Figure 4.2(b)). This pressure was, therefore, subsequently used to synthesize single-target films of the other end-member composition targets (which represent the end members of the accessible composition space) as well as a single film containing more equal concentrations of all B-site dopants. XRD analysis of these films confirmed that the 1 mT deposition pressure produced crystalline films across the entire composition space of interest. Next, laser parameters were investigated. While 5 Hz and 40 Hz produced less crystalline films, both 10 Hz and 20 Hz produced more crystalline films (Figure 4.2(c)). Likewise, both 200 mJ and 300 mJ laser energies produced films with similar FWHM. Laser energy of 300 mJ and pulse frequency of 20 Hz were chosen due to their ability to produce crystalline films at higher rates than the other values studied for these parameters. Although higher deposition rates can result in rough film surfaces and low quality interfaces, this did not become a concern under these conditions.

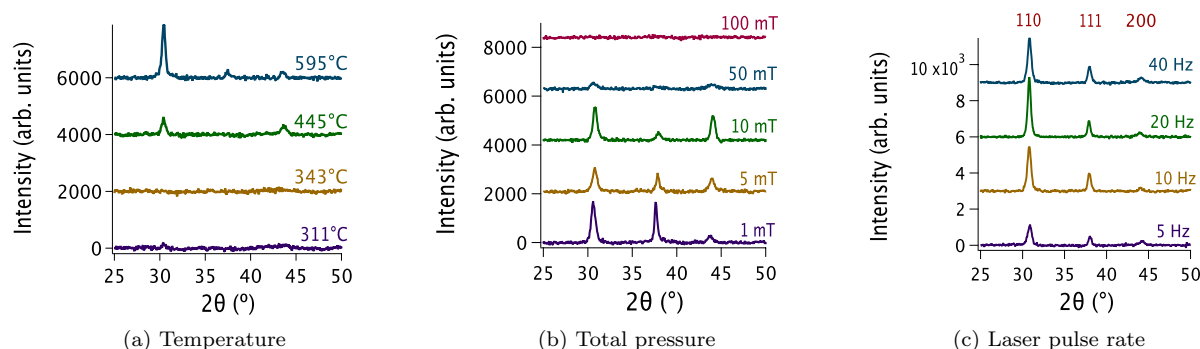


Figure 4.2 Effect of deposition variables on thin film XRD patterns. a) Laser pulse frequency has a negligible effect. Peak intensity increases with b) increasing temperature and c) decreasing total pressure. Peaks in part c) are referenced according to cubic perovskite lattice planes.

### 4.7.2 Structure and composition

Crystalline films were synthesized across the entire composition range under study (see Appendix B, Figure B.1). Each film displayed a cubic perovskite structure; no secondary phases were observed in as-deposited films within the resolution of the laboratory-scale diffractometer. The position of the XRD peaks shifted to higher  $2\theta$  with decreasing B-site ionic radius (Figure 4.3). This trend indicates that substitution of smaller cations (Fe and Co) for larger cations (Zr and Y) on the B-site has a measurable effect on the lattice parameter. Combined with the single-phase XRD patterns, the synchronous change of the lattice constant with the average B-site cation radius indicates that the cations form a solid solution. Chemical composition across each library varied as expected based on the compositions of the targets that were ablated during deposition of each library. SEM images show a consistent, columnar microstructure in the BZY electrolyte layer (Figure 4.3(c)). These images show neither obvious variation in surface roughness nor delamination after electrical measurements.

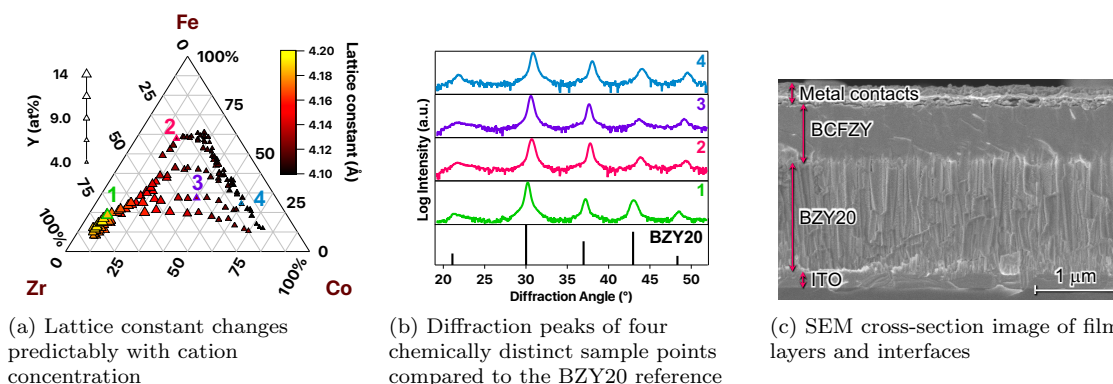


Figure 4.3 Results of structural and microstructural analysis. a) Selected diffraction patterns that correspond to 4 points marked on the ternary plot in part b. The bottom pattern shows the peak positions of BZY20. BCFZY films exhibit the same peaks as the cubic perovskite structure of BZY20, with peak shifts occurring alongside changes in B-site cation ratios. b) Cubic lattice constant across the composition range covered by the three libraries. Lattice constant increases with increasing average B-site cation size. c) SEM micrographs show the columnar microstructure of BZY20, and the interfaces between each layer after impedance measurements.

### 4.7.3 DC results

DC conductivity increased with the concentration of multi-valent transition metals (TM) up to 80 at% B-site occupancy (Figure 4.4(a)). At concentrations of these cations that exceeded 80 at%, conductivity decreased. Conductivity also increased at high concentrations of Zr and Y. DC conductivity increased with increasing temperature, which is consistent with a small polaron hopping mechanism.

While the electronic conductivity is expected to increase with increasing TM concentrations, conduction by small polaron hopping requires a percolative conduction pathway. As the TM concentration increases far beyond the Zr concentration, the majority of TM sites, Fe in particular, may assume a higher oxidation state for charge balance. Since this mechanism relies on both 3+ and 4+ cations, a high concentration of cations in the 4+ oxidation state may inhibit electronic conductivity beyond an upper limit of TM concentration. High TM concentrations may also induce formation of oxygen vacancies, which disrupt the B-O-B conduction path.

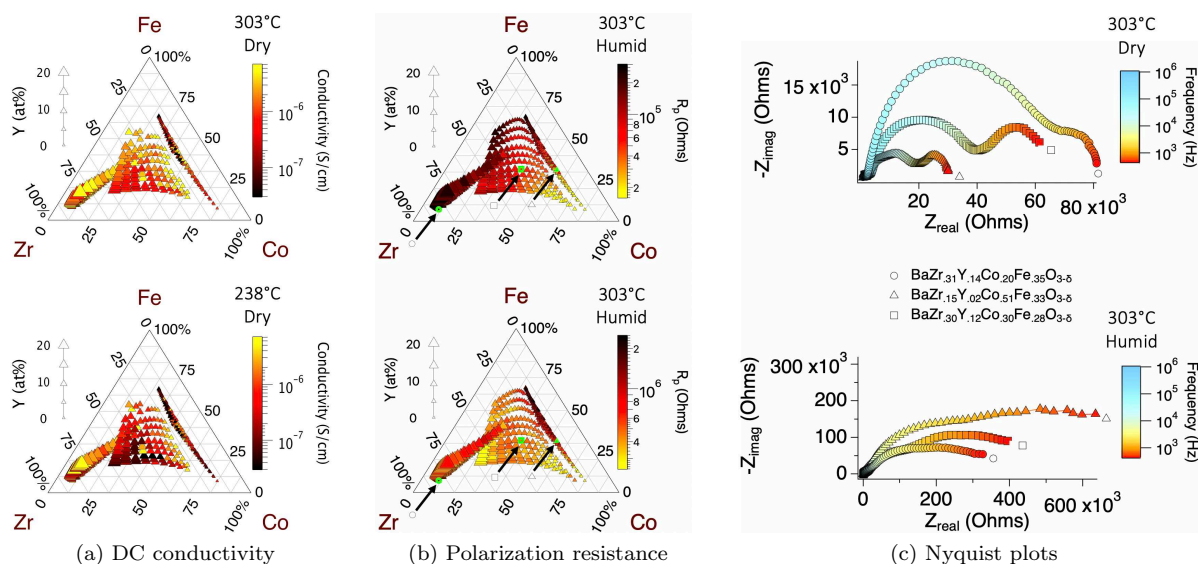


Figure 4.4 Results of DC and AC electronic measurements under dry and humid conditions. a) DC conductivity under dry air at (top) 303°C and (bottom) 238°C demonstrates increased conductivity with increased temperature. This supports the assumption of a small polaron conduction mechanism. b) Polarization resistance of all libraries measured at 303°C. Under dry air (top),  $R_p$  decreases with increasing Co concentration. Under humid  $N_2$ ,  $R_p$  is also low when Zr and Y concentrations are high and the B-site occupancy of Co is near 20 at%. c) Nyquist plots of impedance from three select points measured under (top) dry and (bottom) humid conditions at 303°C. Under dry conditions, the mid-range frequency impedance dominates and decreases with increasing cobalt concentration. Under humid conditions, the low-frequency impedance is very high and decreases with increasing Zr and Y concentrations.

#### 4.7.4 Polarization resistance

Here, polarization resistance is defined as the sum of all non-ohmic resistances from the impedance spectrum. This value can be approximated by the modulus at the low-frequency extreme (as frequency goes to 0 Hz) minus the ohmic resistance. The ohmic resistance is defined as the modulus at the high-frequency extreme, where the imaginary part of the impedance goes to zero. Thus, we can observe the trend in  $R_p$  by fitting the values of the modulus at the lowest measured frequencies and extrapolating to  $\omega=0$  Hz. Ohmic resistance is ignored because it varies negligibly and because the magnitude of the ohmic

resistance is very small compared to  $R_p$ . Under dry conditions,  $R_p$  decreases with increasing Co concentration (Figure 4.4(b)). The medium-frequency resistance (generally associated with charge transfer) is high for the Zr- and Y-rich compositions, and lower with increasing concentrations of Co (Figure 4.4(c)). Cobalt is more readily oxidized and reduced than Fe, enabling facile charge transfer and leading to low  $R_p$  when the concentration of Co is high. Under humid  $N_2$ , the low-frequency resistance is very high (Figure 4.4(c)). In this case,  $R_p$  is lowest for compositions that have either high concentrations of Zr and Y or high concentrations of Co when the B-site occupancy of Fe is less than 25 at%. Low-frequency processes are generally diffusion processes that may be aided by the larger unit cells and higher symmetry of the compositions with higher concentrations of larger cations. Additionally, Co and Fe may inhibit ion diffusion when they cause lattice distortion, which can increase migration energies and create low-energy trapping sites. However, the increased electronegativity of Co over Fe results in lower metal-oxygen bond energy, promoting oxygen vacancy formation which could enable higher proton uptake. This could lead to lower  $R_p$  in Co-rich, versus Fe-rich, compositions in humid conditions.

#### 4.8 Conclusions

Thin films spanning a broad range of chemical compositions were synthesized by pulsed laser deposition. The polarization resistance and DC conductivity of the electrodes were mapped at elevated temperatures under humidified  $N_2$  and dry air. The impedance spectra show that low-frequency processes dominate under humid conditions while medium-frequency processes dominate in dry conditions. Polarization resistance is lower in Co-rich compositions in both conditions, but is also lower in Y-rich compositions in the humid condition, suggesting a proton-controlled impedance contribution at low frequencies. DC conductivity increases with increasing temperature, confirming the assumption of a temperature-activated, small polaron hopping conduction mechanism. Trends with composition show that multi-valent transition metals may enhance conductivity, but that beyond an upper concentration limit, DC conductivity will decrease. This is likely due to an increasing average oxidation state of these cations, which limits conduction pathways.

## CHAPTER 5

### EPILOGUE

#### 5.1 Summary

Triple ionic-electronic conducting oxides form a burgeoning materials class that has potential application for many high-performance electrochemical devices. However, more thorough understanding of the effects of cation substitution in these materials is needed in order to effectively engineer them. Automated electrochemical impedance spectroscopy, combined with combinatorial synthesis methods, allows screening of these materials to identify promising chemical compositions. The work presented here demonstrates a method for rapidly investigating the electronic properties of materials with mixed-species transport. The known TIEC,  $\text{BaCo}_{0.4}\text{Fe}_{0.4}\text{Zr}_{0.1}\text{Y}_{0.1}\text{O}_{3-\delta}$ , has been the subject of many investigations, but our method shows that further optimization may be possible via altered cation substitution, demonstrating the necessity and value of this approach.

#### 5.2 Conclusions

This body of work provides a pathway for designing and investigating novel TIEC materials, particularly for protonic ceramic fuel cell cathodes. The properties of these materials are the result of defect concentrations that are determined by cation occupancy ratios and by the atmosphere in which the materials operate. Defect mobility can be influenced by both composition and structural features, such as symmetry and cation ordering. Thus, the overall conductivity of each carrier type can be manipulated by a combination of composition, structure, and operating conditions. Extending the operable temperature range to even lower temperatures and enabling controlled anion transport will further expand TIEC application. However, chemical stability is often lacking in the highest performing compositions and must be overcome to enable widespread use of these materials.

We have shown that single-phase thin films can be deposited across a broad range of B-site cation compositions in the  $\text{Ba}(\text{Co,Fe,Zr,Y})\text{O}_3$  materials family via pulsed laser deposition, regardless of disparate ionic radii of the cation species. Ionic conductivity of a well-known proton conductor, BZY20, showed that the automated impedance mapping method provides reasonable resistance values and that locally directed gas flow provides more stable measurement than ambient laboratory atmosphere. Measurements of impedance under controlled gas environments indicate decreased overall performance under a humid, reducing environment versus a dry, oxidizing environment. Both uptake of protons and lack of oxygen reactant have a negative effect on the oxygen reduction reaction (ORR) in the humid environment. This

observation supports the conjecture that the ORR limits cathode performance, and explains why compositions containing cobalt, which provides high ORR activity, are often present in high-performing devices. Additionally, the results from this set of chemical compositions indicate that Fe, the second multi-valent transition metal included in this study, does not benefit performance, as evaluated by low polarization resistance ( $R_p$ ). In fact, Fe-rich compositions have higher  $R_p$  than both Y-rich and Co-rich variants. This may be due to lower ORR activity because of fewer oxygen vacancies and a less symmetric structure than the Y-rich compositions and less facile redox behavior of Fe compared to Co. Lastly, impedance spectra show that impedance under humid, reducing conditions is dominated by low-frequency processes, while impedance under dry, oxidizing conditions is dominated by mid-range frequency processes.

### 5.3 Future research directions

Although  $R_p$  provides a useful metric for screening cathode performance, further analysis will develop a more fundamental understanding of transport in these materials. To build on the present work, the following research directions are suggested:

1. Improve impedance data fitting by using distribution of relaxation times to resolve overlapping processes and to quantify changes in these processes with composition, temperature, and gas partial pressures.
2. Investigate stability across the composition space and include this variable as a consideration when identifying optimal chemical compositions.
3. Characterize oxidation states of transition metals and incorporate them into composition-property analysis.
4. Compare devices containing previous and optimized chemical compositions to investigate the ability of this combinatorial method to improve performance at the device level.

### 5.4 Additional research contributions

In addition to the manuscripts included in this dissertation, contributions were made toward publications on a combinatorial data analysis software package,[175] a roadmap for protonic oxide electrodes,[195] a study on defect formation energies in perovskite oxides,[196] and a Bayesian method for distribution of relaxation times analysis.[176]

## REFERENCES

- [1] Ranran Peng, Tianzhi Wu, Wei Liu, Xingqin Liu, and Guangyao Meng. Cathode processes and materials for solid oxide fuel cells with proton conductors as electrolytes. *J. Mater. Chem.*, 20(29-30): 6218–6225, 2010. ISSN 01672738. doi: 10.1039/c0jm00350f.
- [2] Cecilia Solís, Laura Navarrete, Stefan Roitsch, and José M. Serra. Electrochemical properties of composite fuel cell cathodes for  $\text{La}_{5.5}\text{WO}_{12-\delta}$  proton conducting electrolytes. *J. Mater. Chem.*, 22(31):16051, July 2012. ISSN 0959-9428. doi: 10.1039/c2jm32061d.
- [3] Cecilia Solís, Laura Navarrete, Francesco Bozza, Nikolaos Bonanos, and José M Serra. Catalytic surface promotion of composite cathodes in protonic ceramic fuel cells. *ChemElectroChem*, 2(8): 1106–1110, August 2015. ISSN 21960216. doi: 10.1002/celec.201500068.
- [4] Sandrine Ricote, Nikolaos Bonanos, Martin Rørvik, and Camilla Haavik. Microstructure and performance of  $\text{La}_{0.58}\text{Sr}_{0.4}\text{Co}_{0.2}\text{Fe}_{0.8}\text{O}_{3-\delta}$  cathodes deposited on  $\text{BaCe}_{0.2}\text{Zr}_{0.7}\text{Y}_{0.1}\text{O}_{3-\delta}$  by infiltration and spray pyrolysis. *J. Power Sources*, 209:172–179, 2012. doi: 10.1016/j.jpowsour.2012.02.090.
- [5] Xinbo Mao, Tian Yu, and Guilin Ma. Performance of cobalt-free double-perovskite  $\text{NdBaFe}_{2-x}\text{Mn}_x\text{O}_{5+\delta}$  cathode materials for proton-conducting IT-SOFC. *J. Alloys Compd.*, 637: 286–290, 2015. doi: 10.1016/j.jallcom.2015.02.001.
- [6] Chuancheng Duan, Jianhua Tong, Meng Shang, Stefan Nikodemski, Michael Sanders, Sandrine Ricote, Ali Almansoori, and Ryan O’Hayre. Readily processed protonic ceramic fuel cells with high performance at low temperatures. *Science*, 349(6254):1321–1326, September 2015. ISSN 1095-9203. doi: 10.1126/science.aab3987.
- [7] Sang-Yun Jeon, Dae-Kwang Lim, In-Ho Kim, Bhupendra Singh, and Sun-Ju Song. Effectiveness of protonic conduction in  $\text{Ba}_{0.5}\text{Sr}_{0.5}\text{Co}_{0.8}\text{Fe}_{0.2}\text{O}_{3-\delta}$  cathode in intermediate temperature proton-conducting ceramic-electrolyte fuel cell. *J. Electrochem. Soc.*, 161(6):F754–F760, May 2014. ISSN 0013-4651. doi: 10.1149/2.086406jes.
- [8] Daniel Poetzsch, Rotraut Merkle, and Joachim Maier. Proton conductivity in mixed-conducting BSFZ perovskite from thermogravimetric relaxation. *Phys. Chem. Chem. Phys.*, 16(31):16446–16453, July 2014. ISSN 1463-9076. doi: 10.1039/C4CP00459K.
- [9] Chunwen Sun, Rob Hui, and Justin Roller. Cathode materials for solid oxide fuel cells: a review. *J. Solid State Electrochem.*, 14:1125–1144, 2010. doi: 10.1007/s10008-009-0932-0.
- [10] F. S. Baumann, J. Maier, and J. Fleig. The polarization resistance of mixed conducting SOFC cathodes: a comparative study using thin film model electrodes. *Solid State Ionics*, 179(21-26): 1198–1204, September 2008. ISSN 0167-2738. doi: 10.1016/J.SSI.2008.02.059.
- [11] Shanwen Tao and John T. S. Irvine. Discovery and characterization of novel oxide anodes for solid oxide fuel cells. *Chem. Rec.*, 4(2):83–95, January 2004. ISSN 1527-8999. doi: 10.1002/tcr.20003.
- [12] Emiliana Fabbri, Daniele Pergolesi, and Enrico Traversa. Materials challenges toward proton-conducting oxide fuel cells: a critical review. *Chem. Soc. Rev.*, 39(11):4355–69, November 2010. ISSN 1460-4744. doi: 10.1039/b902343g.

- [13] Hyegeon An, Hae-Weon Lee, Byung-Kook Kim, Ji-Won Son, Kyung Joong Yoon, Hyoungchul Kim, Dongwook Shin, Ho-Il Ji, and Jong-Ho Lee. A  $5 \times 5 \text{ cm}^2$  protonic ceramic fuel cell with a power density of  $1.3 \text{ W cm}^{-2}$  at  $600^\circ\text{C}$ . *Nat. Energy*, 3:870–875, August 2018. ISSN 2058-7546. doi: 10.1038/s41560-018-0230-0.
- [14] Wenyuan Li, Bo Guan, Liang Ma, Shanshan Hu, Nan Zhang, and Xingbo Liu. High performing triple-conductive  $\text{Pr}_2\text{NiO}_{4-\delta}$  anode for proton-conducting steam solid oxide electrolysis cell. *J. Mater. Chem. A*, 6(37):18057–18066, September 2018. ISSN 2050-7488. doi: 10.1039/C8TA04018D.
- [15] Yuan Zhang, Ruth Knibbe, Jaka Sunarso, Yijun Zhong, Wei Zhou, Zongping Shao, and Zhonghua Zhu. Recent progress on advanced materials for solid-oxide fuel cells operating below  $500^\circ\text{C}$ . *Adv. Mater.*, 29:1700132, December 2017. ISSN 09359648. doi: 10.1002/adma.201700132.
- [16] Sihyuk Choi, Chris J. Kucharczyk, Yangang Liang, Xiaohang Zhang, Ichiro Takeuchi, Ho-Il Ji, and Sossina M. Haile. Exceptional power density and stability at intermediate temperatures in protonic ceramic fuel cells. *Nat. Energy*, 3:202–210, March 2018. ISSN 2058-7546. doi: 10.1038/s41560-017-0085-9.
- [17] Xinwei Sun, Stian Christopher Simonsen, Truls Norby, and Athanasios Chatzidakis. Composite membranes for high temperature PEM fuel cells and electrolyzers: a critical review. *Membranes*, 9(7):83, July 2019. ISSN 2077-0375. doi: 10.3390/membranes9070083.
- [18] Ryan O’Hayre, Suk-Won Cha, Whitney Colella, and Fritz B. Prinz. *Fuel Cell Fundamentals*. John Wiley & Sons, Inc., Hoboken, NJ, 2 edition, 2009. ISBN 9780470258439.
- [19] Lei Wang, Rotraut Merkle, and Joachim Maier. Surface kinetics and mechanism of oxygen incorporation into  $\text{Ba}_{1-x}\text{Sr}_x\text{Co}_y\text{Fe}_{1-y}\text{O}_{3-\delta}$  SOFC microelectrodes. *J. Electrochem. Soc.*, 157(12):B1802–B1808, 2010. doi: 10.1149/1.3494224.
- [20] Jianhua Tong, Chuancheng Duan, David Hook, Yachao Chen, and Jianhua Tong. Zr and Y co-doped perovskite as a stable, high performance cathode for solid oxide fuel cells operating below  $500^\circ\text{C}$ . *Energy Environ. Sci.*, 176(10):176–182, 2017.
- [21] Chen Xia, Youquan Mi, Baoyuan Wang, Bin Lin, Gang Chen, and Bin Zhu. Shaping triple-conducting semiconductor  $\text{BaCo}_{0.4}\text{Fe}_{0.4}\text{Zr}_{0.1}\text{Y}_{0.1}\text{O}_{3-\delta}$  into an electrolyte for low-temperature solid oxide fuel cells. *Nat. Commun.*, 10(1):1707, December 2019. ISSN 2041-1723. doi: 10.1038/s41467-019-09532-z.
- [22] Xiangnan Li, Jie Zhang, Qi Feng, Chunying Pu, Luozheng Zhang, Manman Hu, Xianyong Zhou, Xiongwei Zhong, Wendi Yi, Jun Tang, Zhiwei Li, Xingzhong Zhao, Hui Li, and Baomin Xu. Redox inactive ion meliorated  $\text{BaCo}_{0.4}\text{Fe}_{0.4}\text{Zr}_{0.1}\text{Y}_{0.1}\text{O}_{3-\delta}$  perovskite oxides as efficient electrocatalysts for the oxygen evolution reaction. *J. Mater. Chem. A*, 6(36):263–314, January 2018. doi: 10.1039/C8TA05599H.
- [23] Chuancheng Duan, Robert Kee, Huayang Zhu, Neal Sullivan, Liangzhu Zhu, Liuzhen Bian, Dylan Jennings, and Ryan O’Hayre. Highly efficient reversible protonic ceramic electrochemical cells for power generation and fuel production. *Nat. Energy*, 4(3):230–240, March 2019. ISSN 2058-7546. doi: 10.1038/s41560-019-0333-2.
- [24] Wesley T. Hong, Marcel Risch, Kelsey A. Stoerzinger, Alexis Grimaud, Jin Suntivich, and Yang Shao-Horn. Toward the rational design of non-precious transition metal oxides for oxygen electrocatalysis. *Energy Environ. Sci.*, 8(5):1404–1427, May 2015. ISSN 1754-5692. doi: 10.1039/C4EE03869J.

- [25] Ana B. Muñoz-García, Mariarosaria Tuccillo, and Michele Pavone. Computational design of cobalt-free mixed proton-electron conductors for solid oxide electrochemical cells. *J. Mater. Chem. A*, 5(23):11825–11833, June 2017. ISSN 2050-7488. doi: 10.1039/C7TA00338B.
- [26] Robert J. Kee, Huayang Zhu, Brett W. Hildenbrand, Einar Vøllestad, Michael D. Sanders, and Ryan P. O’Hayre. Modeling the steady-state and transient response of polarized and non-polarized proton-conducting doped-perovskite membranes. *J. Electrochem. Soc.*, 160(3):290–300, 2013. doi: 10.1149/2.016304jes.
- [27] S. H. Morejudo, R. Zanón, S. Escolástico, I. Yuste-Tirados, H. Malerød-Fjeld, P. K. Vestre, W. G. Coors, A. Martínez, T. Norby, J. M. Serra, and C. Kjøseth. Direct conversion of methane to aromatics in a catalytic co-ionic membrane reactor. *Science*, 353(6299):563–566, August 2016. ISSN 1095-9203. doi: 10.1126/science.aag0274.
- [28] A K Demin, E V Gorbova, M V Glumov, and P E Tsiakaras. Charge transfer in mixed proton, oxygen ion and electron solid oxide conductor. *Ionics*, 11:289–293, 2005.
- [29] Anil V. Virkar. Transport of H<sub>2</sub>, O<sub>2</sub> and H<sub>2</sub>O through single-phase, two-phase and multi-phase mixed proton, oxygen ion, and electron hole conductors. *Solid State Ionics*, 140(3-4):275–283, April 2001. ISSN 0167-2738. doi: 10.1016/S0167-2738(01)00817-7. URL <https://www.sciencedirect.com/science/article/pii/S0167273801008177>.
- [30] Michael D. Sanders and Ryan P. O’Hayre. Coupled transport and uphill permeation of steam and oxygen in a dense ceramic membrane. *J. Memb. Sci.*, 376:96–101, 2011. doi: 10.1016/j.memsci.2011.04.007.
- [31] F. A. Kröger and H. J. Vink. Relations between the concentrations of imperfections in crystalline solids. *Solid State Phys.*, 3:307–435, 1956. doi: 10.1016/S0081-1947(08)60135-6.
- [32] Yukio Cho, Masayuki Ogawa, Itaru Oikawa, Harry L. Tuller, and Hitoshi Takamura. Stabilizing coexisting n-type electronic and oxide ion conductivities in donor-doped Ba-In-based oxides under oxidizing conditions: roles of oxygen disorder and electronic structure. *Chem. Mater.*, 31(8):2713–2722, April 2019. ISSN 0897-4756. doi: 10.1021/acs.chemmater.8b03818.
- [33] Daniel Poetzsch, Rotraut Merkle, and Joachim Maier. Oxygen reduction at dense thin-film microelectrodes on a proton-conducting electrolyte. I. Considerations on reaction mechanism and electronic leakage effects. *J. Electrochem. Soc.*, 162(9):939–950, 2015. doi: 10.1149/2.0951508jes.
- [34] Daniel Poetzsch, Rotraut Merkle, and Joachim Maier. Proton uptake in the H<sup>+</sup>-SOFC cathode material Ba<sub>0.5</sub>Sr<sub>0.5</sub>Fe<sub>0.8</sub>Zn<sub>0.2</sub>O<sub>3-δ</sub> transition from hydration to hydrogenation with increasing oxygen partial pressure. *Faraday Discuss.*, 182:129–143, 2015. doi: 10.1039/c5fd00013k.
- [35] N. A. Tarasova, Ya. V. Filinkova, and I. E. Animitsa. Hydration and forms of oxygen-hydrogen groups in oxyfluorides Ba<sub>2-0.5x</sub>In<sub>2</sub>O<sub>5-x</sub>F<sub>x</sub>. *Russ. J. Phys. Chem. A*, 86(8):1208–1211, 2012. doi: 10.1134/S0036024412080134. URL <https://link.springer.com/content/pdf/10.1134/S0036024412080134.pdf>.
- [36] K. D. Kreuer. Aspects of the formation and mobility of protonic charge carriers and the stability of perovskite-type oxides. *Solid State Ionics*, 125(1-4):285–302, October 1999. ISSN 01672738. doi: 10.1016/S0167-2738(99)00188-5.
- [37] M. Cherry, M.S. Islam, and C. R. A. Catlow. Oxygen ion migration in perovskite-type oxides. *J. Solid State Chem.*, 118(1):125–132, August 1995. ISSN 0022-4596. doi: 10.1006/JSSC.1995.1320.

- [38] Alexander Chroneos, Bilge Yildiz, Albert Tarancón, David Parfitt, and John A. Kilner. Oxygen diffusion in solid oxide fuel cell cathode and electrolyte materials: mechanistic insights from atomistic simulations. *Energy Environ. Sci.*, 4(8):2774, August 2011. ISSN 1754-5692. doi: 10.1039/c0ee00717j.
- [39] Roger A. De Souza. Limits to the rate of oxygen transport in mixed-conducting oxides. *J. Mater. Chem. A*, 5(38):20334–20350, October 2017. ISSN 2050-7488. doi: 10.1039/C7TA04266C.
- [40] O F Schirmer.  $O^-$  bound small polarons in oxide materials. *J. Phys. Condens. Matter*, 18(43):R667–R704, November 2006. ISSN 0953-8984. doi: 10.1088/0953-8984/18/43/R01.
- [41] Alexander J. E. Rettie, William D. Chemelewski, David Emin, and C. Buddie Mullins. Unravelling small-polaron transport in metal oxide photocatalysts. *J. Phys. Chem. Lett.*, 7:27, 2016. doi: 10.1021/acs.jpcclett.5b02143.
- [42] Dragos Neagu and John T. S. Irvine. Enhancing electronic conductivity in strontium titanates through correlated A and B-site doping. *Chem. Mater*, 23:1607–1617, 2011. doi: 10.1021/cm103489r.
- [43] P. M. Raccach and J. B. Goodenough. A localized-electron to collective-electron transition in the system (La,Sr)CoO<sub>3</sub>. *J. Appl. Phys.*, 39:1209–1210, 1968. doi: 10.1063/1.1656227.
- [44] T. He, K. D. Kreuer, Yu. M. Baikov, and J. Maier. Impedance spectroscopic study of thermodynamics and kinetics of a Gd-doped BaCeO<sub>3</sub> single crystal. *Solid State Ionics*, 95:301–308, 1997.
- [45] L. W. Tai, M. M. Nasrallah, H. U. Anderson, D. M. Sparlin, and S. R. Sehlin. Structure and electrical properties of La<sub>1-x</sub>Sr<sub>x</sub>Co<sub>1-y</sub>Fe<sub>y</sub>O<sub>3</sub>. Part 1. The system La<sub>0.8</sub>Sr<sub>0.2</sub>Co<sub>1-y</sub>Fe<sub>y</sub>O<sub>3</sub>. *Solid State Ionics*, 76:259–271, March 1995. ISSN 01672738. doi: 10.1016/0167-2738(94)00244-M.
- [46] R. Raffaele, H. U. Anderson, D. M. Sparlin, and P. E. Parris. Evidence for a crossover from multiple trapping to percolation in the high-temperature electrical conductivity of Mn-doped LaCrO<sub>3</sub>. *Phys. Rev. Lett.*, 65(11):1383–1386, 1990.
- [47] Xiaotong Liu, Hailei Zhao, Jianying Yang, Yuan Li, Ting Chen, Xionggang Lu, Weizhong Ding, and Fushen Li. Lattice characteristics, structure stability and oxygen permeability of BaFe<sub>1-x</sub>Y<sub>x</sub>O<sub>3-δ</sub> ceramic membranes. *J. Memb. Sci.*, 383(1-2):235–240, November 2011. ISSN 03767388. doi: 10.1016/j.memsci.2011.08.059.
- [48] Scott Kirkpatrick. Percolation and conduction. *Rev. Mod. Phys.*, 45(4):574–588, 1973.
- [49] Dongyoung Kim, Shogo Miyoshi, Takashi Tsuchiya, and Shu Yamaguchi. Percolation conductivity in BaZrO<sub>3</sub>–BaFeO<sub>3</sub> solid solutions. *Solid State Ionics*, 262:875–878, 2014. doi: 10.1016/j.ssi.2014.01.007.
- [50] L. I. Duckers. Percolation with nearest neighbour interaction. *Phys. Lett.*, 67A(2):93–94, 1978.
- [51] Z. Sherafat, M. H. Paydar, I. Antunes, N. Nasani, A. D. Brandão, and D. P. Fagg. Modeling of electrical conductivity in the proton conductor Ba<sub>0.85</sub>K<sub>0.15</sub>ZrO<sub>3-δ</sub>. *Electrochim. Acta*, 165:443–449, 2015. doi: 10.1016/j.electacta.2015.03.018.
- [52] Abul K. Azad, Cristian Savaniu, Shanwen Tao, Sophie Duval, Peter Holtappels, Richard M. Ibberson, and John T. S. Irvine. Structural origins of the differing grain conductivity values in BaZr<sub>0.9</sub>Y<sub>0.1</sub>O<sub>2.95</sub> and indication of novel approach to counter defect association. *J. Mater. Chem.*, 18(29):3414, July 2008. ISSN 0959-9428. doi: 10.1039/b806190d.

- [53] Koji Katahira, Yoshirou Kohchi, Tetsuo Shimura, and Hiroyasu Iwahara. Protonic conduction in Zr-substituted BaCeO<sub>3</sub>. *Solid State Ionics*, 138:91–98, 2000. ISSN 01672738. doi: 10.1016/S0167-2738(00)00777-3.
- [54] A. Grimaud, F. Mauvy, J. M. Bassat, S. Fourcade, L. Rocheron, M. Marrony, and J. C. Grenier. Hydration properties and rate determining steps of the oxygen reduction reaction of perovskite-related oxides as H<sup>+</sup>-SOFC cathodes. *J. Electrochem. Soc.*, 159(6):B683–B694, January 2012. ISSN 0013-4651. doi: 10.1149/2.101205jes.
- [55] Emiliana Fabbri, Lei Bi, Daniele Pergolesi, and Enrico Traversa. Towards the next generation of solid oxide fuel cells operating below 600°C with chemically stable proton-conducting electrolytes. *Adv. Mater.*, 24(2):195–208, January 2012. ISSN 09359648. doi: 10.1002/adma.201103102.
- [56] Dengjie Chen, Chi Chen, Zarah Medina Baiyee, Zongping Shao, and Francesco Ciucci. Nonstoichiometric oxides as low-cost and highly-efficient oxygen reduction/evolution catalysts for low-temperature electrochemical devices. *Chem. Rev.*, 115(18):9869–9921, September 2015. ISSN 0009-2665. doi: 10.1021/acs.chemrev.5b00073.
- [57] R. A. De Souza and J. A. Kilner. Oxygen transport in La<sub>1-x</sub>Sr<sub>x</sub>Mn<sub>1-y</sub>Co<sub>y</sub>O<sub>3-δ</sub> perovskites. Part II. Oxygen surface exchange. *Solid State Ionics*, 1999. ISSN 01672738. doi: 10.1016/S0167-2738(99)00228-3.
- [58] J. A. Kilner, R. A. De Souza, and I. C. Fullarton. Surface exchange of oxygen in mixed conducting perovskite oxides. *Solid State Ionics*, 86-88:703–709, 1996. ISSN 01672738. doi: 10.1016/0167-2738(96)00153-1.
- [59] R.A. De Souza. A universal empirical expression for the isotope surface exchange coefficients ( $k^*$ ) of acceptor-doped perovskite and fluorite oxides. *Phys. Chem. Chem. Phys.*, 8:890–897, 2006. doi: 10.1039/b511702j.
- [60] N. Sakai, K. Yamaji, Y. P. Xiong, H. Kishimoto, T. Horita, and H. Yokokawa. Interaction between water and ceria-zirconia-yttria solid solutions. *J. Electroceramics*, 13(1-3):677–682, July 2004. ISSN 1385-3449. doi: 10.1007/s10832-004-5175-y.
- [61] Natsuko Sakai, Katsuhiko Yamaji, Teruhisa Horita, Yue Ping Xiong, Haruo Kishimoto, and Harumi Yokokawa. Effect of water on oxygen transport properties on electrolyte surface in SOFCs. I. Surface reaction mechanism of oxygen isotope exchange on solid oxide electrolytes. *J. Electrochem. Soc.*, 150(6):A689–A694, 2003. doi: 10.1149/1.1568938.
- [62] R.R. Liu, S.H. Kim, S. Taniguchi, T. Oshima, Y. Shiratori, K. Ito, and K. Sasaki. Influence of water vapor on long-term performance and accelerated degradation of solid oxide fuel cell cathodes. *J. Power Sources*, 196(17):7090–7096, September 2011. ISSN 0378-7753. doi: 10.1016/J.JPOWSOUR.2010.08.014.
- [63] S. H. Kim, K. B. Shim, C. S. Kim, J. T. Chou, T. Oshima, Y. Shiratori, K. Ito, and K. Sasaki. Degradation of solid oxide fuel cell cathodes accelerated at a high water vapor concentration. *J. Fuel Cell Sci. Technol.*, 7(2):021011–1, April 2010. ISSN 1550-624X. doi: 10.1115/1.3117608.
- [64] H. Hayashi, H. Inaba, M. Matsuyama, N. G. Lan, M. Dokiya, and H. Tagawa. Structural consideration on the ionic conductivity of perovskite-type oxides. *Solid State Ionics*, 122(1-4):1–15, July 1999. ISSN 01672738. doi: 10.1016/S0167-2738(99)00066-1.
- [65] J. A. Kilner and R. J. Brook. A study of oxygen ion conductivity in doped non-stoichiometric oxides. *Solid State Ionics*, 6(3):237–252, May 1982. ISSN 0167-2738. doi: 10.1016/0167-2738(82)90045-5.

- [66] M. Islam. Computer modelling of defects and transport in perovskite oxides. *Solid State Ionics*, 154-155:75–85, December 2002. ISSN 01672738. doi: 10.1016/S0167-2738(02)00466-6.
- [67] K.D. Kreuer. Proton-conducting oxides. *Annu. Rev. Mater. Res.*, 33(1):333–359, August 2003. ISSN 1531-7331. doi: 10.1146/annurev.matsci.33.022802.091825.
- [68] Truls Norby. Proton conductivity in perovskite oxides. In *Perovskite Oxide Solid Oxide Fuel Cells*, pages 217–241. Springer, Boston, MA, 2009. doi: 10.1007/978-0-387-77708-5\\_11.
- [69] David Parfitt, Alexander Chroneos, Albert Taranc, and John A. Kilner. Oxygen ion diffusion in cation ordered/disordered  $\text{GdBaCo}_2\text{O}_{5+\delta}$ . *J. Mater. Chem.*, 21:2183–2186, 2011. doi: 10.1039/c0jm02924f.
- [70] Ragnar Strandbakke, Vladimir A. Cherepanov, Andrey Yu Zuev, Dmitry S. Tsvetkov, Christos Argirusis, Georgia Sourkouni, Stephan Prünite, and Truls Norby. Gd- and Pr-based double perovskite cobaltites as oxygen electrodes for proton ceramic fuel cells and electrolyser cells. *Solid State Ionics*, 278:120–132, 2015. doi: 10.1016/j.ssi.2015.05.014.
- [71] Reihaneh Zohourian, Rotraut Merkle, and Joachim Maier. Bulk defect chemistry of PCFC cathode materials: Discussion of defect interactions. *ECS Trans.*, 77(10):133–138, May 2017. ISSN 1938-6737. doi: 10.1149/07710.0133ecst.
- [72] K. D. Kreuer, Th. Dippel, Yu. M. Baikovb, and J. Maier. Water solubility, proton and oxygen diffusion in acceptor doped  $\text{BaCeO}_3$ : a single crystal analysis. *Solid State Ionics*, 86-88:613–620, 1996.
- [73] K. D. Kreuer, St. Adams, W. Münch, A. Fuchs, U. Klock, and J. Maier. Proton conducting alkaline earth zirconates and titanates for high drain electrochemical applications. *Solid State Ionics*, 145(1): 295–306, 2001. ISSN 01672738. doi: 10.1016/S0167-2738(01)00953-5.
- [74] Andreas Løken, Christian Kjøseth, and Reidar Haugrud. Electrical conductivity and TG-DSC study of hydration of Sc-doped  $\text{CaSnO}_3$  and  $\text{CaZrO}_3$ . *Solid State Ionics*, 267:61–67, 2014. doi: 10.1016/j.ssi.2014.09.006.
- [75] F. Krug, T. Schober, and T. Springer. In-situ measurements of the water uptake in Yb-doped  $\text{SrCeO}_3$ . *Solid State Ionics*, 81:111–118, 1995.
- [76] Jin Suntivich, Kevin J. May, Hubert A. Gasteiger, John B. Goodenough, and Yang Shao-Horn. A perovskite oxide optimized for oxygen evolution catalysis from molecular orbital principles, December 2011.
- [77] A. A. Taskin, A. N. Lavrov, and Yoichi Ando. Achieving fast oxygen diffusion in perovskites by cation ordering. *Appl. Phys. Lett*, 86:91910, 2005. doi: 10.1063/1.1864244.
- [78] Carlos Bernuy-Lopez, Laura Rioja-Monllor, Takashi Nakamura, Sandrine Ricote, Ryan O’Hayre, Koji Amezawa, Mari-Ann Einarsrud, and Tor Grande. Effect of cation ordering on the performance and chemical stability of layered double perovskite cathodes. *Materials*, 11(2):196, January 2018. ISSN 1996-1944. doi: 10.3390/ma11020196.
- [79] Reihaneh Zohourian, Rotraut Merkle, Giulia Raimondi, and Joachim Maier. Mixed-conducting perovskites as cathode materials for protonic ceramic fuel cells: understanding the trends in proton uptake. *Adv. Funct. Mater.*, page 1801241, July 2018. ISSN 1616301X. doi: 10.1002/adfm.201801241.

- [80] A. Arulraj, F. Goutenoire, M. Tabellout, O. Bohnke, and P. Lacorre. Synthesis and characterization of the anionic conductor system  $\text{La}_2\text{Mo}_2\text{O}_{9-0.5x}\text{F}_x$  ( $x = 0.02-0.30$ ). *Chem. Mater.*, 14:2492–2498, 2002. doi: 10.1021/CM011239X.
- [81] I. Animitsa, N. Tarasova, and Ya. Filinkova. Electrical properties of the fluorine-doped  $\text{Ba}_2\text{In}_2\text{O}_5$ . *Solid State Ionics*, 207:29–37, January 2012. ISSN 0167-2738. doi: 10.1016/J.SSI.2011.11.015.
- [82] G. V. Gibbs, F. C. Hilf, M. B. Boisen, and R. T. Downs. Power law relationships between bond length, bond strength and electron density distributions. *Phys. Chem. Miner.*, 25:585–590, 1998.
- [83] Zhenbao Zhang, Yinlong Zhu, Yijun Zhong, Wei Zhou, and Zongping Shao. Anion doping: a new strategy for developing high-performance perovskite-type cathode materials of solid oxide fuel cells. *Adv. Energy Mater.*, 7(17):1700242, September 2017. ISSN 16146832. doi: 10.1002/aenm.201700242.
- [84] Hailei Zhao, Nansheng Xu, Yunfei Cheng, Wenjing Wei, Ning Chen, Weizhong Ding, Xionggang Lu, and Fushen Li. Investigation of mixed conductor  $\text{BaCo}_{0.7}\text{Fe}_{0.3-x}\text{Y}_x\text{O}_{3-\delta}$  with high oxygen permeability. *J. Phys. Chem. C*, 114(41):17975–17981, October 2010. ISSN 1932-7447. doi: 10.1021/jp106220z.
- [85] J. Suntivich and Y. Shao-Horn. Trend in oxygen reduction reaction on transition metal oxide surfaces. *ECS Trans.*, 58(1):715–726, 2013. doi: 10.1149/05801.0715ecst.
- [86] Ana B. Muñoz-García and Michele Pavone. From oxide to proton conduction: a quantum-chemical perspective on the versatility of  $\text{Sr}_2\text{Fe}_{1.5}\text{Mo}_{0.5}\text{O}_{6-\delta}$ -based materials. *Int. J. Quantum Chem.*, 116(21):1501–1506, November 2016. ISSN 00207608. doi: 10.1002/qua.25170.
- [87] Ronald L. Cook and Anthony F. Sammells. On the systematic selection of perovskite solid electrolytes for intermediate temperature fuel cells. *Solid State Ionics*, 45:311–321, 1991.
- [88] K. Belova, S. Baskakova, Chr. Argirusis, and I. Animitsa. The effect of  $\text{F}^-$ -doping on the conductivity of proton conductor  $\text{Ba}_4\text{Ca}_2\text{Nb}_2\text{O}_{11}$ . *Electrochim. Acta*, 193:63–71, March 2016. ISSN 0013-4686. doi: 10.1016/J.ELECTACTA.2016.02.052.
- [89] Emiliana Fabbri, Daniele Pergolesi, and Enrico Traversa. Electrode materials: a challenge for the exploitation of protonic solid oxide fuel cells. *Sci. Technol. Adv. Mater.*, 11(4):044301, February 2010. ISSN 1468-6996. doi: 10.1088/1468-6996/11/4/044301.
- [90] Emiliana Fabbri, Isaac Markus, Lei Bi, Daniele Pergolesi, and Enrico Traversa. Tailoring mixed proton-electronic conductivity of  $\text{BaZrO}_3$  by Y and Pr co-doping for cathode application in protonic SOFCs. *Solid State Ionics*, 202:30–35, 2011. doi: 10.1016/j.ssi.2011.08.019.
- [91] Yao Wang, Han Wang, Tong Liu, Fanglin Chen, and Changrong Xia. Improving the chemical stability of  $\text{BaCe}_{0.8}\text{Sm}_{0.2}\text{O}_{3-\delta}$  electrolyte by Cl doping for proton-conducting solid oxide fuel cell. *Electrochem. commun.*, 28:87–90, March 2013. ISSN 1388-2481. doi: 10.1016/J.ELECOM.2012.12.012.
- [92] Yuansong Wang, Huaiwen Nie, Shaorong Wang, Ting Lian Wen, Ulrich Guth, and Vladimir Valshook.  $\text{A}_{2-\alpha}\text{A}'_{\alpha}\text{BO}_4$ -type oxides as cathode materials for IT-SOFCs ( $\text{A}=\text{Pr},\text{Sm}$ ;  $\text{A}'=\text{Sr}$ ;  $\text{B}=\text{Fe},\text{Co}$ ). *Mater. Lett.*, 60:1174–1178, 2006. ISSN 0167577X. doi: 10.1016/j.matlet.2005.10.104.
- [93] N. A. Tarasova and I. E. Animitsa. Effect of anion doping on mobility of ionic charge carriers in solid solutions based on  $\text{Ba}_2\text{In}_2\text{O}_5$ . *Russ. J. Electrochem.*, 49(7):698–703, July 2013. ISSN 1023-1935. doi: 10.1134/S1023193513070161.

- [94] J. Lagaeva, D. Medvedev, A. Demin, and P. Tsiakaras. Insights on thermal and transport features of  $\text{BaCe}_{0.8-x}\text{Zr}_x\text{Y}_{0.2}\text{O}_{3-\delta}$  proton-conducting materials. *J. Power Sources*, 278:436–444, 2015. doi: 10.1016/j.jpowsour.2014.12.024.
- [95] V. V. Kharton, A. P. Viskup, E. N. Naumovich, and N. M. Lapchuk. Mixed electronic and ionic conductivity of  $\text{LaCo(M)O}_3$  (M=Ga, Cr, Fe or Ni). I. Oxygen transport in perovskites  $\text{LaCoO}_3$ – $\text{LaGaO}_3$ . *Solid State Ionics*, 104(1-2):67–78, December 1997. ISSN 01672738. doi: 10.1016/S0167-2738(97)00397-4.
- [96] Aron Walsh and Alex Zunger. Instilling defect tolerance in new compounds. *Nat. Mater.*, 16: 964–967, 2017. doi: 10.1038/nmat.4973.
- [97] R. Zohourian, R. Merkle, and J. Maier. Proton uptake into the protonic cathode material  $\text{BaCo}_{0.4}\text{Fe}_{0.4}\text{Zr}_{0.2}\text{O}_{3-\delta}$  and comparison to protonic electrolyte materials. *Solid State Ionics*, 299: 64–69, 2017. doi: 10.1016/j.ssi.2016.09.012.
- [98] Zeng-qiang Deng, Guo-guang Zhang, Wei Liu, Ding-kun Peng, and Chu-sheng Chen. Phase composition, oxidation state and electrical conductivity of  $\text{SrFe}_{1.5-x}\text{Co}_x\text{O}_y$ . *Solid State Ionics*, 152-153:735–739, December 2002. ISSN 01672738. doi: 10.1016/S0167-2738(02)00317-X.
- [99] Ana B. Muñoz-García and Michele Pavone. First-principles design of new electrodes for proton-conducting solid-oxide electrochemical cells: A-site doped  $\text{Sr}_2\text{Fe}_{1.5}\text{Mo}_{0.5}\text{O}_{6-\delta}$  perovskite. *Chem. Mater.*, 28:490–500, 2016. doi: 10.1021/acs.chemmater.5b03262.
- [100] Xi Xu, Huiqiang Wang, Marco Fronzi, Xianfen Wang, Lei Bi, and Enrico Traversa. Tailoring cations in a perovskite cathode for proton-conducting solid oxide fuel cells with high performance. *J. Mater. Chem. A*, 7(36):20624–20632, September 2019. ISSN 2050-7488. doi: 10.1039/C9TA05300J.
- [101] Lei Ge, Wei Zhou, Ran Ran, Shaomin Liu, Zongping Shao, Wanqin Jin, and Nanping Xu. Properties and performance of A-site deficient  $(\text{Ba}_{0.5}\text{Sr}_{0.5})_{1-x}\text{Co}_{0.8}\text{Fe}_{0.2}\text{O}_{3-\delta}$  for oxygen permeating membrane. *J. Memb. Sci.*, 306(1-2):318–328, December 2007. ISSN 0376-7388. doi: 10.1016/J.MEMSCI.2007.09.004.
- [102] Youmin Guo, Ran Ran, Zongping Shao, and Shaomin Liu. Effect of Ba nonstoichiometry on the phase structure, sintering, electrical conductivity and phase stability of  $\text{Ba}_{1\pm x}\text{Ce}_{0.4}\text{Zr}_{0.4}\text{Y}_{0.2}\text{O}_{3-\delta}$  ( $0 \leq x \leq 0.20$ ) proton conductors. *Int. J. Hydrogen Energy*, 36(14):8450–8460, July 2011. ISSN 03603199. doi: 10.1016/j.ijhydene.2011.04.037.
- [103] Yoshihiro Yamazaki, Raul Hernandez-Sanchez, and Sossina M. Haile. Cation non-stoichiometry in yttrium-doped barium zirconate: phase behavior, microstructure, and proton conductivity. *J. Mater. Chem.*, 20:8158–8166, 2010. doi: 10.1039/c0jm02013c.
- [104] N. Tarasova, I. Animitsa, T. Denisova, and R. Nevmyvako. The influence of fluorine doping on short-range structure in brownmillerite  $\text{Ba}_{1.95}\text{In}_2\text{O}_{4.9}\text{F}_{0.1}$ . *Solid State Ionics*, 275:47–52, July 2015. ISSN 0167-2738. doi: 10.1016/J.SSI.2015.02.009.
- [105] N. Tarasova and I. Animitsa. Novel proton-conducting oxyfluorides  $\text{Ba}_{4-0.5x}\text{In}_2\text{Zr}_2\text{O}_{11-x}\text{F}_x$  with perovskite structure. *Solid State Ionics*, 264:69–75, October 2014. ISSN 0167-2738. doi: 10.1016/J.SSI.2014.06.021.
- [106] N. A. Tarasova, N. A. Zhuravlev, I. E. Animitsa, T. A. Denisova, Ya. V. Baklanova, and V. Ya. Kavun. Features of the local structure of hydrated fluorine-substituted solid solutions based on  $\text{Ba}_2\text{In}_2\text{O}_5$ . *Bull. Russ. Acad. Sci. Phys.*, 78(8):730–732, August 2014. ISSN 1062-8738. doi: 10.3103/S1062873814080371.

- [107] Ana B. Muñoz-García and Michele Pavone. K-doped  $\text{Sr}_2\text{Fe}_{1.5}\text{Mo}_{0.5}\text{O}_{6-\delta}$  predicted as a bifunctional catalyst for air electrodes in proton-conducting solid oxide electrochemical cells. *J. Mater. Chem. A*, 5(25):12735–12739, June 2017. ISSN 2050-7488. doi: 10.1039/C7TA03340K.
- [108] Yueh-Lin Lee, Jesper Kleis, Jan Rossmeisl, Yang Shao-Horn, and Dane Morgan. Prediction of solid oxide fuel cell cathode activity with first-principles descriptors. *Energy Environ. Sci.*, 4:3966–3970, 2011. doi: 10.1039/c1ee02032c.
- [109] Xuefeng Zhu and Weishen Yang. Fabrication and characterization of MIEC membranes. In *Mix. Conduct. Ceram. Membr. Fundam. Mater. Appl.*, pages 95–143. Springer, Berlin, Heidelberg, 2017. ISBN 978-3-662-53534-9. doi: 10.1007/978-3-662-53534-9\_4.
- [110] D. Pérez-Coll, G. Heras-Juaristi, D. P. Fagg, and G. C. Mather. Methodology for the study of mixed transport properties of a Zn-doped  $\text{SrZr}_{0.9}\text{Y}_{0.1}\text{O}_{3-\delta}$  electrolyte under reducing conditions. *J. Mater. Chem. A*, 3(20):11098–11110, May 2015. ISSN 2050-7488. doi: 10.1039/C5TA01452B.
- [111] Huayang Zhu, Sandrine Ricote, Chuancheng Duan, Ryan P. O’Hayre, Dmitry S. Tsvetkov, and Robert J. Kee. Defect incorporation and transport within dense  $\text{BaZr}_{0.8}\text{Y}_{0.2}\text{O}_{3-\delta}$  (BZY20) proton-conducting membranes. *J. Electrochem. Soc.*, 165(9):581–588, 2018. doi: 10.1149/2.0161809jes.
- [112] Wei Lai and Sossina M. Haile. Impedance spectroscopy as a tool for chemical and electrochemical analysis of mixed conductors: a case study of ceria. *J. Am. Ceram. Soc.*, 88(11):2979–2997, November 2005. ISSN 0002-7820. doi: 10.1111/j.1551-2916.2005.00740.x.
- [113] J Jamnik and J Maier. Treatment of the impedance of mixed conductors equivalent circuit model and explicit approximate solutions. *J. Electrochem. Soc.*, 146(11):4183–4188, 1999.
- [114] H Schichlein, A C Muller, M Voigts, A Krugel, and E Ivers-Tiffée. Deconvolution of electrochemical impedance spectra for the identification of electrode reaction mechanisms in solid oxide fuel cells. *J. Appl. Electrochem.*, 32:875–882, 2002.
- [115] Francesco Ciucci and Chi Chen. Analysis of electrochemical impedance spectroscopy data using the distribution of relaxation times: a Bayesian and hierarchical Bayesian approach. *Electrochim. Acta*, 167:439–454, June 2015. ISSN 0013-4686. doi: 10.1016/J.ELECTACTA.2015.03.123.
- [116] Yang Chen, Tao Hong, Piaopiao Wang, Kyle Brinkman, Jianhua Tong, and Jigui Cheng. Investigate the proton uptake process of proton/oxygen ion/hole triple conductor  $\text{BaCo}_{0.4}\text{Fe}_{0.4}\text{Zr}_{0.1}\text{Y}_{0.1}\text{O}_{3-\delta}$  by electrical conductivity relaxation. *J. Power Sources*, 440:227122, November 2019. ISSN 0378-7753. doi: 10.1016/J.JPOWSOUR.2019.227122.
- [117] J.A. Lane and J.A. Kilner. Measuring oxygen diffusion and oxygen surface exchange by conductivity relaxation. *Solid State Ionics*, 136-137:997–1001, November 2000. ISSN 0167-2738. doi: 10.1016/S0167-2738(00)00554-3.
- [118] Han-Il Yoo and Chung-Eun Lee. Conductivity relaxation patterns of mixed conductor oxides under a chemical potential gradient. *Solid State Ionics*, 180(4-5):326–337, April 2009. ISSN 0167-2738. doi: 10.1016/J.SSI.2009.01.001.
- [119] Bernard A. Boukamp, Matthijs W. den Otter, and Henny J. M. Bouwmeester. Transport processes in mixed conducting oxides: combining time domain experiments and frequency domain analysis. *J. Solid State Electrochem.*, 8:592–598, 2004. doi: 10.1007/s10008-003-0493-6.

- [120] M. W. den Otter, H. J. M. Bouwmeester, B. A. Boukamp, and H. Verweij. Reactor flush time correction in relaxation experiments. *J. Electrochem. Soc.*, 148(2):J1–J6, 2001. doi: 10.1149/1.1337604.
- [121] G. Kim, S. Wang, A. J. Jacobson, and C. L. Chen. Measurement of oxygen transport kinetics in epitaxial  $\text{La}_2\text{NiO}_{4+\delta}$  thin films by electrical conductivity relaxation. *Solid State Ionics*, 177(17-18): 1461–1467, July 2006. ISSN 0167-2738. doi: 10.1016/J.SSI.2006.07.013.
- [122] Han-Il Yoo, Je-Yong Yoon, Jin-Su Ha, and Chung-Eun Lee. Hydration and oxidation kinetics of a proton conductor oxide,  $\text{SrCe}_{0.95}\text{Yb}_{0.05}\text{O}_{2.975}$ . *Phys. Chem. Chem. Phys.*, 10(7):974–982, February 2008. ISSN 1463-9076. doi: 10.1039/B709371C.
- [123] Ted C. Yeh, Jules L. Routbort, and Thomas O. Mason. Oxygen transport and surface exchange properties of  $\text{Sr}_{0.5}\text{Sm}_{0.5}\text{CoO}_{3-\delta}$ . *Solid State Ionics*, 232:138–143, February 2013. ISSN 0167-2738. doi: 10.1016/J.SSI.2012.11.024.
- [124] A. Grimaud, J.-M. Bassat, F. Mauvy, M. Pollet, A. Wattiaux, M. Marrony, and J.-C. Grenier. Oxygen reduction reaction of  $\text{PrBaCo}_{2-x}\text{Fe}_x\text{O}_{5+\delta}$  compounds as  $\text{H}^+$ -SOFC cathodes: correlation with physical properties. *J. Mater. Chem. A*, 2:3594–3604, 2014. doi: 10.1039/c3ta13956e.
- [125] Dmitry Rupasov, Tatyana Makarenko, and Allan J. Jacobson. Oxygen diffusion in  $\text{Sr}_3\text{YCo}_4\text{O}_{10.5}$ : An electrical conductivity relaxation and thermogravimetric analysis approach. *Solid State Ionics*, 265: 68–72, November 2014. ISSN 0167-2738. doi: 10.1016/J.SSI.2014.07.010.
- [126] Andreas Falkenstein, David N. Mueller, Roger A. De Souza, and Manfred Martin. Chemical relaxation experiments on mixed conducting oxides with large stoichiometry deviations. *Solid State Ionics*, 280:66–73, November 2015. ISSN 0167-2738. doi: 10.1016/J.SSI.2015.07.023.
- [127] J.A. Kilner, A. Berenov, and J. Rossiny. Diffusivity of the oxide ion in perovskite oxides. In *Perovskite Oxide Solid Oxide Fuel Cells*, pages 95–116. Springer, Boston, MA, 2009. doi: 10.1007/978-0-387-77708-5\\_5.
- [128] F. Mauvy, J. M. Bassat, E. Boehm, P. Dordor, J. C. Grenier, and J. P. Loup. Chemical oxygen diffusion coefficient measurement by conductivity relaxation — correlation between tracer diffusion coefficient and chemical diffusion coefficient. *J. Eur. Ceram. Soc.*, 24(6):1265–1269, January 2004. ISSN 0955-2219. doi: 10.1016/S0955-2219(03)00500-4.
- [129] David N. Mueller, Roger A. De Souza, Jochen Brendt, Dominik Samuelis, and Manfred Martin. Oxidation states of the transition metal cations in the highly nonstoichiometric perovskite-type oxide  $\text{Ba}_{0.1}\text{Sr}_{0.9}\text{Co}_{0.8}\text{Fe}_{0.2}\text{O}_{3-\delta}$ . *J. Mater. Chem.*, 19(14):1960, March 2009. ISSN 0959-9428. doi: 10.1039/b819415g.
- [130] J Mizusaki, Y Mima, S Yamauchi, and K Fueki. Nonstoichiometry of the perovskite-type oxides  $\text{La}_{1-x}\text{Sr}_x\text{CoO}_{3-\delta}$ . *J. Solid State Chem.*, 80:102–111, 1989.
- [131] Truls Norby. EMF method determination of conductivity contributions from protons and other foreign ions in oxides. *Solid State Ionics*, 28-30:1586–1591, September 1988. ISSN 0167-2738. doi: 10.1016/0167-2738(88)90424-9.
- [132] Euisung Kim, Jung In Yeon, Manfred Martin, and Han-Il Yoo. Experimental demonstration of the path- and time-dependence of open-circuit voltage of galvanic cells involving a multinary compound under multiple chemical potential gradients. *Solid State Ionics*, 235:22–31, March 2013. ISSN 0167-2738. doi: 10.1016/J.SSI.2013.01.006.

- [133] Domingo Pérez-Coll, Gemma Heras-Juaristi, Duncan P. Fagg, and Glenn C. Mather. Transport-number determination of a protonic ceramic electrolyte membrane via electrode-polarisation correction with the Gorelov method. *J. Power Sources*, 245:445–455, January 2014. ISSN 0378-7753. doi: 10.1016/J.JPOWSOUR.2013.06.155.
- [134] Je-Yong Yoon, Jung In Yeon, and Han-Ill Yoo. Concentration-cell measurement of proton transference number of  $\text{SrCe}_{0.95}\text{Yb}_{0.05}\text{O}_{3-\delta}$ . *Solid State Ionics*, 213:22–28, April 2012. ISSN 0167-2738. doi: 10.1016/J.SSI.2011.05.015.
- [135] R. A. De Souza, J. A. Kilner, and C. Jeynes. The application of secondary ion mass spectrometry (SIMS) to the study of high temperature proton conductors (HTPC). *Solid State Ionics*, 97:409–419, May 1997. ISSN 0167-2738. doi: 10.1016/S0167-2738(97)00038-6.
- [136] M. W. den Otter, B. A. Boukamp, and H. J. M. Bouwmeester. Theory of oxygen isotope exchange. *Solid State Ionics*, 139(1-2):89–94, January 2001. ISSN 0167-2738. doi: 10.1016/S0167-2738(00)00801-8.
- [137] Roger A. De Souza and Manfred Martin. Probing diffusion kinetics with secondary ion mass spectrometry. *MRS Bull.*, 34(12):907–914, December 2009. ISSN 0883-7694. doi: 10.1557/mrs2009.212.
- [138] L. Wang, R. Merkle, J. Maier, T. Acartürk, and U. Starke. Oxygen tracer diffusion in dense  $\text{Ba}_{0.5}\text{Sr}_{0.5}\text{Co}_{0.8}\text{Fe}_{0.2}\text{O}_{3-\delta}$  films. *Appl. Phys. Lett.*, 94(7):071908, February 2009. ISSN 0003-6951. doi: 10.1063/1.3085969.
- [139] John A. Kilner, Stephen J. Skinner, and Hidde H. Brongersma. The isotope exchange depth profiling (IEDP) technique using SIMS and LEIS. *J. Solid State Electrochem.*, 15(5):861–876, May 2011. ISSN 1432-8488. doi: 10.1007/s10008-010-1289-0.
- [140] Yi-Lin Huang, Christopher Pellegrinelli, and Eric D. Wachsman. Reaction kinetics of gas-solid exchange using gas phase isotopic oxygen exchange. *ACS Catal.*, 6:6025–6032, 2016. doi: 10.1021/acscatal.6b01462.
- [141] Shunyi Li, Feng Chen, Robert Schafrank, Thorsten J. M. Bayer, Karsten Rachut, Anne Fuchs, Sebastian Siol, Mirko Weidner, Mareike Hohmann, Verena Pfeifer, Jan Morasch, Cosmina Ghinea, Emmanuel Arveux, Richard Günzler, Jürgen Gassmann, Christoph Körber, Yvonne Gassenbauer, Frank Säuberlich, Gutlapalli Venkata Rao, Sandrine Payan, Mario Maglione, Cristina Chirila, Lucian Pintilie, Lichao Jia, Klaus Ellmer, Michael Naderer, Klaus Reichmann, Ulrich Böttger, Sebastian Schmelzer, Raluca C Frunza, Hana Uršič, Barbara Malič, Wen-Bin Wu, Paul Erhart, and Andreas Klein. Intrinsic energy band alignment of functional oxides. *Phys. Status Solidi RRL*, 8(6):571–576, 2014. doi: 10.1002/pssr.201409034.
- [142] Janakiraman Balachandran, Lianshan Lin, Jonathan S. Ansell, Craig A. Bridges, and P. Ganesh. Defect genome of cubic perovskites for fuel cell applications. *J. Phys. Chem. C*, 121:26637–26647, 2017. doi: 10.1021/acs.jpcc.7b08716.
- [143] Liu Liang, Lu Wencong, and Chen Nianyi. On the criteria of formation and lattice distortion of perovskite-type complex halides. *J. Phys. Chem. Solids*, 65(5):855–860, May 2004. ISSN 00223697. doi: 10.1016/j.jpcs.2003.08.021.
- [144] Harumi Yokokawa, Natsuko Sakai, Tatsuya Kawada, and Masayuki Dokiya. Thermodynamic stability of perovskites and related compounds in some alkaline earth-transition metal-oxygen systems. *J. Solid State Chem.*, 94(1):106–120, September 1991. ISSN 0022-4596. doi: 10.1016/0022-4596(91)90225-7.

- [145] Dongguo Li, Haifeng Lv, Yijin Kang, Nenad M. Markovic, and Vojislav R. Stamenkovic. Progress in the development of oxygen reduction reaction catalysts for low-temperature fuel cells. *Annu. Rev. Chem. Biomol. Eng.*, 7:509–532, June 2016. ISSN 1947-5438. doi: 10.1146/annurev-chembioeng-080615-034526.
- [146] J. T. S. Irvine. Perovskite oxide anodes for SOFCs. In *Perovskite Oxide Solid Oxide Fuel Cells*, chapter 8, pages 167–182. Springer, Boston, MA, 2009. doi: 10.1007/978-0-387-77708-5\8.
- [147] Colin M. Gore, Joseph O. White, Eric D. Wachsman, and Venkataraman Thangadurai. Effect of composition and microstructure on electrical properties and CO<sub>2</sub> stability of donor-doped, proton conducting BaCe<sub>1-(x+y)</sub>Zr<sub>x</sub>Nb<sub>y</sub>O<sub>3</sub>. *J. Mater. Chem. A*, 2(7):2363–2373, January 2014. ISSN 2050-7488. doi: 10.1039/c3ta12668d.
- [148] Chris G. Van de Walle and J. Neugebauer. Universal alignment of hydrogen levels in semiconductors, insulators and solutions. *Nature*, 423(6940):626–628, June 2003. ISSN 0028-0836. doi: 10.1038/nature01665.
- [149] Chris G. Van de Walle and Jörg Neugebauer. Hydrogen in semiconductors. *Annu. Rev. Mater. Res.*, 36(1):179–198, August 2006. ISSN 1531-7331. doi: 10.1146/annurev.matsci.36.010705.155428.
- [150] John Robertson. Band offsets, Schottky barrier heights, and their effects on electronic devices. *J. Vac. Sci. Technol. A Vacuum, Surfaces, Film.*, 31(5):050821, September 2013. ISSN 0734-2101. doi: 10.1116/1.4818426.
- [151] Christoph Freysoldt, Blazej Grabowski, Tilmann Hickel, Jörg Neugebauer, Georg Kresse, Anderson Janotti, and Chris G. Van de Walle. First-principles calculations for point defects in solids. *Rev. Mod. Phys.*, 86(1):253–305, March 2014. ISSN 0034-6861. doi: 10.1103/RevModPhys.86.253.
- [152] Anuj Goyal, Prashun Gorai, Haowei Peng, Stephan Lany, and Vladan Stevanović. A computational framework for automation of point defect calculations. *Comput. Mater. Sci.*, 130:1–9, April 2017. ISSN 0927-0256. doi: 10.1016/J.COMMATSCI.2016.12.040.
- [153] Anuj Goyal and Vladan Stevanović. Metastable rocksalt ZnO is p-type dopable. *Phys. Rev. Mater.*, 2(8):084603, August 2018. ISSN 2475-9953. doi: 10.1103/PhysRevMaterials.2.084603.
- [154] J. C. Booth, Dong Ho Wu, and Steven M. Anlage. A broadband method for the measurement of the surface impedance of thin films at microwave frequencies. *Rev. Sci. Instrum.*, 65:2082, 1994. doi: 10.1063/1.1144816.
- [155] Yil-Hwan You, Byung-Soo So, Jin-Ha Hwang, Wontae Cho, Sun Sook Lee, Taek-Mo Chung, Chang Gyoun Kim, and Ki-Seok An. Impedance spectroscopy characterization of resistance switching NiO thin films prepared through atomic layer deposition. *Appl. Phys. Lett.*, 89(22):222105, November 2006. ISSN 0003-6951. doi: 10.1063/1.2392991.
- [156] Jiagang Wu and John Wang. Ferroelectric and impedance behavior of La- and Ti-codoped BiFeO<sub>3</sub> thin films. *J. Am. Ceram. Soc.*, 93(9):2795–2803, April 2010. ISSN 00027820. doi: 10.1111/j.1551-2916.2010.03816.x.
- [157] Y. Y. Proskuryakov, K. Durose, M. K. Al Turkestani, I. Mora-Seró, G. Garcia-Belmonte, F. Fabregat-Santiago, J. Bisquert, V. Barrioz, D. Lamb, S. J. C. Irvine, and E. W. Jones. Impedance spectroscopy of thin-film CdTe/CdS solar cells under varied illumination. *J. Appl. Phys.*, 106(4):044507, August 2009. ISSN 0021-8979. doi: 10.1063/1.3204484.

- [158] J. E. Bauerle. Study of solid electrolyte polarization by a complex admittance method. *J. Phys. Chem. Solids*, 30(12):2657–2670, December 1969. ISSN 00223697. doi: 10.1016/0022-3697(69)90039-0.
- [159] D. Poetzsch, R. Merkle, and J. Maier. Stoichiometry variation in materials with three mobile carriers-thermodynamics and transport kinetics exemplified for protons, oxygen vacancies, and holes. *Adv. Funct. Mater.*, 25(10):1542–1557, March 2015. ISSN 1616301X. doi: 10.1002/adfm.201402212.
- [160] Martin L. Green, Ichiro Takeuchi, and Jason R. Hattrick-Simpers. Applications of high throughput (combinatorial) methodologies to electronic, magnetic, optical, and energy-related materials. *J. Appl. Phys.*, 113(23):231101, June 2013. ISSN 0021-8979. doi: 10.1063/1.4803530.
- [161] K. C. Hewitt, P. A. Casey, R. J. Sanderson, M. A. White, and R. Sun. High-throughput resistivity apparatus for thin-film combinatorial libraries. *Rev. Sci. Instrum.*, 76(9):093906, September 2005. ISSN 0034-6748. doi: 10.1063/1.2037947.
- [162] Shrisudersan Jayaraman, Sung-Hyeon Baek, Thomas F. Jaramillo, Alan Kleiman-Shwarsctein, and Eric W. McFarland. Combinatorial electrochemical synthesis and screening of pt-wo<sub>3</sub> catalysts for electro-oxidation of methanol. *Rev. Sci. Instrum.*, 76(6):062227, June 2005. ISSN 0034-6748. doi: 10.1063/1.1927007.
- [163] F.S. Baumann, J. Fleig, H.-U. Habermeier, and J. Maier. Ba<sub>0.5</sub>Sr<sub>0.5</sub>Co<sub>0.8</sub>Fe<sub>0.2</sub>O<sub>3-δ</sub> thin film microelectrodes investigated by impedance spectroscopy. *Solid State Ionics*, 177(35-36):3187–3191, November 2006. ISSN 0167-2738. doi: 10.1016/J.SSI.2006.07.057.
- [164] Sebastian Stämmler, Rotraut Merkle, and Joachim Maier. Oxygen exchange activity of La-Sr-Co-O PLD films and quantification of (La,Sr)CoO<sub>3-δ</sub>/(La,Sr)<sub>2</sub>CoO<sub>4+δ</sub>/O<sub>2</sub> triple phase boundary activity. *J. Electrochem. Soc.*, 164(4):F454–F463, March 2017. ISSN 0013-4651. doi: 10.1149/2.0101706jes.
- [165] Robert E. Usiskin, Shingo Maruyama, Chris J. Kucharczyk, Ichiro Takeuchi, and Sossina M. Haile. Probing the reaction pathway in (La<sub>0.8</sub>Sr<sub>0.2</sub>)<sub>0.95</sub>MnO<sub>3+δ</sub> using libraries of thin film microelectrodes. *J. Mater. Chem. A*, 3(38):19330–19345, September 2015. ISSN 2050-7488. doi: 10.1039/C5TA02428E.
- [166] Ruiyun Huang, Chris J. Kucharczyk, Yangang Liang, Xiaohang Zhang, Ichiro Takeuchi, and Sossina M. Haile. Out-of-plane ionic conductivity measurement configuration for high-throughput experiments. *ACS Comb. Sci.*, 20(7):443–450, July 2018. ISSN 2156-8952. doi: 10.1021/acscmbosci.8b00037.
- [167] H. Duan, C. C. Yuan, N. Becerra, L. J. Small, A. Chang, J. M. Gregoire, and R. B. van Dover. High-throughput measurement of ionic conductivity in composition-spread thin films. *ACS Comb. Sci.*, 15(6):273–7, June 2013. ISSN 2156-8944. doi: 10.1021/co4000375.
- [168] T. H. Muster, A. Trinchi, T. A. Markley, D. Lau, P. Martin, A. Bradbury, A. Bendavid, and S. Dligatch. A review of high throughput and combinatorial electrochemistry. *Electrochim. Acta*, 56(27):9679–9699, November 2011. ISSN 00134686. doi: 10.1016/j.electacta.2011.09.003.
- [169] Jürgen Fleig. Microelectrodes in solid state ionics. In *Adv. Electrochem. Sci. Eng. Vol. 8*, pages 1–87. 2002.
- [170] Ikwhang Chang, Jun Yeol Paek, and Suk Won Cha. Parametric study of Y-doped BaZrO<sub>3</sub> thin film deposited via pulsed laser deposition. *J. Vac. Sci. Technol. A Vacuum, Surfaces, Film.*, 33(2):021515, March 2015. ISSN 0734-2101. doi: 10.1116/1.4905775.

- [171] E. Navickas, M. Gerstl, G. Friedbacher, F. Kubel, and J. Fleig. Measurement of the across-plane conductivity of YSZ thin films on silicon. *Solid State Ionics*, 211:58–64, 2012. doi: 10.1016/j.ssi.2012.01.007.
- [172] Peter Babilo, Tetsuya Uda, and Sossina M. Haile. Processing of yttrium-doped barium zirconate for high proton conductivity. *J. Mater. Res.*, 22(5):1322–1330, 2007. doi: 10.1557/JMR.2007.0163.
- [173] Prakash Periasamy, Joseph J. Berry, Arrelaine A. Dameron, Jeremy D. Bergeson, David S. Ginley, Ryan P. O’Hayre, and Philip A. Parilla. Fabrication and characterization of MIM diodes based on Nb/Nb<sub>2</sub>O<sub>5</sub> via a rapid screening technique. *Adv. Mater.*, 23(27):3080–3085, July 2011. ISSN 09359648. doi: 10.1002/adma.201101115.
- [174] M. Gerstl, E. Navickas, G. Friedbacher, F. Kubel, M. Ahrens, and J. Fleig. The separation of grain and grain boundary impedance in thin yttria stabilized zirconia (YSZ) layers. *Solid State Ionics*, 185(1):32–41, March 2011. ISSN 01672738. doi: 10.1016/j.ssi.2011.01.008.
- [175] Kevin R. Talley, Sage R. Bauers, Celeste L. Melamed, Meagan C. Papac, Karen N. Heinselman, Imran Khan, Dennice M. Roberts, Valerie Jacobson, Allison Mis, Geoff L. Brennecke, John D. Perkins, and Andriy Zakutayev. COMBIgor: data-analysis package for combinatorial materials science. *ACS Comb. Sci.*, 21(7):537–547, July 2019. ISSN 2156-8952. doi: 10.1021/acscombsci.9b00077.
- [176] Jake Huang, Meagan Papac, and Ryan O’Hayre. Towards robust autonomous impedance spectroscopy analysis: A calibrated hierarchical Bayesian approach for electrochemical impedance spectroscopy (EIS) inversion. *Electrochim. Acta*, page 137493, November 2020. ISSN 0013-4686. doi: 10.1016/j.electacta.2020.137493.
- [177] Baoyuan Wang, Shuisong Chen, Wenjing Dong, Xunying Wang, Liangping Shen, and Hao Wang. Advance fuel cells using Al<sub>2</sub>O<sub>3</sub>-nNaAlO<sub>2</sub> composite as ion-conducting membrane. *Int. J. Hydrogen Energy*, 43:12847–12855, July 2018. ISSN 0360-3199. doi: 10.1016/J.IJHYDENE.2018.04.149.
- [178] Liangdong Fan and Pei-Chen Su. Layer-structured LiNi<sub>0.8</sub>Co<sub>0.2</sub>O<sub>2</sub> : A new triple (H<sup>+</sup>/O<sup>2-</sup>/e<sup>-</sup>) conducting cathode for low temperature proton conducting solid oxide fuel cells. *J. Power Sources*, 306:369–377, 2016. doi: 10.1016/j.jpowsour.2015.12.015.
- [179] Alexis Grimaud, Fabrice Mauvy, Jean Marc Bassat, Fourcade Sebastien, Mathieu Marrony, and Jean Claude Grenier. Hydration and transport properties of the Pr<sub>2-x</sub>Sr<sub>x</sub>NiO<sub>4+δ</sub> compounds as H<sup>+</sup>-SOFC cathodes. *J. Mater. Chem.*, 22:16017–16025, 2012. doi: 10.1039/c2jm31812a.
- [180] Cuijuan Zhang and Hailei Zhao. A novel cobalt-free cathode material for proton-conducting solid oxide fuel cells. *J. Mater. Chem.*, 22(35):18387, August 2012. ISSN 0959-9428. doi: 10.1039/c2jm32627b.
- [181] JIanc Kai, He Zhiqi, Meng Jian, Ren Yufang, and Su Qiang. Low temperature preparation and fuel cell properties of rare earth doped barium cerate solid electrolytes. *Sci. China*, 42(3):298–304, 1999.
- [182] E. Quarez, Y. Oumellal, and O. Joubert. Optimization of the lanthanum tungstate/ Pr<sub>2</sub>NiO<sub>4</sub> half cell for application in proton conducting solid oxide fuel cells. *Fuel Cells*, 13(1):34–41, February 2013. ISSN 16156846. doi: 10.1002/fuce.201200091.
- [183] Kiho Bae, Dong Young Jang, Sung Min Choi, Byung-Kook Kim, Jong-Ho Lee, Ji-Won Son, and Joon Hyung Shim. Influence of background oxygen pressure on film properties of pulsed laser deposited Y:BaZrO<sub>3</sub>. *Thin Solid Films*, 552:24–31, February 2014. ISSN 0040-6090. doi: 10.1016/J.TSF.2013.12.006.

- [184] Meagan Papac, Vladan Stevanović, Andriy Zakutayev, and Ryan O’Hayre. Triple ionic-electronic conducting oxides for next-generation electrochemical devices. *Nat. Mater.*, 2020. doi: 10.1038/s41563-020-00854-8.
- [185] Zhenbin Wang, Wenqiang Yang, Zhuoying Zhu, Ranran Peng, Xiaojun Wu, Changrong Xia, and Yalin Lu. First-principles study of O<sub>2</sub> reduction on BaZr<sub>1-x</sub>Co<sub>x</sub>O<sub>3</sub> cathodes in protonic-solid oxide fuel cells. *J. Mater. Chem. A*, 2(39):16707–16714, September 2014. ISSN 2050-7488. doi: 10.1039/C4TA01652A.
- [186] Yuanyuan Rao, Shenghong Zhong, Fei He, Zhenbin Wang, Ranran Peng, and Yalin Lu. Cobalt-doped BaZrO<sub>3</sub>: A single phase air electrode material for reversible solid oxide cells. *Int. J. Hydrogen Energy*, 37(17):12522–12527, September 2012. ISSN 0360-3199. doi: 10.1016/J.IJHYDENE.2012.05.022.
- [187] Meng Shang, Jianhua Tong, and Ryan O’Hayre. A promising cathode for intermediate temperature protonic ceramic fuel cells: BaCo<sub>0.4</sub>Fe<sub>0.4</sub>Zr<sub>0.2</sub>O<sub>3-δ</sub>. *RSC Adv.*, 3(36):15769, August 2013. ISSN 2046-2069. doi: 10.1039/c3ra41828f.
- [188] Ken Watanabe, Daisuke Takauchi, Masayoshi Yuasa, Tetsuya Kida, Kengo Shimano, Yasutake Teraoka, and Noboru Yamazoe. Oxygen permeation properties of Co-free perovskite-type oxide membranes based on BaFe<sub>1-y</sub>Zr<sub>y</sub>O<sub>3-δ</sub>. *J. Electrochem. Soc.*, 156(5):E81–E85, 2009.
- [189] Hong Liu, Jie Yu, Jaka Sunarso, Chuan Zhou, Bo Liu, Yujuan Shen, Wei Zhou, and Zongping Shao. Mixed protonic-electronic conducting perovskite oxide as a robust oxygen evolution reaction catalyst. *Electrochim. Acta*, 282:324–330, August 2018. ISSN 0013-4686. doi: 10.1016/J.ELECTACTA.2018.06.073.
- [190] Fumitada Iguchi, Noriko Sata, Takao Tsurui, and Hiroo Yugami. Microstructures and grain boundary conductivity of BaZr<sub>1-x</sub>Y<sub>x</sub>O<sub>3</sub> (x = 0.05, 0.10, 0.15) ceramics. *Solid State Ionics*, 178: 691–695, 2007. doi: 10.1016/j.ssi.2007.02.019.
- [191] Sangbong Ryu, Sanghoon Lee, Wonyeop Jeong, Arunkumar Pandiyan, Suresh Babu Krishna Moorthy, Ikwhang Chang, Taehyun Park, and Suk Won Cha. Pulsed laser deposition of BaCo<sub>0.4</sub>Fe<sub>0.4</sub>Zr<sub>0.1</sub>Y<sub>0.1</sub>O<sub>3-δ</sub> cathode for solid oxide fuel cells. *Surf. Coatings Technol.*, 369:265–268, July 2019. ISSN 0257-8972. doi: 10.1016/J.SURFCOAT.2019.01.034.
- [192] Xu Kuai, Guangming Yang, Yubo Chen, Hainan Sun, Jie Dai, Yufei Song, Ran Ran, Wei Wang, Wei Zhou, and Zongping Shao. Boosting the activity of BaCo<sub>0.4</sub>Fe<sub>0.4</sub>Zr<sub>0.1</sub>Y<sub>0.1</sub>O<sub>3-δ</sub> perovskite for oxygen reduction reactions at low-to-intermediate temperatures through tuning B-site cation deficiency. *Adv. Energy Mater.*, 9(38):1902384, October 2019. ISSN 1614-6832. doi: 10.1002/aenm.201902384.
- [193] Y. Teraoka, H.M. Zhang, K. Okamoto, and N. Yamazoe. Mixed ionic-electronic conductivity of chLa<sub>1-x</sub>Sr<sub>x</sub>Co<sub>1-y</sub>Fe<sub>y</sub>O<sub>3-δ</sub> perovskite-type oxides. *Mater. Res. Bull.*, 23(1):51–58, January 1988. ISSN 00255408. doi: 10.1016/0025-5408(88)90224-3.
- [194] Meagan C. Papac, Kevin R. Talley, Ryan P. O’Hayre, and Andriy Zakutayev. Instrument for spatially resolved, temperature-dependent electrochemical impedance spectroscopy of thin films under controlled atmosphere. In revision.
- [195] John Irvine, Jennifer Rupp, Gang Liu, Xiaoxiang Xu, Sossina Haile, Xin Qian, Alem Snyder, Robert Freer, Dursun Ekren, Stephen Skinner, Ozden Celikbilek, Shigang Chen, Shanwen Tao, Tae Ho Shin, Ryan O’Hayre, Jake Huang, Meagan Papac, Chuancheng Duan, Shuangbin Li, Andrea Russel, Veronica Celorrio, B Hayden, Hugo Nolan, Xiubing Huang, Ge Wang, Ian Metcalfe, Dragos Neagu, and Susana Martin. Roadmap on inorganic perovskites for energy applications. *J. Phys. Energy. In press*.

- [196] Samantha Millican, Ann Deml, Meagan Papac, Andriy Zakutayev, Ryan O'Hayre, Aaron Holder, Charles Musgrave, and Vladan Stevanović. Predicting oxygen off-stoichiometry and hydrogen incorporation in complex perovskite oxides. In revision.

APPENDIX A  
SUPPLEMENTAL INFORMATION FOR INSTRUMENT FOR SPATIALLY RESOLVED,  
TEMPERATURE-DEPENDENT ELECTROCHEMICAL IMPEDANCE SPECTROSCOPY OF THIN  
FILMS UNDER LOCALLY CONTROLLED ATMOSPHERE

Meagan Papac, Kevin Talley, Ryan O'Hayre, and Andriy Zakutayev

### A.1 Synthesis by pulsed laser deposition

Thin films of BZY and BCFZY were deposited in a combinatorial pulsed laser deposition chamber (Figure A.1) that can ablate any of six loaded targets with a 248 nm KrF laser. The laser energy was set to 300 mJ with a pulse rate of 20 Hz. The heater setpoint for BZY was 800°C, with a base pressure below  $1 \times 10^{-6}$  Torr. The total pressure was brought up to 0.05 Torr by flowing oxygen. For the cathode films, the heater was set to 700°C, with a base pressure below  $1 \times 10^{-6}$  torr and the total pressure brought to 1 mT by flowing oxygen.

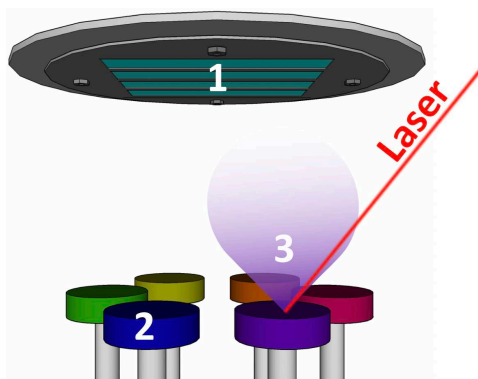


Figure A.1 Schematic of the interior of the combinatorial pulsed deposition chamber including the 1) substrate suspended above six 2) targets of different chemical compositions that are ablated by the laser, forming 3) a plume of material that is deposited onto the substrate.

### A.2 Statistical analysis

A Kolmogorov-Smirnov (KS) two-sample test was employed for statistical analysis. Table A.1 shows the results of KS tests comparing a spectrum from each contact to 1) a spectrum from the same contact measured at the same position on the heater ( $0^\circ$  same contact), 2) a spectrum from the same contact measured at a position rotated  $180^\circ$  around the center of the heater block ( $180^\circ$  same contact), or 3) a spectrum from a different contact measured at the same position on the heater ( $0^\circ$  different contact). The

Table A.1 KS test results from samples in different orientations and under different environmental conditions.

Orientation	Parameter (average value)	No flow	Dry air
0° same contact	p	0.744	0.861
	D	0.061	0.043
	% above critical	25	0
180° same contact	p	0.215	0.536
	D	0.139	0.077
	% above critical	56	2.5
0° different contact	p	-	0.229
	D	-	0.123
	% above critical	-	38.75

parameters from this fit are p, the probability that the two spectra came from the same distribution, and D, the normalized maximum difference between the two spectra. The critical value is determined by the size of the data set and the significance level,  $\alpha$ . Here, we apply  $\alpha=0.05$ . Perfect repeatability would be indicated by a p value of 1 and D equal to 0. The two spectra can be considered to be from the same distribution if the D value is below the critical value. For repeated measurements on all contacts in the same position (“0° same contact”) under dry air, the average p value was 0.861 and the average D value was 0.043 with a critical value of 0.144. When the sample was rotated (“180° same contact”), the average p value for the spectrum of each contact compared to the spectrum taken on the same contact in the rotated position was 0.536 and the D value was 0.077. The D value was still well below the critical value in most cases and much lower than D for the spectrum of each contact compared to the spectrum originating from a different contact on the same physical location on the heater block (“0° different contact”). Additional results showed that the measurements with dry air flow were more repeatable than the measurements with no gas flow (Figure A.2).

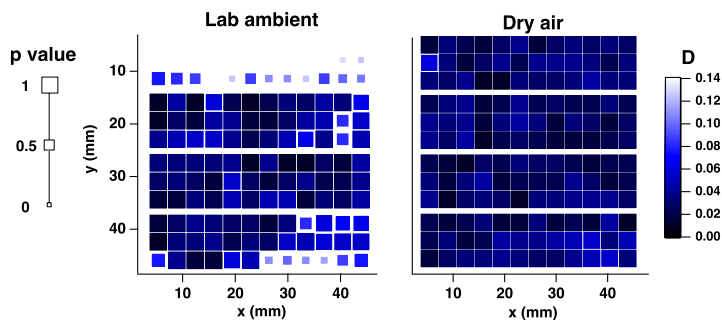


Figure A.2 KS test results show that  $R_{\text{elyte}}$  data values from fits of BZY20 impedance spectra taken under dry air are more repeatable than those taken under laboratory ambient conditions.

### A.3 Temperature calibration

The temperature calibration was performed by measuring the surface of an ITO-coated substrate at temperatures between 100°C and 500°C in 50°C increments (Figure A.3). A thermocouple was placed on a cured dot of silver paint, which was added to the surface of the substrate to increase thermal contact between the thermocouple and the surface. The probe was placed on the same silver dot as close to the thermocouple as possible, provided the spatial restriction imposed by the glass bell. Calibration showed

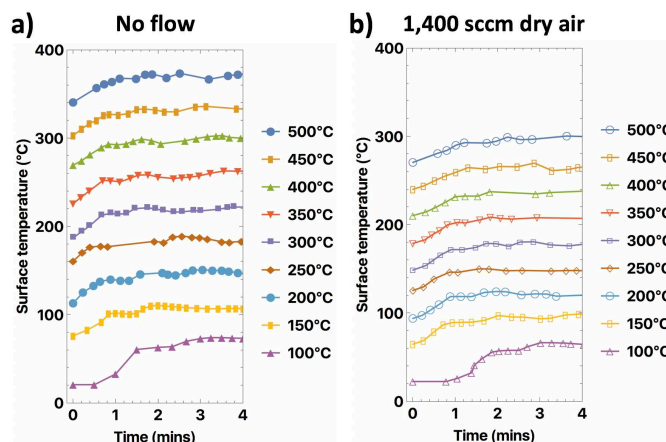


Figure A.3 Surface temperature over time at heater setpoints between 100°C and 500°C under a) no gas flow and b) 1,400 sccm of dry air. Time at 0 minutes represents the time that the heater setpoint was increased by 50°C.

that the temperature at the surface is always lower than the heater setpoint and that flowing gas reduces the surface temperature even further. Temperature calibration measurements also revealed the time required to reach consistent surface temperature. For each recorded temperature at each setpoint, the measured temperature can be compared to the mean temperature inclusive of the current and all successive measured temperatures. After a 50°C increase in the heater setpoint, the surface temperature stabilized to within 4°C of the mean within 4 minutes for temperature between 300°C and 500°C under both atmospheric air and 1,400 sccm dry air flow (Figure A.4), suggesting that this equilibration time is not sensitive to gas flow at this flow rate.

### A.4 Humidity calibration

Relative humidity was measured by connecting the open end of the glass probe enclosure to a handheld hygrometer. The hot plate was set to 40°C and the flow rate was varied between 1,400 sccm and 2,400 sccm. The relative humidity was recorded frequently for the first 30 mins and then was measured once more after 24 hours of flow at these conditions. While the humidity appeared to have stabilized after 30

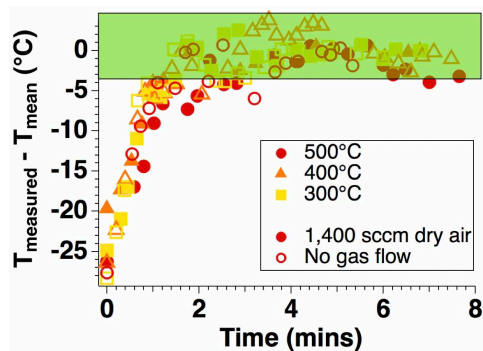


Figure A.4 Difference over time between the measured temperature at the sample surface and the mean measured temperature inclusive of the immediate and all successive measurements. For all temperature setpoints and gas environments, the temperature is within 3.5°C of the mean within 4 minutes after the temperature was raised by 50°C.

minutes, continued measurement indicated an additional change in humidity after 24 hours (Figure A.5). However, this change was within 2.2% of the value measured after less than 20 minutes.

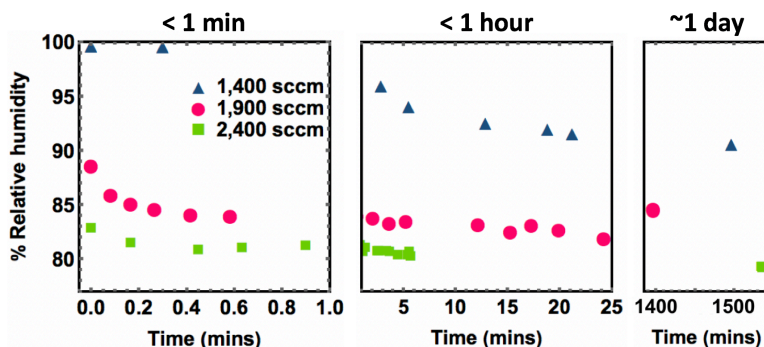


Figure A.5 Relative humidity over time for three different flow rates of humidified N<sub>2</sub> at a hot plate temperature of 40°C. After 20 minutes, humidity appeared to have stabilized. However, after 24 hours (1440 mins), it had reached a different, steady value.

### A.5 Alignment effects

The effect of a contact being measured off-center or with slightly less or more probe-to-contact pressure, were investigated by repeated measurements with slight variation in the x and z directions. The results are shown in Figure A.6. The effects of this variation were negligible.

### A.6 ITO resistance

An ITO substrate was annealed in the deposition chamber at 800°C at a total pressure of 1 mT achieved by oxygen gas flow after evacuation of the chamber. An array of 144 contacts was patterned using the same procedure that was used for the oxide films. The current-voltage behavior was mapped across the

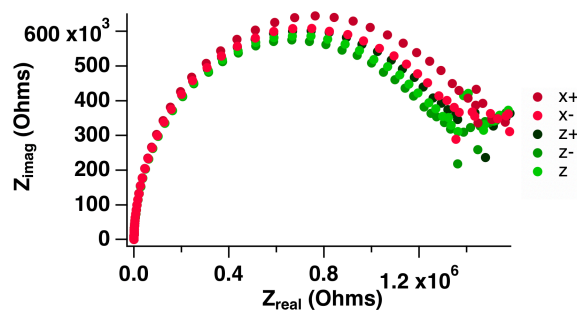


Figure A.6 Nyquist plot from a single contact measured with variation in x and z coordinates in the positive (+) and negative (-) directions with respect to the aligned position.

substrate under 1,400 sccm flow of both dry air and humidified  $N_2$ . The results from all sample points are represented in Figure A.7(a). These resistance values are similar to the ohmic resistance values obtained from equivalent circuit model fits of the BZY20 impedance spectra and are much less than ionic resistance values retrieved from the same fit (Figure A.7(b)). This indicates that the ITO resistance contributes to the ohmic resistance from the impedance spectra and does not interfere with the measurement of the electrolyte resistance.

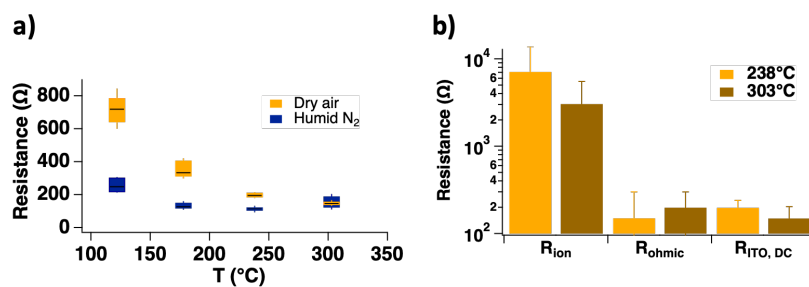


Figure A.7 DC resistance of ITO compared to resistances of samples measured by impedance spectroscopy. a) DC resistance of an ITO substrate patterned with a 144-point array of Ti/Au electrodes and measured under dry air and humidified  $N_2$ . Values at 303°C overlap for both conditions. b) DC resistance of ITO substrate compared to ohmic resistance ( $R_{ohmic}$ ) and BZY20 ionic resistance ( $R_{ion}$ ) from equivalent circuit model fit of impedance spectra measured at 238°C and 300°C under dry air.

APPENDIX B  
SUPPLEMENTAL INFORMATION FOR COMBINATORIAL SCREENING OF TRIPLE  
IONIC-ELECTRONIC CONDUCTING, TRANSITION-METAL SUBSTITUTED BARIUM ZIRCONATE  
ELECTRODES

Meagan C. Papac, Ryan O'Hayre, and Andriy Zakutayev

### B.1 Target synthesis

Targets of the following compositions were synthesized for PLD:  $\text{BaZr}_{0.6}\text{Y}_{0.3}\text{Fe}_{0.1}\text{O}_{3-\delta}$ ,  $\text{BaZr}_{0.1}\text{Fe}_{0.9}\text{O}_{3-\delta}$ ,  $\text{BaZr}_{0.1}\text{Co}_{0.9}\text{O}_{3-\delta}$ ,  $\text{BaZr}_{0.9}\text{Co}_{0.1}\text{O}_{3-\delta}$ ,  $\text{BaZr}_{0.8}\text{Y}_{0.2}\text{O}_{3-\delta}$ , and  $\text{BaZr}_{0.1}\text{Y}_{0.1}\text{Co}_{0.3}\text{Fe}_{0.5}\text{O}_{3-\delta}$ . First, ceramic powders were synthesized using a sol-gel method, described in more detail elsewhere.[187] The powder was ground with 10% PVA binder and pressed into 32 mm diameter pellets. These pellets were sintered at 1050-1150°C for 10-15 hours, depending on composition.

### B.2 X-ray diffraction spectra of thin films

Thin-film structure was investigated by x-ray diffraction spectra from each point of a 4x11 grid across the library. Peak positions from all measured points indicate a cubic perovskite structure.

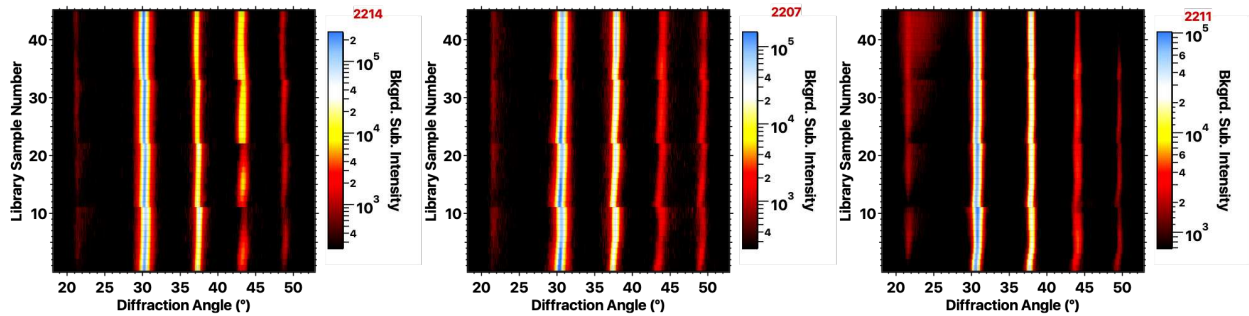


Figure B.1 XRD patterns of all libraries presented in this study. Each displays the peaks associated with a cubic perovskite structure and no additional peaks.

### B.3 Substrate comparison

The most intense peak of the ITO overlaps substantially with the most intense peak of BCFZY making it difficult to achieve structural analysis of the films on ITO(Figure B.2). Instead, diffraction patterns of BCFZY on  $\text{SiO}_2$  substrates were analyzed. However, the peaks are visible on both substrates and give no indication of structural changes in response to the change in substrate.

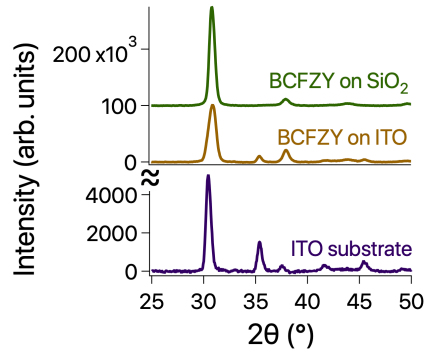


Figure B.2 Diffraction patterns of BCFZY films on  $\text{SiO}_2$  and on ITO compared to the diffraction pattern of an ITO substrate.

#### B.4 Equivalent circuit model results

Equivalent circuit models (ECM) can illuminate the impedance of different processes that possess distinguishable time constants. The circuit used here is shown in Figure B.3 and comprises a resistor in series with four parallel sets of resistors (R) and constant phase elements (CPE) and is similar to circuits commonly used to analyze MIEC impedance spectra.[23,24] The first resistor ( $R_0$ ) represents the ohmic resistance of the system. The first R-CPE combination element ( $R_1$  and  $\text{CPE}_1$ ) represents the electrolyte layer and its interface with the ITO substrate. The remaining R-CPE combination elements represent the charge transfer resistance ( $R_2$ ) and the diffusion resistances ( $R_3$  and  $R_4$ ) associated with the BCFZY electrode and/or the BCFZY/electrolyte.

#### B.5 Electrolyte impedance

Although the ECM method does not fit the low-frequency portion of the impedance spectra well, particularly under the humid gas condition, it does fit the high-frequency portion more accurately, making it possible to extract the electrolyte resistance from these fits (Figure B.4). Electrolyte resistance is higher under dry air than under humid  $\text{N}_2$ , as expected from this proton conductor, and has similar values across all three libraries for a given gas condition.

#### B.6 Validity of polarization resistance fit method

Although polarization resistance is typically calculated as the sum of resistances from equivalent circuit models (ECM). The method of extrapolating the modulus as frequency goes to 0 Hz yields more consistent results across all sample points, while ECM fitting yields more outliers. The ECM method is unable to consistently fit all spectra across a given library with the same model. Additionally, the shape of the low frequency impedance element is not always fully captured within the measured frequency range, leading to

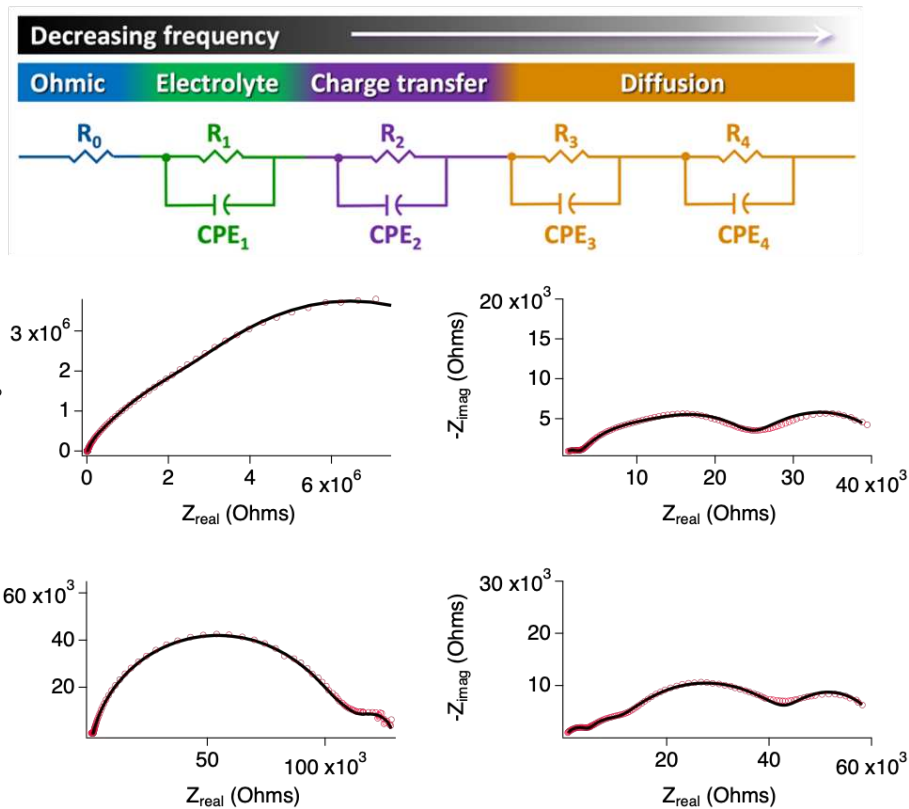


Figure B.3 Equivalent circuit model fits of impedance spectra. Nyquist plots show that the circuit elements are readily distinguishable in some spectra and not in others.

unreasonably high low-frequency resistance values for some spectra. To verify the validity of this approximation, we compared the results obtained by this method to polarization resistance obtained as the sum of resistances from the equivalent circuit model fit (when the model fit well) and to results obtained from the distribution of relaxation times. It is shown that this method yield values that are very similar to these other methods, although the different methods yield more similar results under dry (Figure B.5(a)) versus humid (Figure B.5(b)) gas atmosphere.

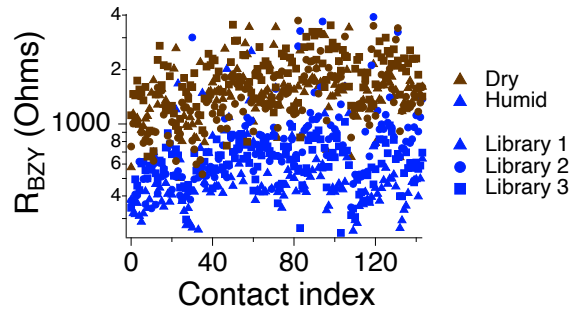


Figure B.4 Electrolyte resistance, as determined by the equivalent circuit model fit. The resistance is higher under dry air compared to humid  $N_2$ , due to increased bulk proton conductivity of BZY20 under humid conditions.

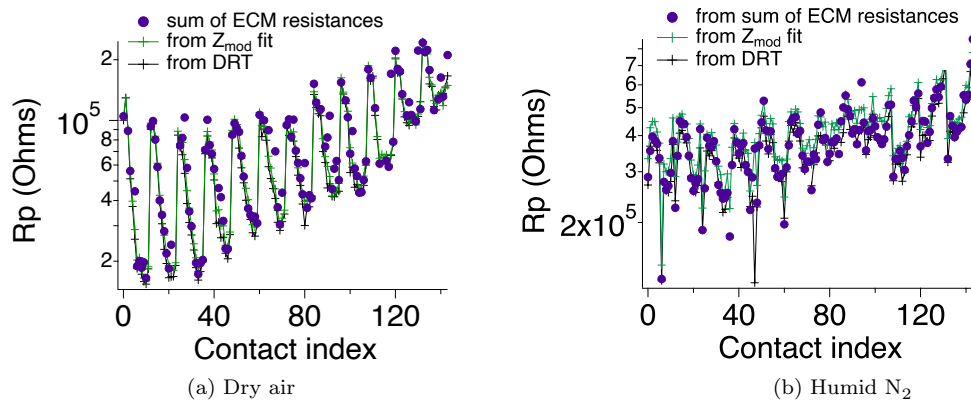


Figure B.5 Comparison of polarization resistance values obtained through different methods.  $R_p$  fit by extrapolating the modulus to 0 Hz yields similar values and identical trends when compared to  $R_p$  values from other methods, and has fewer outliers.

APPENDIX C  
COPYRIGHT PERMISSIONS

Permissions for the reuse of content in this dissertation that has been submitted and/or previously published are included in the accompanying supplemental file.